Characterization of the Nanostructure and Water Permeability of Self-Assembled Systems using Scattering Techniques

Master's thesis in Materials Science and Nanotechnology

Mikkel Killingmoe Christensen

Thesis submitted for the degree of Masters in
Materials Science and Nanotechnology
60 credits

Department of Chemistry
Faculty of Mathematics and Natural Sciences

UNIVERSITY OF OSLO

Spring 2019

Characterization of the Nanostructure and Water Permeability of Self-Assembled Systems using Scattering Techniques

Master's thesis in Materials Science and Nanotechnology

Mikkel Killingmoe Christensen

Characterization of the Nanostructure and Water Permeability of Self-Assembled Systems using Scattering Techniques

http://www.duo.uio.no/

Printed: Reprosentralen, Universitetet i Oslo

Abstract

Amphiphilic molecules such as surfactants and copolymers can self-assemble into a wide range of nanoscaled structures with shapes varying from spheres and cylinders, to bilayers similar to those found in cell membranes. These structures have many important applications ranging from detergents in soaps and cosmetics, to more advanced applications in site-specific drug delivery systems. Hence, research on these molecules and structures is of great interest, especially to understand how they depend on different molecular properties and how they are affected by variations in external conditions such as temperature, pH and salt. New research in this field can be used to gain deeper knowledge of the fundamental thermodynamics of self-assembled systems and for tailoring these to specific applications.

One of the most important and well-studied amphiphilic molecules is the anionic surfactant sodium dodecyl sulfate (SDS). It is known to form globular micelles in aqueous solutions which are highly sensitive to small changes in external parameters such as temperature, pH and ionic strength. Interestingly, the micelles elongate and form cylindrical micelles in the presence of salt that can reach almost macroscopic lengths. Even though this process is well-studied, the mechanisms of this transition has not yet been fully described quantitatively. Experimental results can in combination with computer simulations be used to develop more accurate models to describe the details of the transition. By using synchrotron small-angle X-ray scattering (SAXS) combined with analytical models, the globule-to-cylinder transition is in this work characterized as a function of ionic strength with different salts (NaCl, $MgCl_2$, KCl and $CaCl_2$). Both NaCl and $MgCl_2$ were found to cause an exponential increase in the contour length of the micelles as a function of ionic strength, whereas KCl and $CaCl_2$ were found to cause phase separation. The resultant phase diagrams show overlap between the globule-to-cylinder transition regions in terms of ionic strength for NaCl and $MgCl_2$. At the highest concentrations of $MgCl_2$, it was in addition found evidence of long cylinders with finite flexibility and possible cross-linking and/or branching.

The other main subject of this work is the diblock copolypeptides PBLG-PLL composed of a hydrophobic block of poly-γ-benzyl-L-glutamate (PBLG) and a hydrophilic block of poly-L-lysine (PLL). These specific copolypeptides are thought to form large vesicles in aqueous solution and are hitherto uncharacterized in literature. The vesicles were studied by attempting to fit an analytical model for a vesicle structure to SAXS data based on results from dynamic light scattering (DLS) and transmission electron microscopy experiments (TEM). Although evidence of vesicles was observed using TEM, scattering experiments indicated the presence of additional morphologies. The structural characterization of the system using a vesicle model was therefore not successful. Nonetheless, the particles were by qualitative analysis of the scattering data found to be exceptionally stable towards changes in parameters such as temperature and ionic strength, which are desirable properties in many applications. The water transport through the vesicle membranes was also studied using time-resolved small-angle neutron scattering (TR-SANS) to investigate the permeability of the membrane. Remarkably, the complete exchange of water was found to occur faster than the time scale available in the experimental set-up, which is not typical behavior for copolymer membranes.

Sammendrag

Surfaktanter og kopolymerer er molekyler som kan selvassosiere på nanonivå til en rekke forskjellige strukturer. Dette kan være alt fra sfærer og sylindre, til bi-lag tilsvarende de som finnes i cellemembraner. Disse strukturene har mange viktige anvendelser som for eksempel surfaktanter i såpe og kosmetikk, til mer avanserte anvendelser som medisinbærere i nanomedisinsystemer. På bakgrunn av dette kan forskning på disse molekylene og strukturene være meget nyttig, og det er spesielt viktig å forstå hvordan de avhenger av forskjellige molekylære egenskaper og hvordan de påvirkes av endringer i eksterne parametere som temperatur, pH og salt. Ny forskning på dette feltet kan dermed brukes til å bedre forståelsen av den fundamentale termodynamikken til selvassosierende systemer og for å skreddersy disse til spesifikke anvendelser.

Et av de mest viktige og velstuderte amfifile molekylene er den anioniske surfaktanten natriumdodecylsulfat (SDS). Denne surfaktanten danner globulære miceller i vandige løsninger som er høyst sensitive til små endringer i eksterne parametere som temperatur, pH og ionestyrke. En interresant egenskap ved disse er at de i tilstedeværelse av salt forlenges og danner sylindriske miceller som kan nå nesten makroskopiske lengder. Selv om denne prosessen er velstudert, har ikke mekanismene bak denne overgangen blitt fullstendig beskrevet kvantitativt. Eksperimentelle resultater kan i kombinasjon med datasimuleringer bli brukt til å utvikle mer nøyaktige modeller for å beskrive detaljene rundt denne overgangen. Ved å bruke lav-vinkel røntgenspredning (SAXS) fra en synkrotronkilde i kombinasjon med analytiske modeller, ble globulær-til-sylinderovergangen i dette arbeidet karakterisert som en funksjon av ionestyrke med forskjellige salter (NaCl, $MgCl_2$, KCl and $CaCl_2$). Både NaCl og $MgCl_2$ forårsaket en eksponentiell økning i konturlengden til micellenene som en funksjon av ionestyrke, mens KCl og $CaCl_2$ forårsaket faseseparasjon. Fasediagrammer basert på disse resultatene viser overlapp mellom overgangsområdene ved bruk av ionestyrke for NaCl og $MgCl_2$. Ved den høyeste konsentrasjonen av $MgCl_2$ ble det i tillegg påvist lange, fleksible sylindre med mulig krysslinking og/eller forgrening av micellene.

Det andre hovedemnet i dette arbeidet er diblokk-kopolypeptidene PBLG-PLL bestående av en hydrofobisk del av poly-γ-benzyl-L-glutamat (PBLG) og en hydrofil del av poly-L-lysin (PLL). Disse kopolypeptidene er forventet å produsere store vesikler i vandig løsning og er frem til nå ubeskrevet i litteraturen. Vesiklene ble studert ved å forsøke å tilpasse en analytisk modell for en vesikkelstruktur til SAXS-data basert på resultater fra dynamisk lysspredning (DLS) og transmisjonselektronmikroskopi (TEM). Selv om tegn til vesikler ble funnet med TEM, indikerte spredningseksperimentene tilstedeværelse av andre morfologier. Den strukturelle karakteriseringen av systemene ved bruk av en vesikkelmodell ble derfor mislykket. På tross av dette, ble spredningskurvene fra partiklene analysert kvalitativt, og partiklene ble funnet til å være eksepsjonelt stabile ved endringer av parametere som temperatur og ionestyrke, noe som er ønsket i mange anvendelser. Vanntransporten gjennom vesiklene ble også studert ved bruk av tidsoppløst lav-vinkelnøytronspredning (TR-SANS) for å måle permeabiliteten til membranene. En komplett utveksling av vann gjennom bi-laget skjedde her raskere enn tidsskalen som var tilgjengelig med det eksperimentelle oppsettet, noe som er bemerkelsesverdig og en utypisk egenskap ved kopolymermembraner.

Acknowledgements

This work was carried out in the period from August 2017 to May 2018 for the Soft Matter research group at the Department of Chemistry for the master's degree in materials science and nanotechnology at the University of Oslo

First of all, I would like to thank my main supervisor Reidar Lund for convincing me to work with the exciting field of soft matter and scattering techniques and for accepting me into his group. This has allowed me to acquire unique knowledge by combining chemistry, physics and biology that will be valuable in my future life and career. I am also grateful for the opportunities I have had to visit large-scale research facilities in France and Germany, and for all the help with experiments, analyses and writing of the thesis.

Then, I wish to offer special thanks and gratitude to my co-supervisor Matthias Amann who is unfortunately no longer with us. With his excellent teaching skills and scientific insights, he was of great help in all aspects of my work. His help and patience was especially valuable when he in detail taught how to work in a lab, use different instruments and analyze data. These two years would not have been the same without him and he will, despite his passing, continue to inspire us by his admirable personality and dedication to science.

I would also like to acknowledge the other people in the Soft Matter research group, namely, Victoria Ariel Bjørnestad, Josefine Eilsø Nielsen, Synne Myhre, Nico König and Mirna Porobic. Thank you for all your help, support and for making these two years fun and exciting. Also thanks to Hermis Latrou and his group at the University of Athens for the synthesis of the copolypeptides I have studied, and to the beamline scientist Mark Tully, Petra Pernot, Gabriele Giachin and Sylvain Prevost at the European Synchrotron Radiation Facility in Grenoble, France, and to Vitaily Pipich at the Forschungs-Neutronenquelle Heinz Maier-Leibnitz in Münich, Germany.

Lastly, I want to thank my partner Oda Hagen, my friends, and my dear family for all the support, help and love you have given me throughout this period.

Mikkel Killingmoe Christensen,
May 2019

Abbreviations and symbols

°C	Degrees Celsius
$1/\kappa$	Debye screening length
2θ	Scattering angle
A	Scattering amplitude, monomers, micelles
a_0	Scattering amplitude (wave), equilibrium head group area of amphiphile
b	Scattering length, Kuhn length, fitting coefficients
BG	Background scattering
B	Structure factor constant (PRISM)
c	Concentration
CCD	Charge-coupled device
CMC	Critical micelle concentration
D	Diffusion coefficient, distance, size distribution function
D_{max}	Maximum distance
d	Density, thickness
dR	Head group thickness
DLS	Dynamic light scattering
$d\Sigma/d\Omega$	Differential scattering cross-section
e	Elementary charge
E	Energy
ESRF	European Synchrotron and Radiation Facility
f	Fraction
FWHM	Full width at half maximum
g_0	Normalized auto-correlation function
G	Distribution of decay rates, auto-correlation function
I	Ionic strength
IFT	Indirect Fourier transform
$I(q)$	Intensity
J_1	First order Bessel function of first kind.
k	Boltzmann's constant, equilibrium constant
k_i	Incident wave vector
k_f	Scattered wave vector
l_0	Length of hydrophobic block
l_d	Debye screening length
L	Length
L_c	Contour length

L_{mean}	Average contour length
$\overline{M_n}$	Number average molecular weight
$\overline{M_w}$	Weight average molecular weight
NNLS	Non-negative least squares
p	Packing parameter, pair-distance distribution function
PCS	Photon correlation spectroscopy
PCCS	Photon cross-correlation spectroscopy
PD	Polydispersity
PLL-PBLG	Poly-γ-benzyl-L-glutamate-*block*-poly-L-lysine
$P(q)$	Form factor
PRISM	Polymer reference interaction model
n	Refractive index
N	Aggregation number, number of particles
N_A	Avogadro's number
N_{ave}	Average aggregation number
q	Momentum transfer
r	Position, distance
R_{core}	Core radius
r_e	Thompson radius
R_h	Hydrodynamic radius
R_{HS}	Hard-sphere radius
R_G	Radius of gyration
R_{tot}	Total radius
RPA	Random-phase approximation
SANS	Small-angle neutron scattering
SAS	Small-angle scattering
SAXS	Small-angle X-ray scattering
SDS	Sodium dodecyl sulfate
SLD	Scattering length density
S_{SQ}	Scale factor in Hayter-Penfold structure factor
$S(q)$	Structure factor
t	Time
T	Temperature, transmission
TEM	Transmission electron microscope
TR-SANS	Time-resolved small-angle scattering
v_0	Hydrophobic block volume
v	Resolution volume
V	Volume, interaction potential

V_{core}	Core volume
V_{shell}	Shell volume
V_{tot}	Total volume
vol. %	Volume percent
wt. %	Weight percent
W	Width of shell/core
z	Charge
Z	Number of charges per particle
α	Smoothing parameter
β	Stretching parameter in DLS, parameter in PRISM structure factor
γ	Interfacial free energy
Γ	Gamma function
Γ_c	Decay rate
$\Delta\rho$	Excess scattering length density (contrast)
ϵ	Aspect ratio, free energy
ϵ_p	Solvent permittivity
η	Viscosity, hard-sphere volume fraction
θ	Scattering angle
Λ	Constant in expression for the free energy per molecule in a globular micelle
λ	Wavelength
ρ	Scattering length density, radial density
σ	Scattering cross-section, half-width of graded interface
σ_{PD}	Polydispersity
τ	Relaxation time
φ	Phase difference
ϕ	Volume fraction
Ω	Solid angle

Contents

1 Introduction and aims

The field of soft matter is an exciting area of science with a wide variety of materials and applications. It includes colloids, polymers, surfactants and nanoparticles which can arrange into a plethora of structures at the nanolevel and above. Some of these polymers and surfactant molecules are so-called amphiphiles which can self-assemble into supramolecular structures in solution due to the hydrophobic effect and other interactions. These molecules and structures share the common feature that the predominant physical behaviors happen at an energy scale comparable with the thermal energy at room temperature, hence the word "soft". As a result, the properties of the structures depend on a fine balance between attractive, repulsive and entropic forces, and can usually be changed by small variations in solvent conditions such as temperature, ionic strength, pH and concentration [1]. This allows for the design of an endless variety of shapes and sizes, making them intriguing research subjects due to the promising applications ranging from detergents in soap and cosmetics to more advanced applications in nano- and biotechnology such as in site-specific drug delivery systems [2-5]. It is also relevant to the study of biological systems since important structures such as cell membranes, proteins and DNA belong to the category of soft matter. In all these applications, it is essential to understand how the structure and dynamics of the self-assembled structures are impacted by environmental parameters, and the research in the field is far from finished.

The main focus of this work is to study the world of surfactants and amphiphilic diblock polymers in aqueous solutions, which can be seen illustrated in Figure 1. Surfactants typically consist of one hydrophilic head group, which can be charged, and a hydrophobic tail which is usually a hydrocarbon chain (Figure 1 (a)). Above a certain critical concentration in aqueous solution, these molecules aggregate into what is known as micelles [6]. The hydrophobic tails avoid the solvent and form the core of the micelle, whereas the hydrophilic head groups expose themselves to the solvent forming a surrounding corona. Similar structures can also be formed by the self-assembly of amphiphilic diblock polymers consisting of two covalently linked hydrophobic and hydrophilic blocks (Figure 1 (b)). At a certain ratio between the two blocks, these molecules will instead aggregate into a bilayered structure which can curve up and form a vesicle with a water-filled core, similar to that of a cell membrane [7].

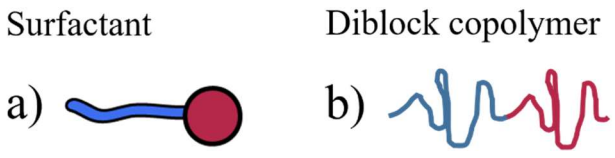

Figure 1: (a) Schematic drawing of a surfactant illustrating the hydrophilic tail (blue) and hydrophobic head group (red). **(b)** Schematic drawing of a diblock copolymer chain with the hydrophobic block (blue) and hydrophilic block (red). The drawings are not to scale.

The self-assembled aggregates come in a variety of shapes and sizes due to their soft and dynamic nature. This includes spherical, ellipsoidal, cylindrical and disk-like micelles, and also lamellar structures like flat bilayers, vesicles and hollow cylinders. The preferred morphology is, among other properties, determined by the geometry of the amphiphile, which varies greatly from a small surfactant molecule to a long polymer chain [8]. In addition to the characteristics of the molecule, the solvent conditions will, as

mentioned above, impact the micellar morphology. Thus, by changing a parameter like pH or the ionic strength of the solution, the structure can be altered deliberately which allows for the study of how variations in environmental factors impacts the structures. This is important for obtaining a deeper understanding of the thermodynamics of self-assembled systems and for the tailoring of such systems to certain applications.

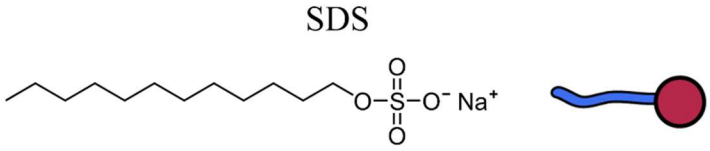

Figure 2: Structural formula and schematic drawing of the anionic surfactant sodium dodecyl sulfate (SDS).

In the field of soft matter science, the micelle-forming anionic surfactant sodium dodecyl sulfate (SDS) is one the most extensively studied. It is part of the growing multibillion-dollar surfactant market [1], and this system has been used as a model system for the study of ionic surfactants for decades. As seen illustrated in Figure 2, the SDS molecule consists of a negatively charged sulfate head group and a C_{12} hydrocarbon chain which in aqueous solutions aggregates into globular micelles of limited sizes. The shape and size of the formed micelle is controlled and limited by inter-molecular repulsion caused by the charges of the head groups. However, by adding salts to the solution, the charges can be partially screened which lead to a change in the surfactant geometry and the resultant micelle morphology [8]. At high electrolyte concentrations, the globular micelles elongate and form cylindrical micelles as illustrated in Figure 3. By tuning the concentration of the electrolytes, one can obtain a relatively precise control of the micelle morphology [9-12]. It is thereby possible to study the effect of different salts and of variations in the ionic strength of the solvent on structural parameters such as radius and length. Despite decades of research, the dynamics and mechanisms of these morphological transitions in surfactant micelles are still not fully understood. Making progress in the field is therefore important in areas such as cosmetics, detergency and emulsification, where a successful formulation is governed by effects such as foaming and solubilization [2, 5, 13].

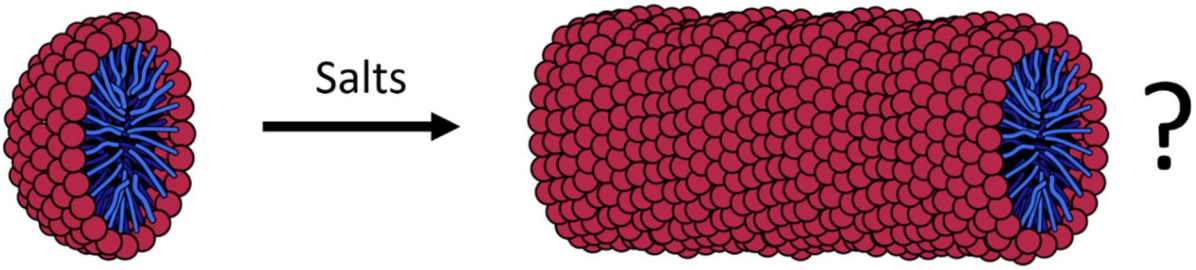

Figure 3: Globular micelles formed by the surfactant SDS is known to elongate and form cylindrical micelles in the presence of high concentrations of salt. The effect of different salts and ionic strengths on the structure is, however, not fully understood. The graphics are adapted from reference [14].

The micelles formed by SDS and similar surfactants in aqueous solutions have been studied extensively since the 1960s to determine the micelle sizes, shapes and inter-micellar interactions [9, 15, 16]. The major techniques included static light scattering in the 60s, dynamic light scattering starting in the early 70s and lastly small-angle scattering starting in the 80s. Although the pronounced effect of electrolytes on SDS micelles, such as the elongation, were known early, more modern methods were needed to obtain more precise information about the internal structures and lengths. In more recent work on SDS in aqueous solutions of NaCl and NaBr, extensive information has been obtained on the structural changes as a function of salt concentration [10-12]. This has been possible due to improvements in experimental techniques in combination with computer simulations and better analytical models used in the data analysis. It was shown in these studies that the morphology at low salt concentrations were that of prolate or oblate ellipsoids. Then, at a certain salt concentration, these were found to form cylindrical micelles which then became flexible and formed so-called worm-like micelles of almost macroscopic lengths at even higher concentrations. Studies on the behavior of SDS and other surfactants in aqueous solutions with other salts also exist [17-22]. There is, however, still ambiguity in the literature about the shape of the micelles at certain conditions, and the effect of ionic strength and other salts on the structure are not yet extensively studied using the latest techniques and analysis methods. Additionally, the exact mechanism and cause of the morphological transitions are thus far only described qualitatively, and cannot be fully resolved using scattering techniques alone. To create a model to explain these mechanisms, one needs precise information of how ions bind to micelles, and how this process influences the local structure and morphology. This is usually studied using molecular dynamics in computer simulations, and it is in this case essential to have experimental data from techniques such as small-angle scattering for comparison and confirmation of the data. In a paper from Sangwai et al. [23] utilizing molecular dynamics, it is reported that ions bond weakly to the SDS head groups to form an electrical bilayer around the water-micelle interface which causes a screening effect. This reduces the surface area per surfactant and leads to the transition from globular to cylindrical micelles. In another paper using molecular dynamics by Volkov et al. [24], it was reported that the loss in entropy caused by the transition was compensated by the gain in interaction energy between surfactant molecules. The results from this thesis will, however, later be used in the development of a new model proposed by K. Shäfer et al. based on results from molecular dynamics which includes details on the co- and delocalization of sodium ions on the head groups of SDS and suggest that the sodium ions bridge the surfactant molecules in pairs [25].

Amphiphilic block copolymers behave in similar ways as surfactants in aqueous solutions. However, due to the endless range of polymers that can be synthesized with variations in parameters such as block length, hydrophobicity and charge, they provide even greater opportunities for structures that are tailor-made for specific applications and also for research on the fundamental physics of their self-assembly [7, 26]. Vesicles are one of the more intriguing structures formed by block copolymers due to the water trapped in the core which, among other things, allows for the encapsulation of hydrophilic drugs. An example of such a vesicle can be seen in Figure 4. Encapsulation makes it possible to deliver and release drug molecules which otherwise have low solubility in blood or limited circulating half-lives [4, 27]. These vesicles have thus received great interest in the field of controlled drug delivery over the last few decades.

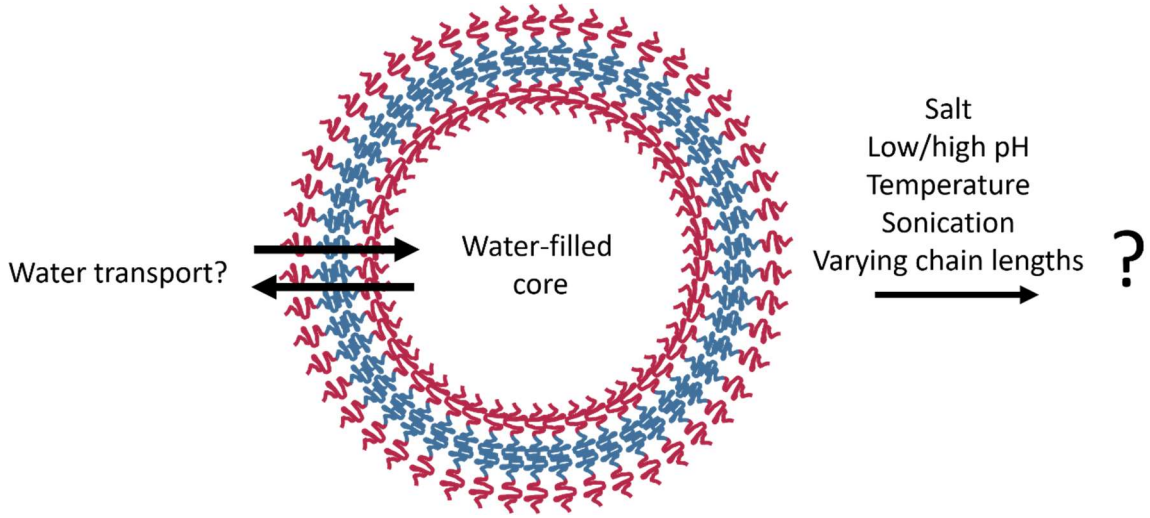

Figure 4: Schematic drawing of a diblock copolypeptide vesicle. The structure of such vesicles made of the copolypeptide PBLG-PLL with different lengths of the hydrophilic PLL block will in this work be characterized with variations in solvent parameters such as pH, temperature and salt concentration. The water transport through the bilayer membrane will also be investigated. These properties are important in applications such as site-specific drug delivery.

A promising class of block copolymers are those composed of amphiphilic polypeptide blocks, i.e. polymers based on amino acids. Since polypeptides can be hydrolyzed into natural amino acids, they are usually biocompatible and can be used more readily in biomedical applications compared to most synthetic polymers [28]. In this work, vesicles formed by a series of well-defined diblock copolypeptides referred to as PBLG-PLL are investigated, and can be seen illustrated in Figure 5. They are composed of a hydrophobic block of poly-γ-benzyl-L-glutamate (PBLG) and a hydrophilic block of poly-L-lysine (PLL) which is highly charged at neutral pH. The copolypeptide is synthesized in several versions where the length of the hydrophilic PLL chain is varied, while the length of hydrophobic PBLG block is kept at an almost constant value. This allows for the study of how the hydrophilic block length affects the structure. As opposed to SDS, the PBLG-PLL copolypeptides used in this work are novel compounds synthesized by a collaborating lab [29, 30]. There is therefore limited literature available on vesicles formed by these exact molecules. There is, however, done considerable research on similar charged copolypeptides and their corresponding self-assembled structures [7, 26, 28, 31, 32], in addition to studies on the individual polypeptides of L-lysine and γ-benzyl-L-glutamate. In one of the studies, the charged diblock copolypeptide poly(L-lysine)-*block*-poly(L-leucine) with a similar PLL block length as the copolypeptides studied in this work was found to form stable vesicles in aqueous solution [31]. In analogy to SDS micelles, PLL based vesicles are also expected to be affected by changes in external parameters such as pH and salt concentration. Interestingly, a PLL chain exists as a random-coil at neutral pH, but changes to a helical conformation at high pH due to the reduction in charge [33, 34]. This was exploited in another study by J. R. Hernandez and S. Lecommandoux where the diblock copolypeptide poly(L-glutamic acid)-*block*-poly(L-lysine) was found to form vesicles with a pH sensitive morphology [32]. An increase in pH is therefore likely to also alter the structure of the PBLG-PLL vesicles used herein, and can possibly be used as a trigger for drug release through changes in membrane permeability or in the morphology. The use of pH as a trigger is in this case especially interesting due to the variations in pH that can be found in normal and diseased biological tissues [35].

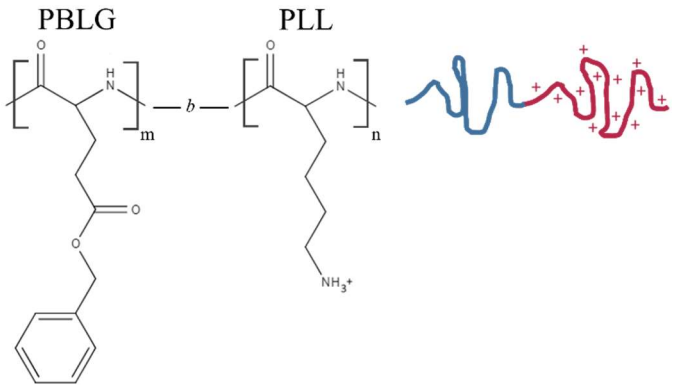

Figure 5: Condensed structural formula and schematic drawing for the diblock copolypeptide PBLG-PLL (poly-γ-benzyl-L-glutamate-*block*-poly-L-lysine).

The micellar and vesicular structures in this work are mainly studied using scattering techniques. One of the most suitable scattering techniques for the investigation of micelles and vesicles is small-angle scattering (SAS) using X-rays or neutrons. It is optimal for these systems as it can probe the average structure of a large number of aggregates in situ and resolve details from approximately 1-100 nm. Moreover, it can be used to study inter-particle interactions and dynamical processes such as water transport through bilayer membranes. In this work, structural characterizations were mainly done using small-angle X-ray scattering (SAXS), while the dynamic processes were studied using time-resolved small-angle neutron scattering (TR-SANS). Most scattering experiments were carried out at large-scale synchrotron or neutron facilities to achieve good quality data from a large number of samples in a short time period. In addition to these, dynamic light scattering (DLS) and transmission electron microscopy (TEM) were applied as complementary techniques for the PBLG-PLL system. While these techniques can be used to obtain structural parameters, they cannot be used directly to acquire detailed mechanisms of the morphological transitions induced by salt. The scattering and imaging data can, however, be used in conjunction with computer simulation methods such as molecular dynamics to develop new models to explain such mechanisms.

Finally, after introducing the systems studied in this work, the three main aims can be summarized as follows:

- Investigate the effect of different salts (NaCl, $MgCl_2$, KCl and $CaCl_2$) and ionic strengths on the structure and morphology of sodium dodecyl sulfate micelles in aqueous solutions using small-angle X-ray scattering.
- Resolve the structure of self-assembled particles composed of the diblock copolypeptide PBLG-PLL using small-angle X-ray scattering and investigate the effects of PLL block length, concentration, pH, temperature, salt and sonication on the structure to assess its potential as a drug-delivery system.
- Study the water transport through bilayer vesicles formed by PBLG-PLL using time-resolved small-angle neutron scattering.

2 Theory

2.1 Self-assembly

2.1.1 General principles of amphiphilic self-assembly

Surfactants and certain diblock copolymers are some of the molecules which exhibit amphiphilic properties when dissolved in water. One part of the of the molecule is typically hydrophobic, and another part hydrophilic due to its charge and/or polar character. Above a certain temperature and concentration, the unfavorable contact between the water and hydrophobic parts will lead to the formation of structures known as micelles in which the hydrophobic parts of the molecule is shielded from the hydrophilic environment [6]. This happens spontaneously without any external manipulation, and is mainly caused by what is known as the hydrophobic effect where the loss of entropy of water molecules leads to a large effective surface tension [6]. The micelles can adopt different shapes including spheres, discs, ellipsoids and rods depending on the characteristics of the amphiphiles and the solvent conditions. They can also form bilayered structures like sheets, globular vesicles with an internal cavity resembling the structure of a cell membrane and also hollow cylinders. Examples of such morphologies can be seen in Figure 6.

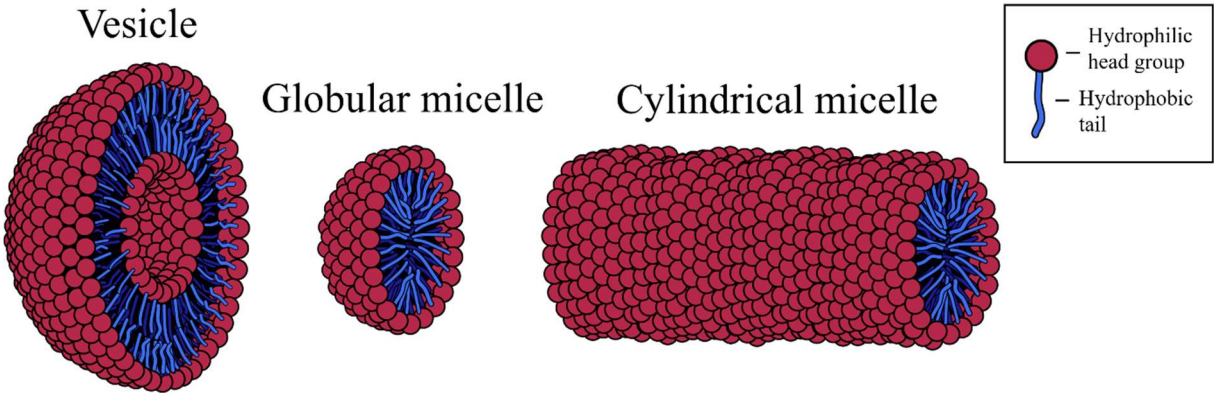

Figure 6: Examples of self-assembled structures formed by surfactant molecules. For diblock copolymers, the red head groups in the illustrations are exchanged for longer chains. The graphics are adapted from reference [14].

A parameter often used to describe a micellar system is the aggregation number N which is defined as the number of molecules present in a micelle. Since there usually is a distribution of micelle sizes in a solution, a more correct description is given by the average number of given by the average aggregation number N_{ave} with an accompanying deviation from this number in accordance with the type of distribution. The amphiphilic molecules only aggregate with a defined aggregation number above the so-called critical micelle concentration, generally abbreviated as «CMC». The CMC for a given system varies with parameters such as temperature, pressure and the presence of electrolytes and other surface active molecules. When adding monomeric amphiphilic molecules to a solution, the monomers will initially partition in the water-air interface to lower the interface energy and shield the hydrophobic parts from the water. When the

surface coverage is sufficient, the amphiphiles aggregate into micelles to further decrease the free energy of the system [36]. Above the critical concentration, the number of monomeric amphiphiles in solution remains constant, and any further addition of amphiphiles will go into aggregates. To determine the CMC for a given system experimentally, one can monitor parameters like surface tension, turbidity or viscosity while increasing the concentration of the micelle-forming amphiphiles. The point where there is a sharp change in slope for the measured parameter is then defined as the CMC.

The CMC and the formation of micelles can be rationalized from the equilibrium

$$nA_1 \overset{k}{\rightarrow} A_n \tag{1}$$

where A_1 denotes the free monomers, A_n denotes the micelles and k is the equilibrium constant [37]. It is here assumed that all micelles contains exactly n amphiphilic molecules. The equilibrium constant is then given by

$$k = \frac{[A_n]}{[A_1]^n} \tag{2}$$

where $[A_n]$ and $[A_1]$ are the concentrations of micelles and monomers, respectively. One can now introduce the parameter v which describes the number of molecules per object (i.e. monomers plus micelles) which is given by the expression:

$$v = \frac{[A_1] + n[A_n]}{[A_1] + [A_n]} \tag{3}$$

By combining Equation 2 and 3, v can be written as:

$$v([A_1]) = \frac{1 + nk[A_1]^{n-1}}{1 + k[A_1]^{n-1}} \quad \text{or} \quad v(x) = \frac{1 + nkx^{n-1}}{1 + kx^{n-1}} \tag{4}$$

The plot of v as a function of x (Figure 7) show a sharp increase in the number of molecules per object micelles with a midpoint at a concentration x that satisfies $1/k = x^{n-1}$. This concentration will then be the CMC and indicates the transition from free monomers to micelles. Below the CMC, $v \approx 1$ since $x^{n-1} \ll 1/k$ for low values of x, and the solution is thus dominated by free monomers. For high values of x, however, $v \rightarrow n$ and micelles dominate the solution.

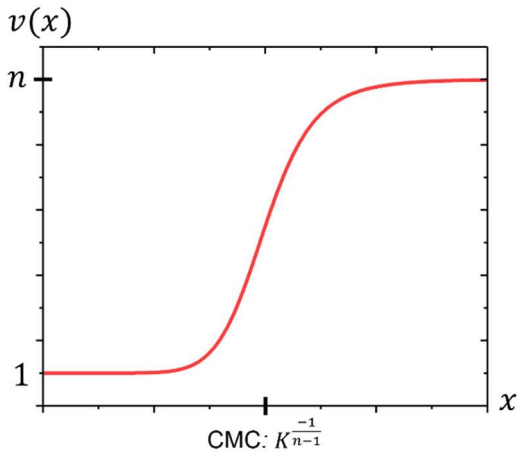

Figure 7: Graph illustrating the model describing CMC and micelle formation. Below the CMC, most amphiphiles exists as free monomers in solution, while above the CMC, most molecule are in micelles containing n monomers.

Another way of describing micelle formation is through thermodynamics. This can be quite challenging as it should take into account the hydrophobic, electrostatic and entropic contributions giving rise to surface energies, chain stretching and hydrophilic head interactions, as well as the translational entropy of micelles, monomers and counter ions. Nevertheless, the main forces governing the formation of can be simplified into three contributions that have been illustrated Figure 8. The equilibrium structure results from the balance between the hydrophobic interactions and the repulsion between the head groups leading to the interfacial free energy per amphiphile given as [38]

$$\mu_N^0 = \gamma a + \frac{K}{a} \tag{5}$$

where K is a constant, γ is the interfacial free energy, a is the head group area. The first term represents the attractive contributions, while the second accounts for the repulsion. With the assumption that the interactions operate in the same interfacial area, the minimum of μ_N^0 is found at $a_0 = \sqrt{K/a}$ [38]. K can now be replaced in Equation 5 to get:

$$\mu_N^0 = 2\gamma a_0 + \frac{\gamma}{a}(a - a_0)^2 \tag{6}$$

Consequently, a change in the head group area a_0 is energetically unfavorable and thus introduces geometrical constraints on the structure.

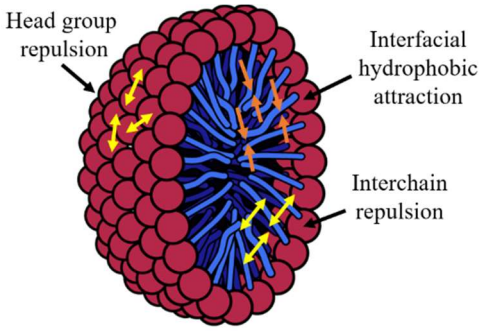

Figure 8: Illustration of the main forces governing the formation of a surfactant micelle. The graphics aretab adapted from reference [14].

The effective shape of the micelles is classically rationalized in terms of the mentioned geometrical packing constraints, which is convenient as it circumvents any considerations about intermolecular interactions. A change in shape can be thought of as a change in the experimentally or numerically determined packing parameter p defined as [38]:

$$p = \frac{v_0}{a_0 l} \tag{7}$$

Here, v_0 and l are the hydrophobic tail (block) volume and length, respectively, and a_0 is the equilibrium head group area. In general, it is found that $p \leq 1/3$ will lead to globular structures and $1/3 < p < 1/2$ will lead to cylindrical structures. This can also be applied to bilayer structures, which will have a value of $1/2 < p \leq 1$. These bilayers can also curve up and form vesicles as long as the area a_0 can be maintained. A cone-shaped surfactant molecule and a cylindrical shaped diblock copolymer molecule with their corresponding packing parameters are illustrated in Figure 9.

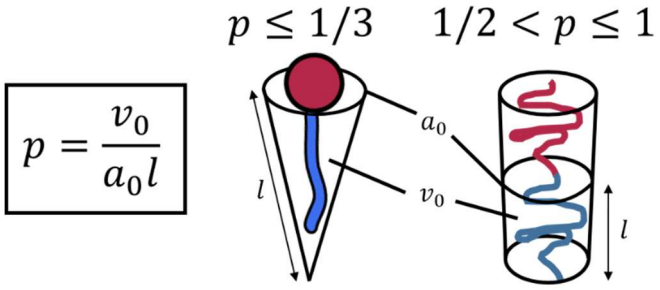

Figure 9: Illustration of the packing parameter p for a cone-shaped surfactant molecule leading to globular micelles and a cylindrical shaped copolymer molecule leading to bilayered structures. The figures are not to scale.

2.1.2 Globular surfactant micelles

As seen in Figure 9, an anionic surfactant molecule like sodium dodecyl sulfate takes up the effective shape of cone in aqueous solutions due to the electrostatic repulsion between the head groups [36]. This yields a

simple globular micelle with a compact core of hydrocarbon tail groups and a shell formed by the hydrophilic head groups combined with a significant amount of water.

If the formation of globular micelles is favored, one would expect the interfacial energy per surfactant molecule to have a minimum value for a certain aggregation number $N = N_{ave}$ resulting in an optimal size for the micelle. Micelles smaller than this value will have too large head group areas causing unfavorable contact between the hydrophobic tails and the water. If they on the other hand become too large in size, the head groups will come too close. This can be described through the expression for the free energy per molecule in a micelle given as [8, 39]

$$\mu_N^0 = \mu_{N_{ave}}^0 + \Lambda(N - N_{ave})^2 \tag{8}$$

where $\mu_{N_{ave}}^0$ is the lowest free energy and Λ is a constant given by $\Lambda = \gamma a_0 / 9N_{ave}^2$. Even though an optimal size exists, the micelles will have a spread in the aggregation number around the aggregation number with the lowest free energy due to thermal fluctuations and thus be polydisperse in size. This polydispersity will nevertheless be small as the free energy curve is usually relatively narrow around $\mu_{N_{ave}}^0$. The size of the globular micelles is therefore virtually independent of concentration in most cases.

2.1.3 Surfactant micelles in electrolyte solutions

When adding an electrolyte like NaCl to a solution of micelles formed by ionic surfactants like SDS, the ions from the salt will mix into the layer of associated counter-ions and shield the electrostatic interactions of the charged surfactant head groups. The ions organize as an electrical double layer which can be modeled as a diffuse layer of charges with a characteristic length scale known as the Debye screening length, l_D, defined as the distance where the Coulomb interactions have decreased in magnitude by $1/e$ [8]. The magnitude of the Debye length depends solely on the properties of the solution, and is inversely proportional to the ionic strength of the solution. Hence, if the salt concentration is high enough, the cloud of cations can screen the net charge of the micelle and drastically reduce the magnitude of inter-micellar interactions. Although it is difficult to characterize the counter-ion binding experimentally, molecular dynamics simulations suggest that the counter-ions bridges the head groups [25, 40-43]. These interactions will depend on the properties of the specific counter-ion used and have drastic effects on the size, structure and phase diagram of the micellar system [44]. It should be noted that the exact mechanisms of the ion binding are not fully understood, and more research using computer simulations combined with experimental techniques are needed to develop more accurate models.

Geometrically speaking, the shielding of the head group charges allows for denser packing since the effective area of the head groups, a_0, will decrease, thereby increasing the packing parameter p corresponding to elongated structures. A group of cone-shaped surfactant molecules will thus take a shape similar to that of a wedge, which can further assemble into discs and rods [36] as illustrated in Figure 10.

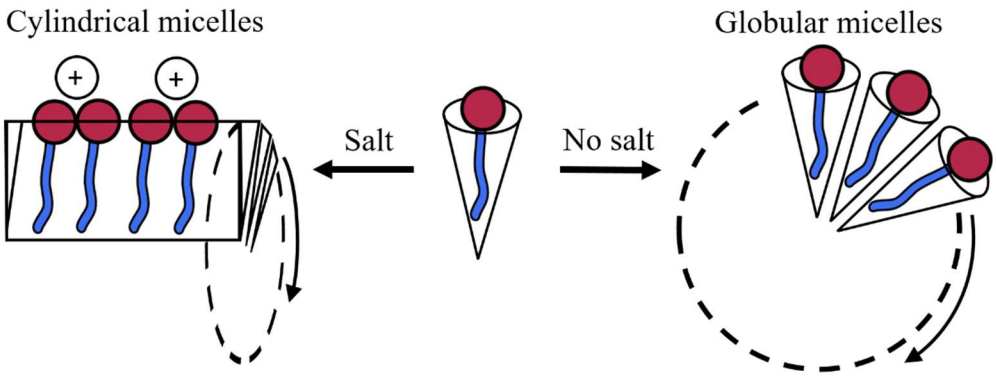

Figure 10: Electrostatic shielding causes denser packing of the surfactants and the preferred morphology changes from globular to cylindrical.

The free energy expression is for elongated micelles very different from the expression for spherical micelles as there is now have a less symmetrical shape with energy-unfavorable locations for the molecules at both ends. Now, there is a free energy μ_∞^0 which is length-independent and located away from the end caps. In addition, there is the energy of the end-caps, $2E_{end}$, described as energy per molecule due to it being distributed among all the molecules. This yields the following expression for the free energy as a function of the aggregation number N [39]:

$$\mu_N^0 = \mu_\infty^0 + \frac{2E_{end}}{N}. \tag{9}$$

A consequence of this is an exponential distribution in the size of the micelles and relatively high polydispersity in length, contrary to what was seen for globular micelles. It also leads to a strong dependence of concentration, c, on the aggregation number and micelle contour length L_c, usually following [39]:

$$N \propto L_c \propto \sqrt{c} \tag{10}$$

The added electrolytes do not only change the morphology of the micelles, but also the solubility of the surfactant and the so-called Krafft temperature. Usually, the solubility of an ionic surfactant is low at low temperatures with the molecules being present as a lyotropic phase. Beyond a certain point, however, the solubility increases rapidly. This is illustrated in Figure 11 where the temperature dependence of the solubility of a surfactant like SDS is shown. The point where the solubility curve meets the CMC line, is defined as the Krafft point, which also defines the Krafft temperature [36]. This is important since electrolytes can significantly increase the Krafft temperature and cause phase separation in solvent conditions were the surfactant was previously dissolved. Adding electrolytes to a solution of ionic surfactants will also reduce the CMC drastically [11] since the electrostatic shielding will reduce the free energy contribution from the head group repulsion and favor the formation of micelles.

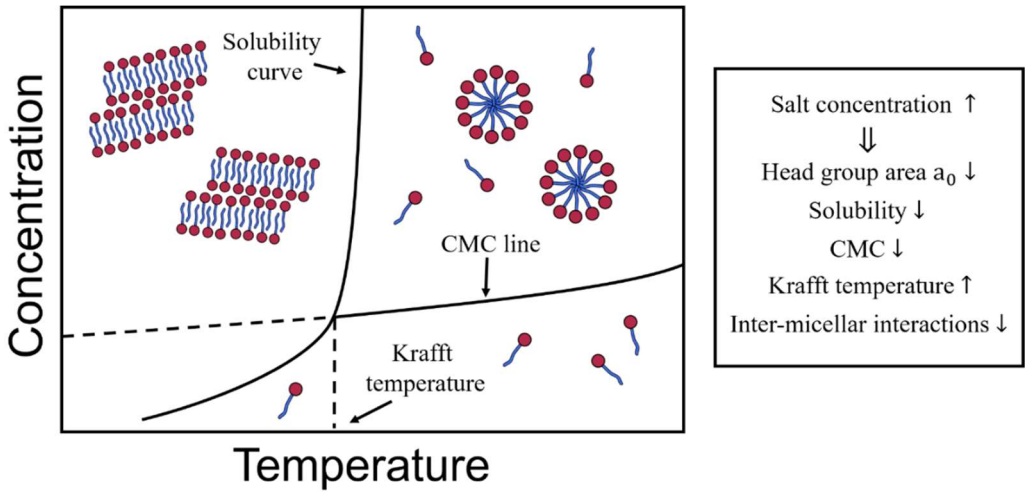

Figure 11: The figure to the left shows a conceptual diagram of the temperature dependence of the solubility of a surfactant such as SDS in aqueous solution. To the right, an overview of the effects of increased salt concentration on the same system can be seen.

Salts consists of a variety of anions and cations in various ratios. To compare the effect of different salts on the micelles, it is therefore convenient to introduce the molar ionic strength I of the solution given as

$$I = \frac{1}{2}\sum_{i=1}^{n} c_i z_i^2 \tag{11}$$

where c_i is the molar concentration of ion i and z_i is the charge of the same ion.

2.1.4 Diblock copolymer vesicles

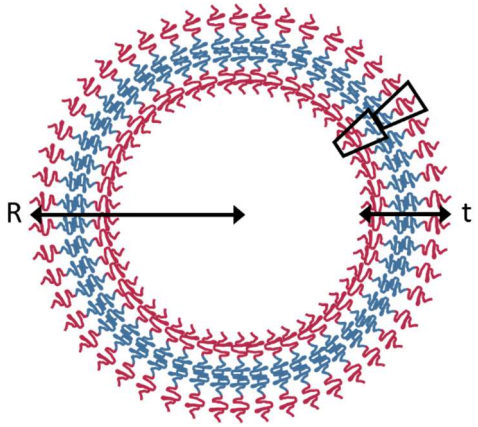

Figure 12: Sketch of a block copolymer vesicle illustrating the radius R and bilayer thickness t. In contrast to surfactant micelles, there is for vesicles an additional curvature dependence in the free energy term.

In the same way as surfactants, amphiphilic diblock copolymers self-assemble in aqueous solutions by solubilizing one part of the molecule but not the other, thereby forming self-assembled structures. If the

hydrophilic block is dominant in size, globular micelles are usually formed. As the length or volume of the hydrophilic bock is decreased relative to the hydrophobic part, however, cylindrical micelles and finally vesicles and flat bilayers are formed [26]. The balance between the attractive and repulsive forces will still give rise to an optimal surface area a_0, which is now defined as the area of the hydrophobic block at the interface between the two blocks. In terms of the packing parameter, p, bilayered structures are formed when this value lies close to unity which corresponds to a low curvature.

If the edges of a bilayer formed by copolymers can curve up and form a vesicle, the extra energy cost of having hydrophobic parts at the edges can be eliminated. However, this will also lead to an energy cost due to the curvature imparted on the bilayer. The balance between these two terms determines if the preferred morphology is planar bilayers or closed spherical vesicles. For surfactant micelles, the lateral attractive and repulsive forces between neighboring molecules were assumed to act in the same plane, but this is not the case for vesicles. The lack of fluidity in a bilayer give rise to a lateral chain pressure in the hydrophobic region at some distance D resulting in an additional curvature dependence in μ_N^0. The distance is positive and above the interface if hydrophilic block repulsion dominates, and negative and below the interface if hydrophobic block repulsion dominates. Including this effect, the mean energy per molecule in a bilayer vesicle is given as [8]

$$\mu_N^0 = 2\gamma a_0 \left[1 - \frac{2\pi Dt}{Na_0}\right] = 2\gamma a_0 \left[1 - \frac{Dt}{4R^2}\right] = \mu_\infty^0 - \frac{\gamma a_0 Dt}{2R^2} \tag{12}$$

where t is the thickness and R is the radius of the bilayer.

The increase in size of the hydrophobic block required to form vesicles also have an effect on other aggregate properties. Firstly, the increase of the hydrophobic part will drastically reduce the CMC due to it now being more unfavorable to have monomeric molecules in solution. Furthermore, it changes the dynamics within and between the aggregates. Micellar structures made from surfactants are usually highly dynamic, while copolymer vesicles are usually frozen, i.e. having slow or non-existent monomer exchange [7].

2.2 General scattering theory

The principles of the scattering of waves is fundamental to all scattering techniques, including small-angle X-ray scattering (SAXS) and small-angle neutron scattering (SANS) which is used in this work. When a beam of photons or neutrons scatters off an object, the recorded scattering pattern can be used to derive information about e.g. the shape and size of the objects. Theories explaining scattering events have been thoroughly described in many textbooks with some examples being references [45-48]. In the following section, a summary of the most important concepts and derivations of relevant scattering theory based on these sources will be presented.

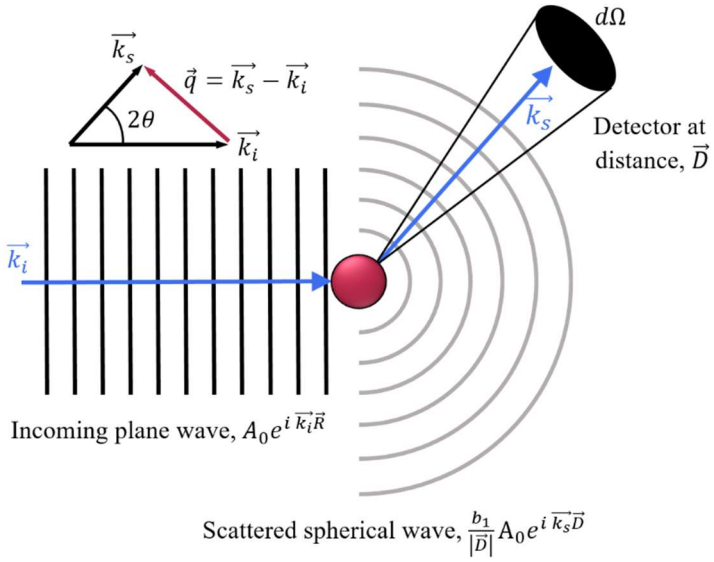

Figure 13: Illustration of a general scattering event and definition of the scattering vector $\vec{q}$.

In a general scattering event, illustrated in Figure 13, incoming radiation in the form of a plane wave interacts with a scatterer, i.e. an atom, which then scatters the wave spherically. For this to happen, the scatterer need to have an interaction potential with the incoming wave. If the kinetic energy of the incoming wave is much lower than this potential, the scatterer acts as an impenetrable wall at a certain distance b. This distance is referred to as the scattering length, and is a measure of the scattering power of the scatterer. If a low energy wave is scattered by a potential with scattering length b, it is the same as if this potential had the same properties as a sphere of radius b. Using this definition, one can define a scattering cross section

$$\sigma = 4\pi b^2 \tag{13}$$

being the effective area for the collision. Since electromagnetic radiation is scattered by electrons, the scattering length is determined by the classical electron radius (Thomson scattering length), and can easily be calculated. For neutrons, however, the radiation is scattered by the nuclei, and the interactions are thus caused by the nuclear force, requiring complex quantum mechanical theory to be described. This leads to both positive and negative scattering lengths for different nuclei as the potential can be either attractive or repulsive.

In several scattering techniques, including small-angle scattering, one assumes completely elastic scattering, meaning no exchange of energy between the incoming radiation and the sample. Hence, the magnitudes of the incident and scattered propagations vectors are equal to each other, and are given as

$$|\vec{k_i}| = |\vec{k_s}| = \frac{2\pi}{\lambda} \tag{14}$$

where λ is the wavelength of the incoming and scattered waves. The inelastic scattering will not be considered here as it only produces a background in small-angle scattering experiments.

The scattering vector or momentum transfer $\vec{q}$, also illustrated in Figure 13, is the independent variable measured in a typical scattering experiment. It is defined as the difference between the propagation vectors of the scattered and incident waves:

$$\vec{q} = \overrightarrow{k_s} - \overrightarrow{k_i} \tag{15}$$

From simple geometrical arguments, the magnitude of the scattering vector can be found to be

$$|\vec{q}| = \frac{4\pi}{\lambda} \sin\theta \tag{16}$$

where θ is the scattering angle. This means that the scale observed in a typical scattering experiment is inversely proportional to length.

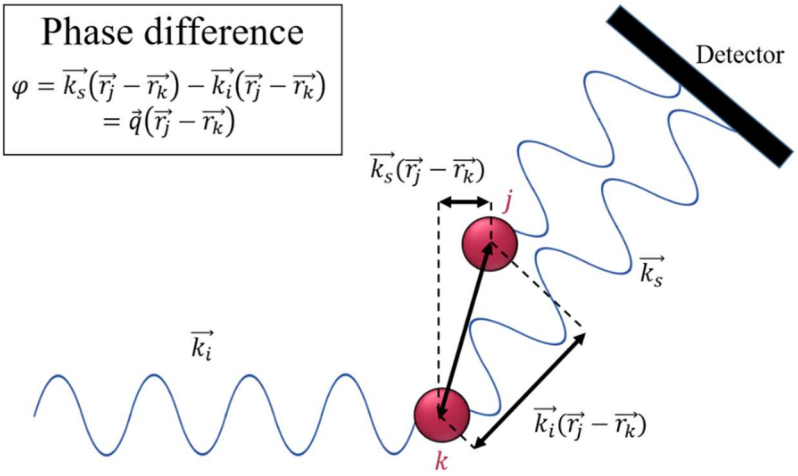

Figure 14: Two scatterers separated by a distance $\overrightarrow{r_{jk}} = \overrightarrow{r_j} - \overrightarrow{r_k}$ creates a phase shift φ in the scattered waves.

An incoming monochromatic plane wave at position $\vec{r}$ can be described as the probability amplitude

$$A_i(\vec{R}) = A_0 e^{i\,\overrightarrow{k_i}\vec{r}} \tag{17}$$

where A_0 is the amplitude. With the assumption that the scatterer can be considered as a point, the scattered wave from one scatterer located at the origin will be a homogenous spherical wave with the probability amplitude at a distance $\vec{D}$ given as:

$$A_1^s(\vec{D}) = \frac{b_1}{|\vec{D}|} \mathrm{A}_0 e^{i\,\overrightarrow{k_s}\vec{D}} \tag{18}$$

A realistic sample, however, will consist of countless scatterers, and the amplitude at a distance D will be a sum of the scattering amplitudes. Now, there are also interactions between the scattered waves and other scatterers. This is nevertheless not an issue in most scattering experiments when the so-called Born

approximation is valid [49]. Assuming the scattered field is small compared to the incident radiation, the total interacting field at each scattering center can be approximated with the incident radiation, which is usually valid for X-ray and neutron scattering. In this approximation, the scattered intensity measured at a detector will be the square of the sum of amplitudes from the individual scatterers. This will depend on the phase of the waves, and the phase difference will only depend on the relative positions of the scatterers if one assumes elastic scattering events. This yields the phase difference φ illustrated in Figure 14, and is given by:

$$\varphi = \overrightarrow{k_s}\left(\overrightarrow{r_j} - \overrightarrow{r_k}\right) - \overrightarrow{k_i}\left(\overrightarrow{r_j} - \overrightarrow{r_k}\right) = \vec{q}\left(\overrightarrow{r_j} - \overrightarrow{r_k}\right) \tag{19}$$

Now, when introducing a second atom at a distance $\vec{r}$ from the other atom located at the origin, interference occurs between the scattered waves due to the phase difference. The atom at the origin will still have the amplitude shown in Equation 18, while the scattering from the second atom will have a probability amplitude, now including an interference term correcting for the phase difference, given as:

$$A_2^s\left(\vec{D}, \vec{q}\right) = \left[\frac{b_2}{\left|\vec{D}\right|} A_0 e^{i\,\overrightarrow{k_s}\vec{D}}\right] e^{-i\vec{q}\vec{r}} \tag{20}$$

The scattering amplitude from both atoms at a detector at a distance $\vec{D}$ can then be described from the sum of these two amplitudes. Generalizing this to a system of N atoms at positions r_j with amplitudes A_j, the final probability amplitude of

$$A_s\left(\vec{D}, \vec{q}\right) = \sum_{j=1}^{N} A_j e^{-i\vec{q}\overrightarrow{r_j}} \tag{21}$$

is found by summing all the amplitude contributions and including the corrections from the phase differences. What is measured at a detector, however, is the scattered intensity which is given as the square of the amplitude given by

$$\langle I_s(\vec{q})\rangle = \langle A_s(\vec{D}, \vec{q}) \cdot A_s^*\left(\vec{D}, \vec{q}\right)\rangle = \frac{A_0^2}{D^2} \sum_{j,k=1}^{N} \langle b_j e^{-i\vec{q}\overrightarrow{r_j}} \times b_k^* e^{-i\vec{q}\overrightarrow{r_k}}\rangle \tag{22}$$

$$\Rightarrow \quad \langle I_s(\vec{q})\rangle = \frac{A_0^2}{D^2} \sum_{j,k=1}^{N} \langle b_j b_k e^{-i\vec{q}\overrightarrow{r_{jk}}}\rangle \tag{23}$$

where $\overrightarrow{r_{jk}} = \overrightarrow{r_j} - \overrightarrow{r_k}$. The term before the sum is merely an instrumental constant, and the intensity depends only on the scattering lengths and positions of the scatterers. It is also important to note that the phase information of the waves is lost by squaring the amplitudes. This is commonly known as the phase problem in diffraction, and makes it difficult to resolve a structure from the scattered intensity pattern as it prohibits a direct reconstruction of the structure.

Removing the constant in Equation 23, one is left with what is called the differential scattering cross-section. It is defined as the flux of scattered radiation, $d\sigma$, into a solid-angle element $d\Omega$ (illustrated in Figure 13). One can then normalize to the sample volume to obtain the more convenient expression:

$$\frac{d\Sigma}{d\Omega}(\vec{q}) = \frac{1}{V} \cdot \frac{d\sigma}{d\Omega}(\vec{q}) = \frac{1}{V} \sum_{j,k=1}^{N} \langle b_j b_k e^{-i\vec{q}\vec{r}_{jk}} \rangle . \tag{24}$$

This is the quantitative representation of the scattering interactions, and contains all information about the structure and is commonly used in the final data analysis.

In the case of neutron scattering, the scattering lengths in Equation 24 must be replaced with a distribution. This is because the scattering length will depend on which isotope is present a site and on the associated spin states. If one assumes uncorrelated and randomly distributed isotopes and spins, the scattering lengths can be replaced by the ensemble average $\langle b_j b_k \rangle$ which can for different sites be given as

$$\langle b_j b_k \rangle = \langle b_j \rangle \langle b_k \rangle = \langle b \rangle^2 \tag{25}$$

and for the same sites ($j = k$) be given as

$$\langle b_j b_k \rangle = \langle b_j^2 \rangle = \langle b^2 \rangle \tag{26}$$

Then, by splitting Equation 24 into different terms for scattering from different and same sites, one obtains the final expression

$$\frac{d\Sigma}{d\Omega}(\vec{q}) = \frac{1}{V} \sum_{j,k=1}^{n} \langle b \rangle^2 e^{i\vec{q}\vec{r}_{jk}} + \sum_{j} (\langle b^2 \rangle + \langle b \rangle^2) = \left[\frac{d\Sigma}{d\Omega}(\vec{q})\right]_{coherent} + \left[\frac{d\Sigma}{d\Omega}\right]_{incoherent} \tag{27}$$

where the differential cross-section is split up into a coherent and a $\vec{q}$-independent incoherent part. The coherent part contains all structural information about the sample, while the incoherent part caused by elastic scattering yields a flat background in a measurement.

2.2.1 Small-angle scattering theory

The theory of small-angle scattering using X-rays dates back to the 30's, and was well described in the book of Guinier and Fournet [50]. Small-angle neutron scattering, on the other hand, came later in the early 70's. The general small-angle theory is applicable to both SAXS and SANS, and an overview of this theory based on the concepts introduced above will be presented in this section. A sketch of the set-up of a general small-angle scattering experiment is given in Figure 15.

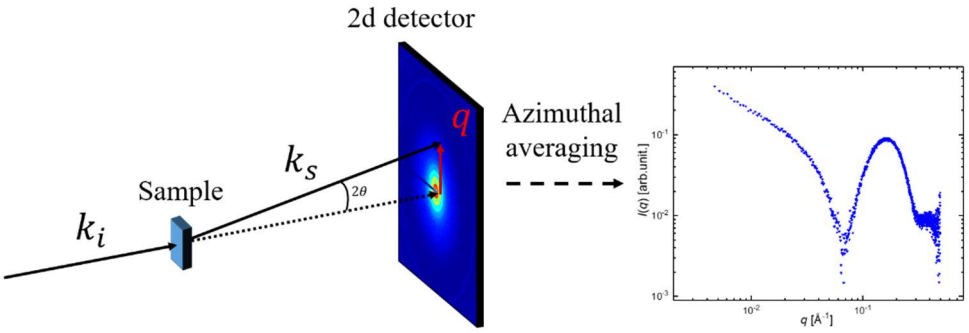

Figure 15: Sketch of a typical set-up of a small-angle scattering experiment and an example of the resulting scattering curve.

The scattering pattern of particles is determined by the interference between waves scattered by linear dimensions l such that $l \approx \frac{\pi}{q_{max}}$, with q_{max} being the maximum value of q gathered in the measurement [51]. Instead of concerning all the individual scattering lengths in a sample, one can introduce a scattering length density (SLD) $\rho(\vec{u})$ by taking the sum of all coherent scattering lengths in a scatterer and dividing by the volume of that scatterer. This density is given as

$$\rho(\vec{u}) = \frac{1}{v}\sum_i b_i(\vec{u}) \tag{28}$$

where b_i is the scattering length at position $\vec{u}$ of scatterer i.

The term contrast or excess scattering length can also be introduced and is defined as the scattering length density of the particle compared to the surroundings, usually a solvent, given as

$$\Delta\rho(\vec{u}) = \rho_p(\vec{u}) - \rho_s \tag{29}$$

where $\rho_p(\vec{u})$ is the particle scattering length density and ρ_s is the solvent scattering length density. The scattering amplitude from a particle in vacuum is then calculated by integrating the product of the excess scattering length density and a phase factor over the particle volume V_p. This is given by

$$A_s(\vec{q}) = \int_{V_p} \Delta\rho(\vec{u}) e^{i\vec{q}\vec{u}} d\vec{u}\,, \tag{30}$$

and can be recognized as the Fourier transform of $\Delta\rho(\vec{r})$. The differential scattering cross-section from one particle, Equation 24, can be reformulated with the concept of contrast, and is then given as

$$\frac{d\Sigma}{d\Omega}(\vec{q}) = \iint_{V_p} \Delta\rho(\vec{u})\Delta\rho(\vec{v})\, e^{-i\vec{q}(\vec{u}-\vec{v})}\, d\vec{u}\, d\vec{v} \tag{31}$$

where $\vec{u}$ and $\vec{v}$ are the intraparticle distances. Again, generalizing this to N number of particles at positions $\vec{r}$ relative to an arbitrarily chosen origin, one gets

$$\frac{d\Sigma}{d\Omega}(\vec{q}) = \frac{1}{V}\left(\sum_{j=1}^{N} e^{-\vec{q}\,\vec{r_j}} \int_{V_p} \Delta\rho(\vec{u}) e^{-i\vec{q}\,\vec{u}}\, d\vec{u}\right)\left(\sum_{k=1}^{N} e^{-\vec{q}\,\vec{r_k}} \int_{V_p} \Delta\rho(\vec{v}) e^{-i\vec{q}\,\vec{v}}\, d\vec{v}\right) \tag{32}$$

which is valid for both neutron and X-ray scattering.

Because the small-angle scattering experiments done in this work involves scattering from solutions, Equation 32 must be modified to account for the fact that all particles are randomly oriented and distributed by taking a positional and orientational average. Moreover, if the system is isotropic, the equation can be written as a function of the magnitude of the scattering vector $|\vec{q}|$ rather than $\vec{q}$, yielding a scattering pattern with circular symmetry. The expression is now given as:

$$\frac{d\Sigma}{d\Omega}(\vec{q}) = \frac{N}{V}\left\langle\left(\iint_{V_p} \Delta\rho(\vec{u})\Delta\rho(\vec{v}) e^{-i\vec{q}(\vec{u}-\vec{v})}\, d\vec{u}\, d\vec{v}\right)\left(\frac{1}{N}\sum_{j=1}^{N}\sum_{k=1}^{N} e^{i\vec{q}(\vec{r_j}-\vec{r_k})}\right)\right\rangle \tag{33}$$

The first main expression inside the brackets in Equation 33 accounts for scattering from single particles and yields what is known as the form factor $P(q)$. The second term accounts for the inter-particle interactions, and is known as the structure factor $S(q)$. Equation 33 is thus usually simplified into

$$\frac{d\Sigma}{d\Omega}(q) = \frac{N}{V} V_p \langle\Delta\rho\rangle^2 P(q) S(q) \tag{34}$$

where the form factor is defined as

$$P(q) = \iint_{V_p} e^{-i\vec{q}(\vec{u}-\vec{v})}\, d\vec{u}\, d\vec{v} \tag{35}$$

and the structure factor is defined as:

$$S(q) = \frac{1}{N}\sum_{j=1}^{N}\sum_{k=1}^{N} e^{i\vec{q}(\vec{r_j}-\vec{r_k})} \tag{36}$$

The form factor contains all information about the shape and size of the scatterers, and for some simple geometrical shapes the form factors are known analytically. Examples of form factors for some common shapes with their respective scattering curves can be seen in Figure 16.

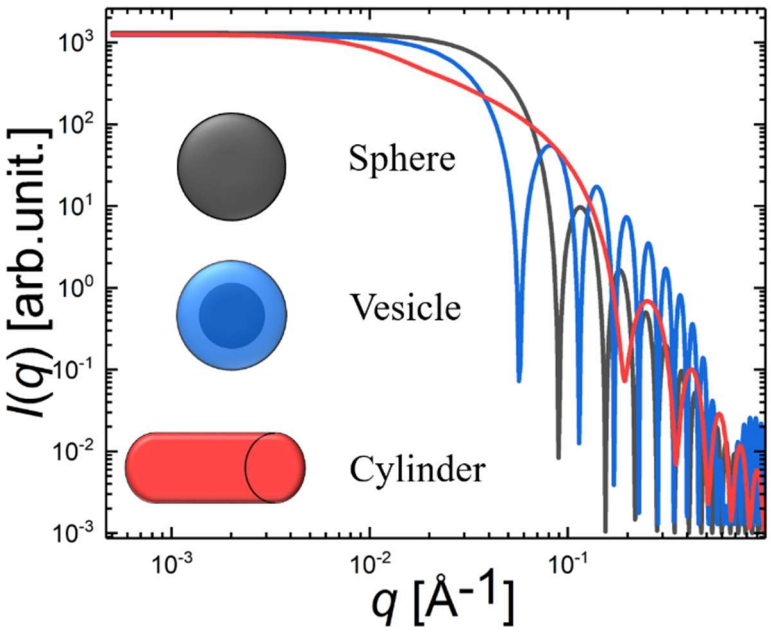

Figure 16: Schematic plots of form factors for a sphere, vesicle and cylinder. The particle dimensions used are: sphere radius 50 Å, vesicle radius 50 Å and thickness 10 Å, and cylinder radius 20 Å and length 400 Å.

The structure factor is usually approximated using analytically known interaction potentials and/or results from simulations. An experimental structure factor can also be found by dividing the scattering data with the form factor assuming the form factor is constant with variations in concentration. Since the interactions become less prominent with fewer particles, $S(q) \to 1$ as the concentration approaches zero. For dilute samples, one can thus assume the form factor and contrast to be the only contributors to the scattering curve.

In order to describe a real sample that contains particles with a distribution in size, polydispersity has to be accounted for in the scattering cross-section. This is done by integrating the form factor over a normalized distribution function $D(x)$ to create an average form factor of

$$\overline{P(q)} = \int D(x)P(q,x)\,dx \tag{37}$$

where x is the parameter with a distribution in size, e.g. radius or length. The size distributions can change the average aggregation number and have a smearing effect on the form factor compared to form factors from monodisperse particles. These effects can be seen in Figure 17 where the scattering from a polydisperse system (red) is compared to a monodisperse system (black).

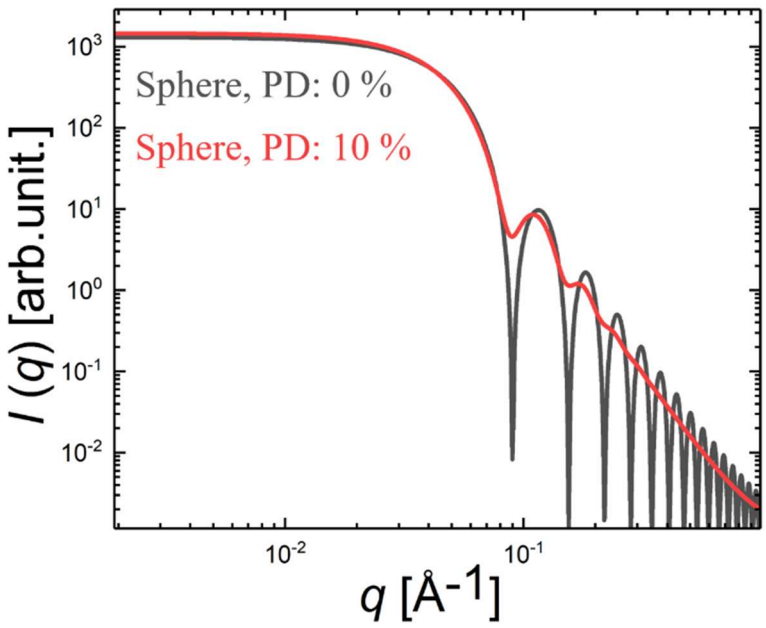

Figure 17: Schematic plots of the form factors of spheres (R = 50 Å) with a 0 % and 10 % distribution in the radii. Smearing caused by the size distribution can be seen at high q-values.

For a polydisperse system, one also has to introduce a modification to Equation 34 since $\langle|A_s(\bar{q})|^2\rangle \neq \langle|A_s(\bar{q})|\rangle^2$. In this case, the equation for the differential scattering cross-section must be on the form :

$$\frac{d\Sigma}{d\Omega}(q) = \frac{N}{V} V_p \langle\Delta\rho\rangle^2 P(q)\left(1 + \frac{\langle|A_s(\bar{q})|\rangle^2}{\langle|A_s(\bar{q})|^2\rangle}(S(q) - 1)\right) \tag{38}$$

Lastly, some important differences in the contrast for X-rays and neutrons which can be exploited in experiments should be mentioned. The scattering length for an atom interacting with X-rays scales with the number of electrons in the atom. It consequently increases proportionally to the atomic numbers and is constant for all isotopes of the same element. For neutrons, however, the scattering lengths of different isotopes can be drastically different and is no longer proportional to the atomic numbers. An important example is the difference in scattering power between hydrogen and its isotope deuterium. The scattering length of these isotopes are, respectively, $0.68 \cdot 10^{-12}$ cm and $-0.37 \cdot 10^{-12}$ cm [46]. Thus, by varying the ratio of H_2O and D_2O in the solvent, the contrast can be fine-tuned and thereby hide or highlight different components of the particles in the solution. If, for instance, the SLD of the solvent and the core of a particle are matched, one will only obtain scattering data for the particle shell. Furthermore, one can use these mixtures to study dynamics of water transport through particle membranes by preparing one batch of particles in H_2O and one batch in D_2O. If they are then mixed prior to measurement, the hydrogenated and deuterated water will diffuse through the membranes, and the resulting change in contrast can be used to study the kinetics.

2.2.2 Dynamic light scattering

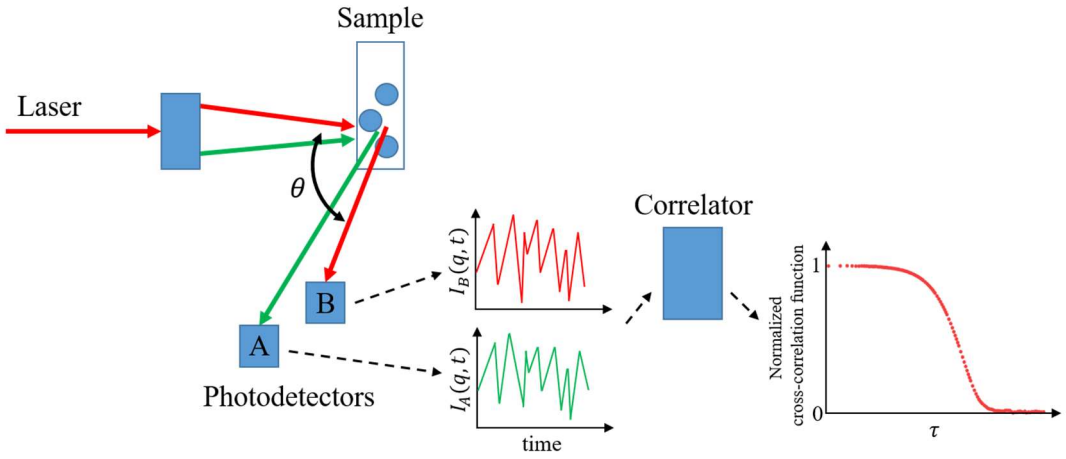

Figure 18: Set-up of a DLS instrument using photon cross-correlation spectroscopy (PCCS) which filters out signals from multiple scattering.

Dynamic light scattering (DLS) is a technique used to find the size distribution profile of sub-micron particles or polymers dispersed in a liquid. The theory and technical details are explained in numerous textbooks and publications, including [52-56], and the theory for DLS using photon correlation spectroscopy (PCS) and photon cross-correlation spectroscopy (PCCS) presented here is based on these. The set-up of a typical PCCS instrument can be seen in Figure 18.

DLS works by measuring the random Brownian motion of particles in solution and relating their diffusion rate to the hydrodynamic radius, thus obtaining information about the particle size. The hydrodynamic radius R_h is defined as the radius of a sphere with the same diffusion rate as the particles measured, and the two are related by the Stokes-Einstein relation [57]

$$R_h = \frac{kT}{6\pi\eta D} \tag{39}$$

where k is Boltzmann's constant, T is the temperature, η is the viscosity and D is the translational diffusion coefficient. In order to get an accurate hydrodynamic radius, precise and stable values of the sample temperature and viscosity are therefore needed. Moreover, the hydrodynamic radius is not only influenced by the actual particle size, but also the surface structure, concentration and the ionic strength of the solvent. These are important factors to consider when evaluating the obtained radius from DLS experiments, in addition to the fact that the evaluation methods described below is limited to single scattered light.

To obtain the diffusion coefficient arising from the particle's Brownian motion in DLS with PCS, one first illuminates a cuvette containing the sample with a laser. The scattered light is then detected at one or more angles as speckle patterns on the detector where the position of each speckle varies constantly due to the particle motion. Each speckle arises from the light scattered from particles which arrive with the same phase and interferes constructively to give a bright point. The rate of the fluctuations in intensity depends

on the particle speed and also particle size as seen in the Stokes-Einstein relation. While it is possible to measure the frequency spectrum of the intensity fluctuations directly, it is inefficient, and a device called a correlator is used instead.

The basic function of a correlator is to compare the similarity of two signals, or one with itself, at different time intervals. For a random signal, the correlation will go towards zero, and the decay time for this correlation is related to the diffusion speed. In DLS, the history of the intensity signal is compared over relatively long times with the full signals at a later time. One then obtains correlation functions which are commonly plotted against time on a log scale. Large particles will give a slowly changing signal which yields a correlation function decaying slower than one obtained from smaller particles.

The correlator will from correlating the intensity at different times t, calculate the so-called auto-correlation function $G_{(2)}(q,t)$ (or second-order correlation function). The normalized $G_{(2)}(q,t)$ is given by

$$g_{(2)}(q,\tau) = \frac{\langle I(t)I(t+\tau)\rangle}{\langle I(t)\rangle^2} \tag{40}$$

where τ is the time over which the correlation is measured. At short correlations times τ, the function is expected to go towards $g_{(2)}(q,\tau=0) = \frac{\langle I(t)^2\rangle}{\langle I(t)\rangle^2}$ as the change in intensity is very small. At long correlation times, the correlation is, as mentioned earlier, expected to approach zero. In terms of Equation 40, this means that $g_{(2)}(q,\tau) \to 1$ or $g_{(2)}(q,\tau) - 1 \to 0$.

Assuming that the detector only detects scattered light and that the photon counting is a random Gaussian process, the diffusion coefficient used to calculate the hydrodynamic radius can be found using the Siegert relation [58]:

$$g_{(2)}(q,\tau) = 1 + C|g_1(q,\tau)|^2 \tag{41}$$

Here, C is an instrumental constant related to optics and the incoherence of the laser beam, and $g_{(1)}(q,\tau)$ (normalized first-order correlation function) is the sum of all the exponential decays in the correlation function. Assuming a monodisperse solution, $\left|g_{(1)}(q,\tau)\right|$ is a single exponential given by

$$\left|g_{(1)}(q,\tau)\right| = e^{-\Gamma_c \tau} \tag{42}$$

where Γ_c is the decay rate which is related to the diffusion rate through the relation:

$$\Gamma_c = Dq^2 \tag{43}$$

The scattering vector q is here defined as

$$q = \frac{4\pi n}{\lambda}\sin\left(\frac{\theta}{2}\right) \tag{44}$$

where λ is the incoming laser wavelength, n is the refractive index of the sample and θ is the scattering angle.

For a polydisperse system, the particle diffusion is instead described using an integral over a distribution of decay rates $G(\Gamma_c)$ weighted by the intensity:

$$g_{(1)} = \int_0^\infty G(\Gamma_c) e^{-\Gamma_c \tau} d\Gamma_c \tag{45}$$

The single exponential of $g_{(1)}$ in Equation 42 can in that case be substituted by a stretched exponential function to account for size distribution

$$g_{(1)} = e^{-\left(\frac{\tau}{\tau_c}\right)^\beta} \tag{46}$$

where τ_c is the characteristic relaxation time, and β is a parameter which qualitatively accounts for the stretching of the exponential and approaches one for monodisperse samples. If $\beta = 1$, then $\tau_c = 1/\Gamma_c$ and Equation 46 becomes equal to Equation 42. If $\beta \neq 1$, the mean relaxation time $\langle \tau_c \rangle$ can be calculated from the integral of the stretched exponential function. This can be solved analytically, and the diffusion coefficient can then be calculated through the relation

$$\Gamma_c = \frac{1}{\langle \tau_c \rangle} = \frac{1}{\left[\frac{\tau_c}{\beta} \cdot \Gamma\left(\frac{1}{\beta}\right)\right]} = Dq^2 \tag{47}$$

where $\Gamma(x)$ is the gamma function. Hence, by relating the decay rate from the autocorrelation function to get the diffusion rate using Equations 43 and 47, one can through the Stokes-Einstein relation obtain the hydrodynamic radius of the particle.

As the evaluations above require single scattered light, accurate characterization of concentrated and turbid samples can be problematic due to multiple scattering. To overcome this problem, the technique of PCCS can be employed where only the single scattering signal is extracted. This is achieved by performing two scattering experiments on the same volume with the same scattering vectors, and then cross-correlating the obtained scattering signals as seen illustrated in Figure 17. The cross-correlation function is then obtained which corresponds to $g_{(2)}(q, \tau)$ in PCS and can be evaluated in the same way.

To obtain the size distributions from multimodal systems, a method such as the non-negative least squares (NNLS) method developed by Morrison et al. [59] can be used. It uses non-negativity constraints and geometrical spacing of the distribution using a Laplace transform on $g_{(1)}$ from Equation 45. Decay constants $\bar{\Gamma}$ corresponding to decay rates $G(\Gamma_c)$ are spaced over a chosen range of Γ. The coefficients b_i of Γ_i can then be obtained by a fit to the data by minimizing the following equation within the NNLS constraints [60]

$$X^2 = \sum_{j=1}^{N} \left[g_{(1)}(\tau_j) - \sum_{i=1}^{M} b_i e^{-\Gamma_i \tau_j} \right]^2 \tag{48}$$

where N is the number of data points and M is the number of decay constants having the constraint $\Gamma_i, b_i \geq 0$.

Distribution functions obtained from a method such as NNLS can be represented in distributions weighted by intensity, volume or number. Intensity weighted distributions scale with R^6, and the result will therefore be dominated by large particles. The volume weighted distribution is, however, less sensitive to large particles as it scales with R^3. Lastly, the number weighted distribution represents a real distribution of the sample without any dependence on the size of the particles.

2.3 Model-independent analysis

2.3.1 Indirect Fourier transform

Small-angle scattering experiments yields data in reciprocal space which can be analyzed by comparing analytical scattering models of the structure to the experimental data. Alternatively, structural information can be obtained in real space by analyzing the pair distance distribution function $p(\vec{r})$ which is related to the scattering intensity through an inverse Fourier transform. Small-angle scattering data is, however, finite, which causes an ill-posed problem when calculating the unbound integral in an inverse Fourier transform. This is often circumvented by using the so-called indirect Fourier transform (IFT) with the assumption that there is a value D_{max} for the maximum distance within the particle. Assuming an orientationally averaged sample, the relationship between the intensity and the pair distance distribution function is given by [61]:

$$I(\vec{q}) = 4\pi \int_0^{\mathrm{Dmax}} p(\vec{r}) \frac{\sin \vec{q}\vec{r}}{\vec{q}\vec{r}} \tag{49}$$

Since the pair distance distribution function is a description of the distribution of distances $\vec{r}$ between pairs of particles in a given volume, information about the shapes and sizes of the particles in the measured sample can be obtained. There are several methods which are used to accomplish this calculation, and these have been implemented in different software packages.

The distribution function is calculated by fitting the coefficients of the Fourier transform of a linear combinations of functions in r-space to the scattering data. The method of Glatter [62] is commonly used where N equidistant cubic B-splines $\phi_i(r)$ are used as the function set such that $p(r) = \sum_i c_i \phi_i(r)$. Due to the linearity of the transformation, the resulting $I(q)$ has the same coefficients c_i so that $I(q) = \sum_i c_i \chi_i$. The set of coefficients is then optimized by minimizing the function $L + \alpha N_c$ given by

$$L + \alpha N_c = \sum_{j=1}^{M} \left(\frac{I_{exp}(q_j) - \sum_i c_i \chi_i(q_j)}{\sigma(q_j)} \right)^2 + \alpha \sum_{i=1}^{N-1} (c_{i+1} - c_i)^2 \tag{50}$$

where $I_{exp}(q_j)$ is the experimental intensity and $\sigma(q_j)$ is the variance at point j. The first sum runs over M measured points and optimizes the fit quality to the experimental intensities, while the last sum controls the fluctuation of the coefficients. The minimization of the last sum yields a smooth $p(r)$ function without unphysical fluctuations and is controlled by the smoothness parameter α. Lastly, the fitted $I(q)$ is Fourier transformed to yield $p(r)$. In the case of unphysical fluctuations being present close to $r = D_{max}$, a new value for D_{max} is used and the calculation is repeated.

This IFT calculation is usually automated in the software yielding a plot of the pair distribution function and values for the gyration radius R_G, maximum dimension D_{max} and the smoothness parameter α. From the shape of the plot, one can estimate the rough shape of the particles measured using small-angle scattering. Some typical shapes can be seen in Figure 19. For a particle containing regions of both positive and negative contrast, there will also be negative contributions to $p(r)$ that might lead to negative values as seen in plot from the micelle in the figure. This is often the case for surfactant micelles where the hydrocarbon tail gives a negative contrast when measured using SAXS.

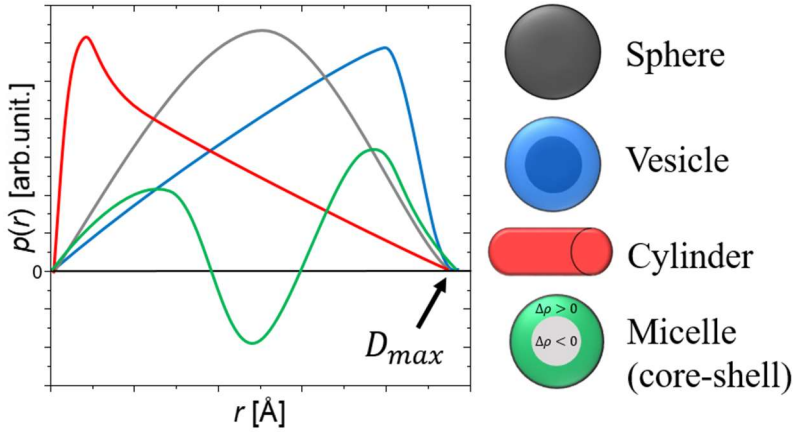

Figure 19: Schematic plots of the pair distribution functions for a sphere, vesicle, cylinder and a core-shell micelle. The negative values for the micelle is caused by oppositely signed contrasts for the core and shell. This is often the case for surfactant micelles measured using SAXS.

2.4 Data modeling

To obtain detailed structural information about micellar and bilayered structures, the small-angle scattering data can be compared to a calculated scattering pattern from a mathematical model. The different structural parameters of the model can then be iteratively changed until a satisfactory fit to the experimental data is obtained. This is done using a least-squares procedure to obtain a high quality fit and physically reasonable parameters with low uncertainties. A wide range of models which include different form factors $P(q)$ and structure factors $S(q)$ can be found in literature. The ones used in this thesis will be presented in the sections below.

The parameters obtained from the fit will be precise as long as the model is accurately describing the physical system and yields a good overlap between the fitted curve and the experimental data. There is, however, a maximum size r_{max} that can be resolved due to the limit in q-range estimated as [51]:

$$r_{max} = \frac{\pi}{q_{min}} \tag{51}$$

This makes it difficult to obtain values for the length or size of particles larger than r_{max}.

2.4.1 Core-shell scattering models

For most micelle forming surfactants and polymers studied by small-angle scattering, there is a substantial difference in the scattering length densities between the hydrophilic and hydrophobic parts of the molecules. The scattering from surfactant micelles must therefore be modeled using a core-shell structure as illustrated in Figure 20 with different contrast for the core and shell [39]. This can also be applied for more complex structures such as copolymers vesicles made and is explained in further detail in Section 2.4.5.

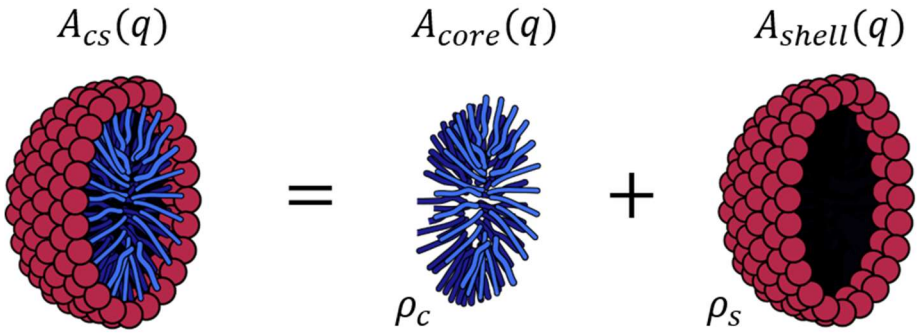

Figure 20: Illustration of how a micelle with substantial differences in scattering length densities between the head and tail groups can be modelled. The graphics are adapted from reference [14].

For surfactant micelles, the hydrophilic head groups form the shell with a scattering length density ρ_s, and the hydrocarbon chains constitute the core with a scattering length density ρ_c. The final scattering amplitude can then be written as a sum of the individual scattering amplitudes

$$A_{CS}(q) = (\rho_c - \rho_0) \cdot V_{core} \cdot A_{core}(q, R_{core}) + (\rho_s - \rho_0) \cdot V_{shell} \cdot A_{shell}(q, R_{shell}) \tag{52}$$

where V_{core}, ρ_c, V_{shell} and ρ_s are the volumes and scattering length densities for the core and shell, respectively, ρ_0 is the scattering length density for the solvent, and A_{core} and A_{shell} are the respective scattering amplitudes for the core and shell. The scattering cross-section is then given by

$$\frac{d\Sigma}{d\Omega}(q) = \frac{\phi}{NV_{sur}} \langle |A_{cs}(q)|^2 \rangle \tag{53}$$

where ϕ is the concentration, N is the aggregation number and V_{sur} is the surfactant volume.

2.4.2 Scattering model for ellipsoidal micelles

In pure water, surfactant molecules like SDS are known to form ellipsoidal micelles with a structure similar to the one illustrated in Figure 20 and Figure 21 [36]. An overview of the derivation of the form factor for this shape will be given in this section.

For a homogenous sphere with radius R, the scattering amplitude is given as [39]:

$$A_{sph}(qR) = \frac{3[sin(qR) - qRcos(qR)]}{(qR)^3} \tag{54}$$

When covering a wide q range, however, it is found that the form factor derived from the scattering amplitude from a sphere cannot represent the scattering data from SDS [39]. Therefore, a homogenous ellipsoid of revolution with aspect ratio ϵ and minor and major axes R_{core} and ϵR_{core} is introduced. It has a form factor $P_{ell}(q)$ including the scattering amplitude for the sphere given as

$$P_{ell}(q) = \Delta\rho^2 V_{ell}^2 \int_0^{\frac{\pi}{2}} A_{sph}(qr)^2 \, sin\,\alpha \; d\alpha \tag{55}$$

where $\Delta\rho$ is the scattering contrast, V_{ell} is the volume of the ellipsoid and $r = R(\sin^2\alpha + \epsilon^2\cos^2\alpha)^{1/2}$. The integration is needed to account for all possible orientations α of the ellipsoids.

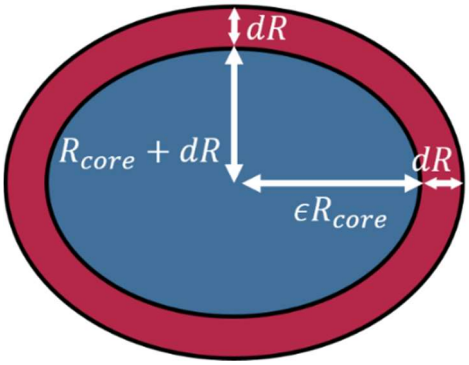

Figure 21: Cross-section of an ellipsoid showing the radii and shell thickness of the two axes as defined in the model.

Since the micelles in this case have a core-shell structure, a new form factor $P_{cs,ell}(qR)$ is constructed based on Equation 55 by summing the scattering amplitudes from the core and shell. For the core-shell ellipsoid, the total radii are given as $R_{tot} = R_{core} + dR$ and $\epsilon R_{core} + dR$, where dR is defined as the shell thickness, as illustrated in Figure 21. The aspect ratio of the total ellipsoid can be calculated using $\epsilon_{outer} = (\epsilon R_{core,} + dR)/(R_{core} + dR)$. The expressions for the volumes of the total ellipsoid, core and shell are given by $V_{tot} = \frac{4}{3}\pi\epsilon R_{tot}^3$, $V_{core} = \frac{4}{3}\pi\epsilon R_{core}^3$, and $V_{she} = V_{tot} - V_{core}$. Finally, the average form factor $\overline{P_{cs,ell}(q)}$ for the core-shell ellipsoids is given as:

$$\overline{P_{cs,ell}(q)} = \int_0^{\frac{\pi}{2}} [\Delta\rho_s V_{shell} A_{sph}(qr_{tot})^2 + (\Delta\rho_c - \Delta\rho_s) V_{core} A_{sph}(qr_{core})^2] \sin\alpha \, d\alpha \quad (56)$$

where $r_i = R_i(\sin^2\alpha + \epsilon_i^2 \cos^2\alpha)^{1/2}$ and $\Delta\rho_s$ and $\Delta\rho_c$ are the scattering contrasts for the shell and core, respectively.

2.4.3 Scattering model for short rod-like micelles

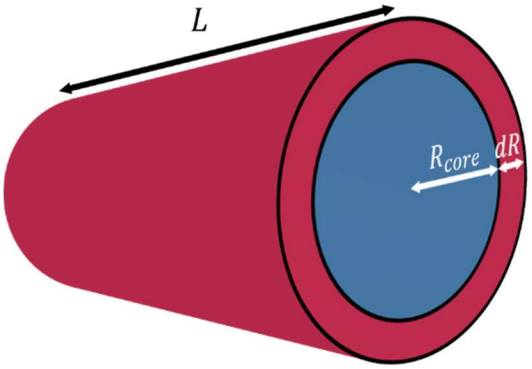

Figure 22: Sketch of a rod-like core-shell micelle with length L and radius $R_{tot} = R_{core} + dR$.

Surfactant molecules like SDS can also under certain conditions form short, rod-like micelles as shown in Figure 22. These cylindrical shapes with length L and radius R are known to have the orientationally averaged form factor [39]

$$\overline{P_{cyl}(q)} = \Delta\rho^2 V_{cyl} \int_0^{\frac{\pi}{2}} \left[\frac{2J_1(qR\sin\alpha)}{qR\sin\alpha} \cdot \frac{\sin\left(qL\cos\frac{\alpha}{2}\right)}{qL\cos\frac{\alpha}{2}} \right]^2 \sin\alpha \, d\alpha \quad (57)$$

where $\Delta\rho$ is the scattering contrast, $V_{cyl} = \pi R^2 L$ is the volume of the cylinder, and $J_1(x)$ is the first order Bessel function of first kind.

The cylindrical micelles still have a core-shell structure, and since the scattering amplitudes of these parts are additive, Equation 52 can be used to create a new form factor $\overline{P_{cs,cyl}(q)}$ for the core-shell cylinder structure

$$\overline{P_{cs,cyl}(q)} = \int_0^{\frac{\pi}{2}} \left[\Delta\rho_s V_{tot} \frac{2J_1(qR_{tot}\sin\alpha)}{qR_{tot}\sin\alpha} \cdot \frac{\sin\left(qL_{tot}\cos\frac{\alpha}{2}\right)}{qL_{tot}\cos\frac{\alpha}{2}} + (\Delta\rho_c - \Delta\rho_s) V_{core} \frac{2J_1(qR_{core}\sin\alpha)}{qR_{core}\sin\alpha} \cdot \frac{\sin\left(qL_{core}\cos\frac{\alpha}{2}\right)}{qL_{core}\cos\frac{\alpha}{2}} \right]^2 \sin\alpha \; d\alpha \quad (58)$$

where $\Delta\rho_s, L_{shell}, V_{shell}$, and $\Delta\rho_c$, L_{core} and V_{core} are the scattering contrasts, lengths and volumes for the shell and core, respectively, R_{core} is the core radius and $R_{tot} = R_{core} + dR$ is the total radius with head group thickness dR. It is worth mentioning that this model can be used for disc-like core-shell micelles by having $R_{tot} > L_{tot}$ [39].

The final expression can include a polydispersity in the length L, yielding the average form factor [39]

$$\overline{P_{cs,cyl}}(q) = \frac{\int_{L_{min}}^{L_{max}} \int_0^{\frac{\pi}{2}} L^2 f(L) P_{cs,cyl}(q)\, d\alpha\, dL}{\int_{L_{min}}^{L_{max}} L^2 f(L)\, dL} \tag{59}$$

where $f(L)$ is an exponential size distribution given as $f(L) = e^{-L/L_{ave}}$ with an average length L_{ave}. The lower and upper bounds of the integrals account for the minimum and maximum sizes of the micelles, respectively.

2.4.4 Scattering model for long rod-like and worm-like micelles

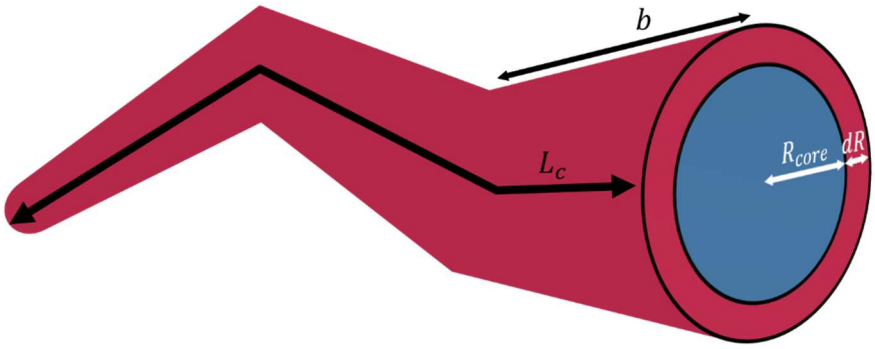

Figure 23: Sketch of a worm-like core-shell micelle with contour length L_c, Kuhn length b and radius $R_{tot} = R_{core} + dR$.

The cylindrical micelles described above can under some conditions become very long and form so-called «worm-like» micelles which are illustrated in Figure 23 [11, 12, 39, 63]. These may no longer be rigid, and may therefore contain a statistical segment length known as the Kuhn length b describing the flexibility of the cylinder. It furthermore becomes difficult to calculate the integral in Equation 58 numerically when $L_c \gg R$. A new analytical model is therefore necessary for the cases of both long non-flexible (rod-like) and flexible micelles (worm-like).

These core-shell micelles will still have a core radius R_{core}, a total radius $R_{tot,} = R_{core,} + dR$ and a contour length L_c. The total volume is given as $V_{tot} = \pi R_{tot}^2 L_c$, and the core volume is given by $V_{core} = \pi R_{core}^2 L_c$. Not that for non-flexible micelles $b \geq L_c$ and $L = L_c$.

When the length of the cylinder becomes long in relation to its radius, the form factor can be decoupled into factors including the contributions from the spherical cylinder cross-section $A_{cr}(Q)$ and the cylinder length $P_L(q)$, thereby overcoming the technical difficulties of the previously mentioned integral. The form factor $P_{cs,long\ cyl}(q)$ is then given as [39]

$$P_{cs}(q) = [\Delta\rho_s V_{tot} A_{cr}(qR_{tot}) + (\Delta\rho_c - \Delta\rho_s) V_{core} A_{cr}(qR_{core})]^2 \, P_L(q) \quad (60)$$

where

$$A_{cr}(x) = \frac{2J_1(x)}{x} \quad (61)$$

with $J_1(x)$ being the first order Bessel function of first kind. For non-flexible cylinders, the form factor $P_L(q)$ is given by the that of an infinitely thin cylinder given by

$$P_L(q) = L^2 \left[\frac{2\mathrm{Si}(qL)}{qL} - 4\sin^2\left(\frac{\frac{qL}{2}}{q^2L^2} \right) \right] \quad (62)$$

where Si signifies the antiderivative of the sinc function and the normalization requires $P_L(q = 0) = L^2$. The scattering from the worm-like micelles in the longitudinal direction is instead given by the form factor $P_{chain}(q, L, b)$ explained in references [64, 65] and is not shown here due to its complexity. Computer simulation studies [11, 64, 65] have shown that $P_{chain}(q, L, b)$ can be written as a combination of the contributions from an infinitely thin rod with length L, and from a flexible chain with contour length L_c and Kuhn length b. This means that the function follows the scattering from the rod at high q, and that of a flexible chain at low q. This has previously been applied with success to SDS dissolved in concentrated salt solutions where they are known to form these worm-like structures [11, 12].

Based on this, the final expression including polydispersity in the contour length L_c, gives the average form factor [39]

$$\overline{P_{cs,worm}(Q)} = \frac{\int_{L_{min}}^{L_{max}} L^2 f(L) P_{cs}(q, L, b) dL}{\int_{L_{min}}^{L_{max}} L^2 f(L) dL} \quad (63)$$

where $f(L_c)$ is the same exponential size distribution given as $f(L_c) = e^{-L_c/L_{mean}}$ with an average length L_{mean}. The lower and upper bounds of the integrals account for the minimum and maximum sizes of the micelles, respectively.

2.4.5 Scattering model for block copolypeptide vesicles

Potential vesicles formed by PLL-PBLG will consist of a water filled core surrounded by a bilayer which can be modelled as a hollow sphere composed of three shells. Going from the core and out, the vesicle will consist of a shell of hydrophilic PLL blocks, a shell of hydrophobic PBLG blocks and finally an outer shell of PLL blocks. Moreover, some overlap between the shells are expected in addition to inhomogeneity due to polymer swelling. This requires the implementation of a radial density profile containing gradually

decaying surfaces. The model presented here is based on the model in reference [66] which was successfully applied to a similar structure.

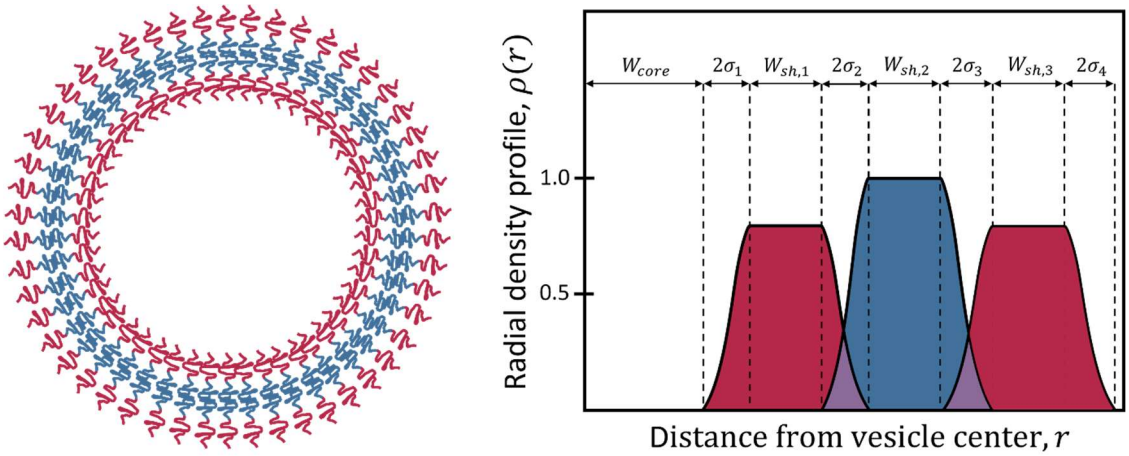

Figure 24: Schematic plot of the radial density profile used in the scattering model for block copolypeptide vesicles illustrating the meaning of the widths W of the core and shells, and the widths 2σ of the graded interfaces. The plot is adapted from reference [66].

The radial density profile $\rho(r)$ of the vesicle, illustrated in Figure 24, can be expressed through the half-height radius $R = W + \sigma$ using a parabolic shape, where W describes the width of the core or shell with constant density, and σ is the half-width of the graded interface:

$$\rho(r) = 1 \quad r \leq (R - \sigma) \tag{64}$$

$$\rho(r) = 1 - \frac{1}{2}\frac{[(r - R) + \sigma]^2}{\sigma^2} \quad (R - \sigma) < r \leq R \tag{65}$$

$$\rho(r) = \frac{1}{2}\frac{[(R - r) + \sigma]^2}{\sigma^2} \quad R < r \leq (R + \sigma) \tag{66}$$

$$\rho(r) = 0 \quad (R + \sigma) < r \tag{67}$$

By doing an analytical Fourier transform of the presented radial density profile, the following expression for the scattering amplitude is obtained

$$\Phi(q, R, \sigma) = \frac{1}{V_n}\left[\left(\frac{R}{\sigma^2} + \frac{1}{\sigma}\right)\frac{\cos\big(q(R + \sigma)\big)}{q^4} + \left(\frac{R}{\sigma^2} - \frac{1}{\sigma}\right)\frac{\cos\big(q(R - \sigma)\big)}{q^4}\right.$$
$$\left. - \frac{3\sin\big(q(R + \sigma)\big)}{q^5\sigma^2} - \frac{3\sin\big(q(R - \sigma)\big)}{q^5\sigma^2} + \frac{2\cos(qR)}{q^5\sigma^2} + \frac{6\sin(qR)}{q^5\sigma^2}\right] \tag{68}$$

where the volume of the vesicle is given as $V = 4\pi V_n$ where $V_n = \frac{R^3}{3} + \frac{R\sigma^2}{6}$ and the amplitude is normalized such that $\Phi(q = 0, R, \sigma) = 1$.

The scattering amplitudes of the individual shells can now be found in a way similar to the core-shell approach explained in Section 2.4.1. This is done by finding the difference in scattering amplitudes at different radii R and interfaces σ weighted by the volumes of the shell which yields the amplitudes

$$A_{sh,1}(q, R_{sh,1}, \sigma_2, \Delta\rho_{\mathrm{sh},1}, R_{core}, \sigma_1) = \Delta\rho_{sh,1}\left(V_{sh,1}\Phi(q, R_{sh,1}, \sigma_2) - V_{core}\Phi(q, R_{core}, \sigma_1)\right) \quad (69)$$

$$A_{sh,2}(q, R_{sh,2}, \sigma_3, \Delta\rho_{\mathrm{sh},2}, R_1, \sigma_2) = \Delta\rho_{sh,2}\left(V_{sh,2}\Phi(q, R_{sh,2}, \sigma_3) - V_1\Phi(q, R_1, \sigma_2)\right) \quad (70)$$

$$A_{sh,3}(q, R_{sh,3}, \sigma_4, \Delta\rho_{\mathrm{sh},3}, R_2, \sigma_3) = \Delta\rho_{sh,3}\left(V_{sh,3}\Phi(q, R_{sh,3}, \sigma_4) - V_2\Phi(q, R_2, \sigma_3)\right) \quad (71)$$

where $\Delta\rho_{sh,n}$ and $V_{sh,n}$ are the scattering length density and volume of shell n, respectively. The core is assumed to be filled with the same solvent as on the outside, and its scattering amplitude is therefore not included.

Because it is likely to be water present in the hydrophilic regions of the shells, the fraction of water in the inner shell, f_{wi}, and outer shell, f_{wo} was introduced in the calculations of the scattering length densities. The fractions were calculated using the fit parameter f.

The form factor $P(q)$ can now be calculated as the square of the sum of scattering amplitudes $A_{tot}(q)$:

$$A_{tot}(q) = A_{sh,1}(q, R_{sh,1}, \sigma_2, \Delta\rho_{\mathrm{sh},1}, R_{core}, \sigma_1) + A_{sh,2}(q, R_{sh,2}, \sigma_3, \Delta\rho_{\mathrm{sh},2}, R_1, \sigma_2) + A_{sh,3}(q, R_{sh,3}, \sigma_4, \Delta\rho_{\mathrm{sh},3}, R_2, \sigma_3) \quad (72)$$

In contrary to short surfactant molecules, polymers can exhibit significant local short-range correlations of polymer segments in the presence of water. These correlations contribute to the scattering patterns at q-values corresponding to the length scales where the internal parts of the polymer chains, known as blobs, are visible. A contribution $\frac{d\Sigma}{d\Omega_{blob}}(q)$ known as "blob scattering" based on the form factor of random-walk Gaussian chains given by Debye [67] can then be added to the final differential scattering cross-section to account for this effect. This introduces the fit parameter R_G being the radius of gyration related to the blob scattering.

The final differential scattering cross-section for the block copolypeptide vesicles is now

$$\frac{d\Sigma}{d\Omega}(q) = \frac{\phi}{V_{dry}}\langle|A_{\mathrm{tot}}(q)|^2\rangle + \frac{d\Sigma}{d\Omega_{blob}}(q) \quad (73)$$

where ϕ is the volume fraction of the vesicles and V_{dry} is the dry volume of the shells.

2.5 Interactions and structure factors

2.5.1 Charged globular micelles

Since surfactant molecules like SDS are charged, they form micelles with strong columbic interactions. The strength of these interactions increases with the surfactant concentration resulting in a structure factor contribution in the scattering data. This must consequently be taken into account in the modeling for some systems.

For charged globular micelles, one can introduce the hard sphere interaction potential

$$V(r) = \frac{e^2 Z^2}{4\pi\epsilon_p(1+\kappa R_{hs})r} e^{-\kappa(r-2R_{hs})} \tag{74}$$

for particle distances $r > R_{HS}$ with $V(r) = \infty$ for $r \leq R_{HS}$. R_{HS} is the hard-sphere radius, e is the elementary charge, Z is the number of charges per particle, ϵ_p is the solvent permittivity and $\frac{1}{\kappa}$ is the Debye screening length. The structure factor can be deduced from this potential and the resulting analytical expression can be found in the article by Hayter and Penfold [68]. Using this structure factor, one introduces the fit parameters R_{HS}, Z and scale factor S_{SQ} yielding the hard-sphere volume fraction $\eta = S_{SQ}\phi$ where ϕ is the volume fraction of surfactant in the solution.

2.5.2 Charged cylindrical micelles

For cylindrical and worm-like micelles, the structure factor is more complex as it involves both inter- and intra-chain interactions, and there are no analytical expressions available. Nonetheless, there are two good approximations available known as the random-phase approximations (RPA) [69] and the polymer reference interaction site model (PRISM) [70]. The PRISM model uses a continuum theory of polymers where each chain in the system is modeled as having "sites" that interact with "sites" on other chains. An empirical structure factor from the PRISM theory is given by the expression

$$S(q) = \frac{1}{1+\beta c(q) P_{\mathrm{rod}}(q, L-2R)} \tag{75}$$

where $c(q)$ is the direct correlation function between sites on the rod, and the parameter β can be calculated from the structure factor at $q = 0$. The form factor for a homogenous rod P_{rod} with length L and radius R is given as

$$P_{rod}(q) = \frac{2Si(qL)}{qL} - \frac{4\sin^2\frac{qL}{2}}{q^2L^2} \tag{76}$$

where Si signifies the antiderivative of the sinc function.

2.6 Microscopy

2.6.1 Transmission electron microscopy

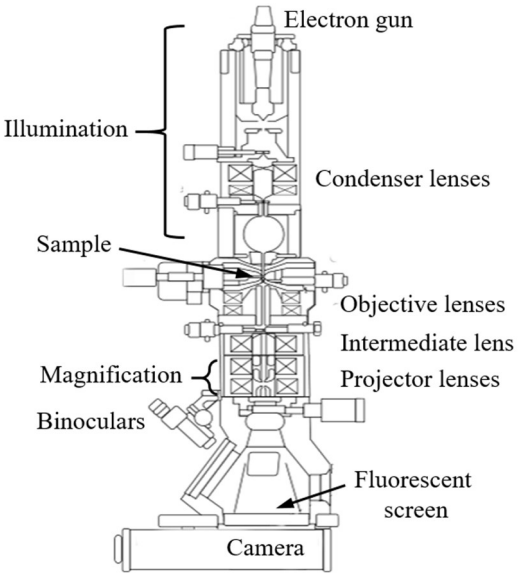

Figure 25: Sketch of a typical transmission electron microscope set-up (adapted from reference [71]). An electron beam is generated at the top and runs through a series of lenses and apertures that focuses, magnifies and collimates the beam. The intensity of the electrons transmitted through the sample are detected using a fluorescent screen at the bottom.

Structural information obtained from small-angle scattering techniques is derived indirectly through modeling of reciprocal space data and represents the average particle structure present in a solution. It is consequently useful to complement small-angle scattering data with direct structural information obtained from real-space images using a transmission electron microscope (TEM). This technique generates images with far higher magnification and resolution than conventional light microscopy. A TEM works in a similar way as a transmission light microscope, but instead of using photons for illumination, it uses a focused beam of electrons. Due to the much shorter wavelength of the electron compared to visible light, it is possible to reach sub-nanometer resolution on biological and other soft materials. The theory describing TEM can be found in numerous textbooks and reviews, and a summary of the theory relevant to the study of self-assembled nanostructures based on references [72-74] will here be presented.

In TEM, an image is formed as electrons transmitted through a thin sample produces bright and dark spots depending on the transmitted intensity on a fluorescent screen. This is known as bright field imaging and is the imaging method most commonly used for soft materials. A typical set-up of a TEM can be seen in Figure 25. The electrons are emitted at the top of an evacuated tube by a cathode referred to as the electron gun and then accelerated by an electric potential of up to several 100 keVs towards the anode below. The electron gun is composed of a filament made of a heavy-duty material such as tungsten, crystalline LaB_6 or a field emission filament. A series of apertures and electromagnetic lenses above and below the sample are then used to modify the beam and produce an image. Above the sample, condenser lenses control the sample illumination by varying the beam focus, size and intensity. The objective lenses

below the sample focus the transmitted beam and applies some magnification. Next, an intermediate lens and aperture control the focal plane enabling a change from real space imaging to reciprocal space imaging. This allows for the detection of diffraction patterns arising from crystalline samples. Projector lenses further magnify the beam and projects it onto a fluorescent screen creating an image which can be seen directly through a pair of binoculars or on a computer screen with a charge-coupled device (CCD) camera as the input source.

Using TEM with soft and biological materials imposes several limitations on the choice and preparation of samples which are not encountered to the same extent in techniques such as light microscopy and small-angle scattering. Most importantly, to allow for an adequate transmission of electrons, the samples must be extremely thin (~ 100 nm) or alternatively suspended on a coated metal grid. Moreover, since the electron beam operates in high vacuum, the sample must be completely dry, thereby precluding direct imaging of particles in solution as opposed to in certain other techniques. To overcome these challenges, methods including drying, staining and rapid freezing (cryo-TEM) can be applied for hydrated samples.

Drying is the easiest and most accessible sample preparation method a for the study of self-assembled nanostructures with TEM, and is the method applied in this work. This is done by placing a droplet of the sample solution on a polymer or carbon coated metal grid and allowing it to dry for up to several hours. The sample may also be stained by an electron dense chemical like uranyl acetate prior to drying to improve contrast in the imaging. To be representative of the structures in solution, the imaged nanostructures must exhibit exceptional structural stability and also insensitivity to the dramatic increase in concentration upon drying. The final images can therefore include additional structures arising from the drying process and from interactions with the grid, but also residues from the solvent and staining procedure. It is thus important to interpret the images with caution and use complementary techniques to support the findings [74].

3 Experimental

3.1 Sample preparation

All stock solutions used in this work were prepared gravimetrically using a 0.1 mg precision scale (CP224S from Sartorius, Germany) as close in time to the measurements as possible. The precision of the concentrations are discussed in the Appendix Section 6.2, and a list of all chemicals used in the experiments conducted in this thesis can be found in the Appendix Section 6.1.

3.1.1 SDS solution protocol

All SDS solutions were prepared using the solvents in Table 1 and the following protocol.

Salts were weighed out according to the concentrations in Table 1 and dissolved in Milli-Q water while stirring. The volume of the water was measured using a volumetric flask. Next, SDS (Sigma Aldrich ≥ 99.0%) was weighed out to yield stock solutions of 50. mg/mL SDS for each concentration of NaCl and $MgCl_2$, and 13 mg/mL SDS for each concentration of KCl and $CaCl_2$. The SDS powder was then added to the solvents with gentle swirling, before they were stored at ~4 ° C. The samples were prepared as close in time as possible to the experiments to avoid potential hydrolysis reactions of SDS in aqueous solution that could impact the results [16, 75].

The day prior to scattering experiments, the stock solutions were diluted with their respective solvents using a micropipette to yield the SDS concentrations listed in Table 1. The prepared solutions were equilibrated at ~37 ° C in a heating chamber for ~12 hours before the measurements.

Table 1: Overview over solvent and SDS concentrations used in the scattering experiments. The highest concentrations of SDS was used as stock solutions. The precision of the concentrations are discussed in the Appendix Section 6.2.

Solvent	c_{salt} [M]	c_{SDS} [mg/mL]
H_2O	N/A	6.3, 13, 25, 50.
NaCl in H_2O	0.100, 0.250, 0.400, 0.500, 0.550, 0.600, 0.650, 0.750, 0.850, 1.00	6.3, 13, 25, 50.
$MgCl_2$ in H_2O	0.0835, 0.167, 0.250, 0.333, 0.500	6.3, 13, 25, 50.
KCl in H_2O	0.005	6.3, 13
$CaCl_2$ in H_2O	0.005	6.3, 13

3.1.2 Buffer and salt solution preparation protocols

Certain PLL-PBLG copolypeptide samples used buffers or salt solutions as solvents that were prepared using the protocols presented below. An overview over the buffers used, their measured pH and their molarity can be found in Table 2.

The amounts of the buffer components required to achieve the desired pH and molarity were found in buffer tables in literature or calculated using the Buffer Maker software [76]. The components were weighed out and dissolved in Milli-Q water (except for tris buffer that was dissolved in D_2O) while stirring and measuring the pH using a freshly cleaned pH meter (827 pH Lab from Metrohm, Switzerland). If the right pH was not reached at this point, it was carefully adjusted by adding small amounts of one of the buffer components. The buffer was allowed to equilibrate before doing these adjustments. If needed, the buffer was diluted to achieve the right molar concentration. After reaching the correct values, the flask was sealed and stored at 4 ° C.

In addition to the buffers, aqueous solutions of NaCl were made in concentrations of 0.0625 M, 0.125 M, 0.250 M and 0.500 M. The required amounts of salt were weighed and dissolved in Milli-Q water while stirring, and the solutions were finally stored at ~4 ° C.

Table 2: pH and molarities of buffers used to dissolve PLL-PBLG polypeptides prior to SAS measurements.

Buffer	**pH**	**Molarity [mM]**
Citric acid / NaOH	3.50	50
Citric acid/ Na_2HPO_4	3.50	50
Tris	7.40	50
Tris (D_2O)	7.40	50
Tris	9.00	50
CHES / NaOH	9.00	50
CAPS / NaOH	10.0	50
Na_2CO_3 / $NaHCO_3$	9.00	50
NaH_2PO_4 / NaOH	11.5	50

3.1.3 PBLG-PLL solution preparation protocol

The PBLG-PLL (poly-γ-benzyl-l-glutamate-block-poly-l-lysine) diblock copolypeptides were synthesized by Hermis Iatrou et al. at the National and Kapodistrian University of Athens, Greece, using ring opening polymerization of the corresponding a-aminoacid N-carboxyanhydrides [29, 30]. The copolypeptides were synthesized with three different PLL block lengths and an almost constant PBLG block length. The molecular characteristics reported by the research group that synthesized the copolypeptides can be seen in Table 3.

All stock solutions (5.0 mg/mL or 10. mg/mL), regardless of the buffers/salt solutions used, were prepared using the following protocol.

First, the powdered polypeptides were carefully weighed gravimetrically into 1.5 mL Eppendorf tubes before adding the buffer, salt solution or Milli-Q water using a micropipette. After gentle swirling by

hand, the solution was allowed to swell at room temperature for ~1 h. Next, the tube was heated in a water bath at~ 50 ℃ for 60 minutes. The tube was then sealed and stored at 4 ° C until the day of measurements.

If needed, the stock solutions were diluted with the respective buffers using a micropipette to yield the desired concentrations, and then allowed to equilibrate at ~37 ℃ for ~8 h prior to the scattering experiment.

Table 3: Molecular characteristics of the PBLG-PLL copolypeptides used in this work. Note the varying length of the PLL blocks compared to the almost constant length of the PBLG blocks.

Polymer	Block length	$\overline{M_n}$ [gmol^{-1}], PBLG	$\overline{M_n}$ [gmol^{-1}], PLL	$\overline{M_n}$ [gmol^{-1}], Total	%w/w. PBLG-PLL	$\frac{\overline{M_w}}{\overline{M_n}}$
PBLG-PLL I	$PBLG_{60}$-*b*-PLL_{82}	13000	10500	23500	59.8 – 40.2	1.12
PBLG-PLL II	$PBLG_{74}$-*b*-PLL_{120}	16100	15500	31600	50.3 – 49.7	1.11
PBLG-PLL III	$PBLG_{70}$-*b*-PLL_{151}	15200	19400	34600	39.8 – 60.2	1.13

3.1.4 Transmission electron microscopy sample preparation protocol

Transmission electron microscopy requires special sample preparation. In this case the samples were dried, stained and embedded on a fine metal mesh before use. The sample preparation protocol presented in the next paragraph was used for all samples imaged in this work, and was based on the protocol described in reference [74].

15 μL of the sample solution was first placed on a piece of Parafilm, before a 100 mesh carbon/Formvar coated copper grid (FCF100 from Electron Microscopy Sciences, Hatfield, USA) was placed on top of the droplet and allowed to incubate for 5 minutes. The grid was then washed three times by placing it on fresh droplets of Milli-Q water before removing the excess water with filter paper. To stain the sample, the grid was transferred to a droplet of 4 % aqueous uranyl acetate and allowed to incubate for 1 minute. Excess liquid was once again absorbed with filter paper. The grid was then put in a Leica Reichert grid box and stored at ~4 ℃ the day prior to imaging.

3.2 Characterization techniques

3.2.1 Synchrotron SAXS

The main SAXS measurements in this work were done at the BM29 BioSAXS and ID02 ultra-SAXS beamlines at the European Synchrotron and Radiation Facility (ESRF) in Grenoble, France [77, 78]. In addition to these, the Bruker Nanostar SAXS system at the Department of Chemistry, University of Oslo, was used for complementary measurements. The instrument set-ups, specifications and data treatment procedures used in this work will here be presented.

The synchrotron produces a high brilliance X-ray beam which is highly monochromated and collimated in a pinhole configuration at both BM29 and IDO2. This is illustrated in the photograph of the instrument at BM29 shown in Figure 26. For all measurements in this work expect for the temperature scans, the temperature of the capillary was set to 37 °C. This was done to go above the Krafft temperature of SDS at the highest salt concentrations, in addition to the relevance of the temperature in biological systems and applications.

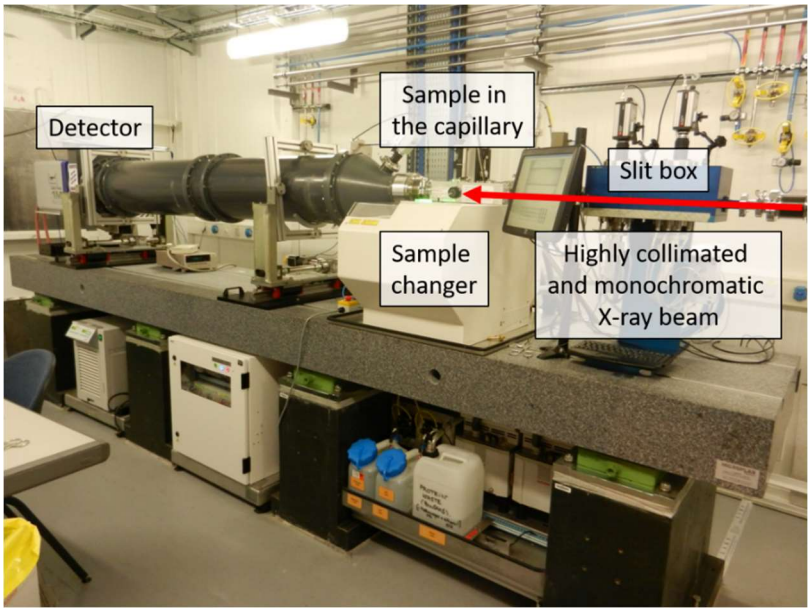

Figure 26: Photograph of the BM29 instrument at the ESRF including descriptions of its main parts. Photograph taken from the ESRF website [79].

The BM29 BioSAXS instrument features a fixed sample-to-detector distance of 2.867 m with a q-range of 0.0025 $Å^{-1}$ to 0.5 $Å^{-1}$. An automated sample changer was used to inject all samples into a 1.8 mm thick quartz glass capillary. Since samples can be prone to radiation damage from the high photon flux, the samples were put under constant flow through the capillary while measuring. As opposed to BM29, the ID02 instrument has movable detector with three sample-to-detector distances yielding a combined q-range of 0.0001 $Å^{-1}$ to 5 $Å^{-1}$. All sample positions were used in the measurements and merged into one curve after the data treatment procedures. The samples were injected manually and measured in a static set-up using a flow-through cell.

The Bruker Nanostar SAXS system features a InCoatec Cu microsource ($\lambda = 0.154$ nm), a Våntec-2000 detector and a scatter-less slits. The samples were injected manually into a temperature-controlled quartz cell located in a vacuum chamber and measured for 60 minutes.

There are several data treatment steps which are common for the instruments that must be performed on the raw detector images before the data can be used in analysis. First, the pixel data from the 2d-detector is normalized using the data collection time, incident beam intensity and the transmitted intensity, and unwanted pixels such as the beam stop, inter-modulus gaps and hot pixels are removed using a mask. These first calibration steps are usually performed using a homogenous scatterer such as glassy

carbon. Next, an azimuthal average is performed of the 2d-data to obtain 1d-data, assuming isotropic scattering. This is done by taking an average of all pixels at a radius $r_{det} = d_{det}\tan(\theta)$ with the center found from direct beam measurements. The q-values are calculated using the obtained values for the wavelength λ, the position of the beam and the sample-to-detector distance d_{det}. These steps yield the scattered intensity from the sample as a function of q.

To convert the data to an absolute scale, an internal standard with a known scattering cross-section $\frac{d\Sigma}{d\Omega_{st}}$ and thickness d_{st}. In this case, water at 20 °C was used as a standard. If also the scattering from the empty cell is measured both with and without the water standard, and by applying the same data reduction steps as described above, an absolute intensity can be calculated which is independent of the instrument used, and allows for the comparison of the scattering data with data from other times and instruments. The scattering cross-section of the sample is finally given as [80]

$$\frac{d\Sigma}{d\Omega_s}(\vec{q}) = \frac{\frac{d\Sigma}{d\Omega_{st}}(\vec{q})}{\left[\frac{I_{st}(\vec{q}) - BG_{st}}{d_{st}T_{st+cell}}\right]} \cdot \left[\frac{\mathrm{I_s}(\vec{q}) - BG_s}{d_s T_{s+cell}}\right] \tag{77}$$

where I_s and I_{st} is the measured intensity of the sample and standard, T_{s+cell} and $T_{st+cell}$ are the transmissions of the sample and standard in the cells, and BG are the scattering backgrounds.

Lastly, the captured frames from the detector are checked for radiation damage and the averages of the undamaged frames are calculated (only an issue for synchrotron SAXS data). The scattering from the solvent is then subtracted from the sample to yield the final scattering data which can be used for structure analysis.

3.2.2 SANS

The SANS measurements used for the investigations water transport through the vesicles membranes were performed at the very small-angle scattering instrument KWS-3 at the Forschungs-Neutronenquelle Heinz Maier-Leibnitz in Munich, Germany. The instrument is based on the focusing mirror principle and features two sample-to-detector distances yielding a total q-range of $4.0 \cdot 10^{-5}$ Å^{-1} to $2.0 \cdot 10^{-2}$ Å^{-1}. In the experiments presented in this work, only the sample-to-detector distance of 1.3 m was used, yielding a q-range of $1.5 \cdot 10^{-3}$ Å^{-1} to $2.0 \cdot 10^{-2}$ Å^{-1}

As in SAXS experiments, the raw data from the experiment cannot be used directly without data treatment. First, the effective detector area is determined by masking the beam top and any remnants of the direct beam. Next, a sensitivity matrix is used to correct the data and convert the data to absolute scale. This matrix is created by calibration from a well-known isotropic scatterer, in this case acrylic glass. Lastly, the empty cell and background subtraction is performed according to Equation 77, which holds for both SAXS and SANS. This was all automated using a script in the QtiKWS software [81].

To perform the water transport experiments, solutions of PBLG-PLL III were prepared in both H_2O and D_2O buffers at a concentration of 10. mg/mL. Right before the measurement, the H_2O solution

containing the copolypeptides were mixed with an equal amount of D_2O buffer and vice versa. The mixing was done in an Eppendorf tube using a micro pipette and then injected in the Hellma quartz capillary using a syringe. The time from mixing to the start of measurement averaged at approximately 1 minute.

3.2.3 Data analysis

Indirect Fourier Transform calculations on the small-angle scattering data were performed using the distance distribution tool in the PRIMUS software package [82] which is based on the GNOM program [83]. The system chosen in the software the calculation was «arbitrary monodisperse» using the full q-range if possible and around 200 splines. If the automatically chosen parameters failed to produce a good fit and/or produced unphysical oscillations around zero, the D_{max} parameter was varied manually until a satisfactory fit was obtained and/or the oscillations disappeared.

The fitting of scattering data to analytical models introduced in Section 2.4 was programmed using C++ in the QtiKWS software developed by Vitaly Pipich [81]. In most cases, the Nelder–Mead simplex algorithm was used to as a fitting algorithm, but the Levenberg-Marquardt algorithm was also used if the Nelder-Mead simplex algorithm was found to be inefficacious. Polydispersity in radius was calculated with a built-in option which uses Gaussian distribution, while polydispersity in length was programmed explicitly as described in Section 2.4.

3.2.4 Dynamic light scattering

Figure 27: Photograph of the Nanophox DLS instrument at the Department of Chemistry, University of Oslo, and the type of cuvette used for measurements.

The measurements were performed on a Sympatec Nanophox DLS instrument with photon cross-correlation spectroscopy (PCCS) located at the Department of Chemistry at the University of Oslo. A picture of the instrument and a sample cuvette can be seen in **Figure 27**. The instrument uses a laser with a wavelength of 632.8 nm with a single detection angle of 90°. The measurements were run for 240 s each at 37 °C after 30 minutes of temperature equilibration.

Multiple scattering and inter-particle interactions can cause unwanted contributions to DLS results. Although the PCCS should remove signals from multiple scattering, a dilution series was measured to ensure that this was achieved for reliable results. Measurements are also sensitive to large particles like dust, and the sample must therefore be as dust free as possible. This was attempted by filtering the sample solutions through a 5 µm filter (Millex-SV 25mm PVDF membrane from Merck Millipore) before adding them to an acrylic cuvette used in the measuring. The filtering and sealing of the cuvette was done inside a pressurized nitrogen atmosphere glove box.

The data was first analyzed by fitting the stretched exponential function in Equation 46 to the obtained cross-correlation functions, yielding the relaxation time τ and stretching parameter β. From this, the diffusion coefficient D was calculated using Equation 47, which was further used to calculate the hydration radius with the Stokes-Einstein relation (Equation 39) using the viscosity of water at 37 $°C$ (0.6913 mPas [84]). These analyses were performed in the Origin software package [85].

The cross-correlation functions were also fitted using the NNLS method using the Windox application by Sympatec, Germany [86]. It was performed in manual mode with a minimum particle size of 1 nm and a maximum particle size of 4000 nm. Lag times were adjusted manually until satisfactory fits were obtained.

3.2.5 Transmission electron microscopy

Imaging in real space of the diblock copolypeptide samples was done on a Philips FEI CM120 BioTwin transmission electron microscope located at the Institute of Oral Biology, University of Oslo. It was equipped with a tungsten filament and a Morada 11 megapixel CCD camera. The focal length was 6.15 mm, resolution ~3.4 Å (point to point) and the magnification could be varied from 18x to 330 000x. All images were shot in bright field mode with a beam voltage of 100 kV.

Figure 28: Photograph of the Philips FEI CM120 BioTwin transmission electron microscope located at the Institute of Oral Biology, University of Oslo.

3.2.6 Densitometry

In order to calculate precise scattering length densities and volume fractions for the analysis of the small-angle scattering data, the density of the solvents used in the experiments were measured at 37 °C using a U-tube Anton Paar D5000 density meter. This type of density meter contains a tube filled with the sample which is brought to oscillation by an electromagnet. Since the volume of the filled tube is known precisely and the oscillations depends on the mass of the tube, the density can be determined with high accuracy. The theoretical accuracy of the instrument is specified to be $1 \cdot 10^{-5}\mathrm{g/cm^3}$ and the temperature control is specified to be accurate within ± 0.01°C.

The scattering length density can be calculated using the formula

$$\rho_0 = \mathrm{N_A r_e} \sum_{i=1}^{N} c_i Z_i \tag{78}$$

where Z_i and c_i are, respectively, the number of electrons and the molar concentration of solvent component i, r_e is the Thompson radius and N_A is Avogadro's number. By rewriting Equation 78 for a system with a total density d_{tot} and a known concentration of salt, one gets

$$\rho_0 = N_A r_e \left[(d_{tot} - M_{salt} c_{salt}) \cdot \frac{Z_{H2O}}{M_{H2O}} + Z_{salt} c_{salt} \right] \tag{79}$$

which was used to calculate the SLDs in Table 4.

Table 4: Measured densities and calculated scattering length densities for solvents used to dissolve SDS.

Solvent	**Density (37 ° C) [gcm^{-3}]**	**Scattering length density [10^{10} cm^{-2}]**
Milli-Q H_2O	0.99328	9.3565
0.100 M NaCl	0.99712	9.3851
0.250 M NaCl	1.00362	9.4351
0.400 M NaCl	1.0099	9.4832
0.500 M NaCl	1.01311	9.5056
0.550 M NaCl	1.0153	9.5253
0.600 M NaCl	1.0181	9.5449
0.650 M NaCl	1.0207	9.5657
0.750 M NaCl	1.0235	9.5847
0.850 M NaCl	1.0272	9.6115
1.00 M NaCl	1.0326	9.6513
0.0835 M $MgCl_2$	0.9997	9.4163
0.167 M $MgCl_2$	1.0026	9.4245
0.250 M $MgCl_2$	1.0125	9.5080
0.333 M $MgCl_2$	1.0183	9.5540
0.500 M $MgCl_2$	1.0310	9.6538
5 mM KCl	0.9936	9.3588
5 mM $CaCl_2$	0.9938	9.3607

4 Results and discussion

This chapter is divided into two main parts. The first section contains the structural characterization of sodium dodecyl sulfate micelles in aqueous solutions with different salts and varying ionic strengths to study the morphological transition from globules to cylinders. The second section contains an investigation of the effects of PLL block length, concentration, pH, temperature, salt and sonication on the structure of self-assembled PBLG-PLL particles using small-angle X-ray scattering and complementary techniques to assess its potential as a drug-delivery system. Included here is also the study of the water permeability of PBLG-PLL bilayer membranes.

4.1 Structural Characterization of SDS micelles: transition from globules to cylinders

A model-independent analysis of the SDS micelles in water and salt solutions using indirect Fourier transformations is first presented. The SDS micelles in pure water is then further characterized by fitting an analytical model to synchrotron small-angle X-ray scattering data obtained from the BM29 beamline at ESRF, Grenoble, France which provides a reference for later comparison with micelles in salt solutions. This is followed by the characterization of SDS micelles in the aqueous solutions with NaCl, $MgCl_2$, KCl and $CaCl_2$ using the same techniques.

4.1.1 Indirect Fourier transformations

In order to get an overview of the shapes and sizes of SDS micelles at different salt concentrations, indirect Fourier transformations were performed on scattering data obtained from the BM29 SAXS instrument. To later obtain physical structural parameters from the fitting of scattering data, it is important that the selected analytical model represents the morphology present at in the sample at a certain concentration. IFT data is thus valuable as it can be used to estimate when the morphology transitions from globular (ellipsoids) to cylindrical (rods and worm-like micelles). Data from SDS with KCl and $CaCl_2$ were not included in this section due to problems with phase separation and will be discussed later together with the analysis of the SAXS data in Section 4.1.5.

Since the IFT calculations used in this work do not account for structure factor contributions, the calculations were performed on scattering data from the lowest SDS concentration (6.3 mg/mL). In Figure 29, the scattering curves from SDS in 0 M (pure water), 0.400 M and 0.500 M NaCl can be seen in (a) together with the corresponding pair-distance distribution functions in (b) calculated from the fits of the coefficients of the Fourier transform. The curves in the figure were selected due to the possible globule-to-cylinder transition occurring in this concentration regime, and the remaining fits can be found in the Appendix Section 6.3. The fits in Figure 29 (a) show excellent overlap with the experimental scattering data apart from a slight deviation at low q-values for SDS in pure water (red points) due to contributions from the

structure factor and an undescribed increase in scattering at the lowest q-values. The values obtained from this fit (0 M) might thus deviate slightly from the physical values. This should nevertheless be a minor issue in the later analysis since the structure of SDS micelles in pure water is already well-known in literature and the effect was not seen in the presence of salt.

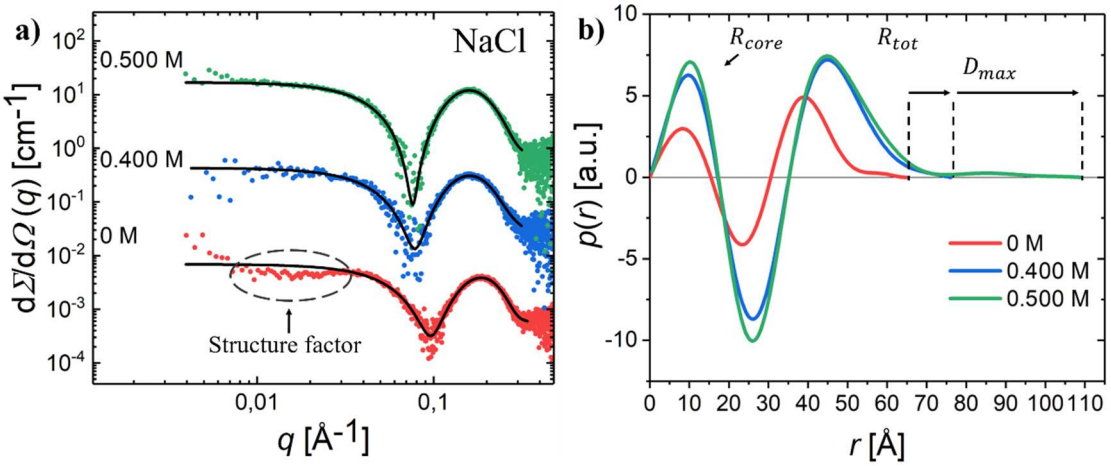

Figure 29: (a) Scattering curves from 6.3 mg/mL SDS in 0 M, 0.400 M and 0.500 M NaCl at 37 °C. The black lines represent the fits of the coefficients of the Fourier transform used to calculate $p(r)$. The curves are multiplied by 6^{2n} where n runs from 0 to 3 for clarity. **(b)** Pair-distance distribution functions calculated from the curves in **(a)**. Here, a substantial increase in the maximum distance D_{max} can be seen from 0.400 M to 0.500 M, indicating a transition from ellipsoids to rods.

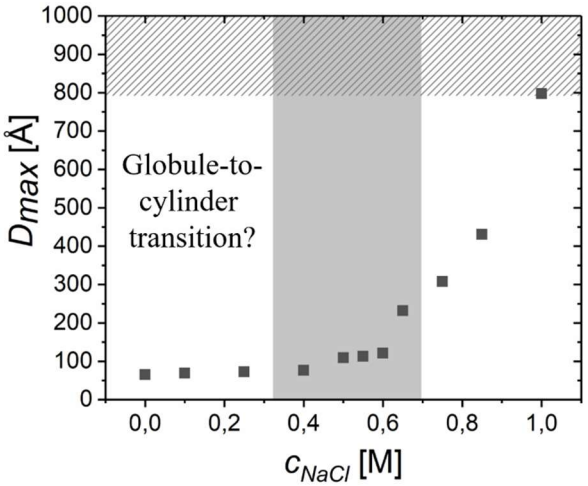

Figure 30: Plot of the maximum distance of the particles as a function of NaCl concentration. The hatched area marks unresolvable distances due to the limited q-range in the scattering data, and the grey area marks a possible concentration regime for the globule-to-cylinder transition.

Table 5: Maximum dimension D_{max} and radius of gyration R_G obtained from indirect Fourier transformations. SDS concentration is 6.3 mg/mL.

c_{NaCl} [M]	D_{max} [Å]	R_G [Å]
0	64.9	28.6
0.100	69.1	31.5
0.250	72.2	33.7
0.400	76.1	35.4
0.500	109	38.1
0.550	113	38.8
0.600	121	42.6
0.650	232	73.4
0.750	308	95.6
0.850	430	145
1.00	797	263

Qualitatively, the obtained $p(r)$ functions seen in Figure 29 (b) is similar to what is expected for core-shell micelles [87]. For ellipsoidal and cylindrical core-shell micelles, the maximum dimension (D_{max}) defines the major axis and the length of the micelles, respectively, and can be determined from the point where $p(r) = 0$ at high r-values. Moreover, an approximate value for the core radius (R_{core}) can be found from the first peak, and an approximate value for the total radius ($R_{tot} = R_{core} + dR$) can be found from the second peak. This can be seen illustrated in Figure 29 (b). It should be noted that this information is gathered differently compared to how information is derived from the small-angle scattering curves in (a). Here, the curves are described in reciprocal space and information such as the total radius and length is obtained at the beginning of the curve instead of at the end. The analysis of scattering data will be described in greater detail in the next sections where analytical models are fitted to the scattering curves. An interesting feature of the $p(r)$ functions in (b) is the presence of both positive and negative values similar to the example shown in the Theory Section 2.3.1. This is due to the opposite signs of the contrasts for the core and shell of the micelles. Although the obtained $p(r)$ functions from the micelles having ellipsoidal and cylindrical morphologies are expected to share this property and have similar shapes, they can still be distinguished by evaluating the asymmetry of $p(r)$ functions. As seen in the Theory Section 2.3.1, scattering from an elongated micelle such as a cylinder yields a more asymmetric $p(r)$ curve with a longer tail at high r-values. For SDS in pure water (red), the tail is short due to the slight elongation seen in micelles with an ellipsoidal morphology. For SDS with 0.500 M NaCl (green), however, the tail is more pronounced and grew considerably from the previous concentration. This indicates a morphological transition from ellipsoidal to cylindrical micelles.

Quantitative values for the radius of gyration R_G and maximum dimension of the particles D_{max} obtained from the transformations can be seen in Table 5, and these are plotted against concentration of NaCl in Figure 30. Here, a sharp increase in D_{max} from 0.400 M to 0.500 M can be seen, which again indicates a transition from globular to cylindrical micelles in this concentration region. The value continues to increase beyond this point, which is expected if there is a growth in the length of the cylindrical micelles as a function of salt concentration as described in Section 2.1.3. It is, however, difficult to pinpoint the exact transition region from these plots as slightly elongated ellipsoids and short cylinders produce similar scattering patterns and might also co-exist at certain concentrations. Due to this, a slightly wider region is drawn in grey in Figure 30 to illustrate where the transition likely occur. Interestingly, the obtained maximum dimension in the sample of 1.00 M NaCl reached the maximum resolvable distance r_{max} indicated by the hatched region in Figure 30 and signifies the presence of very long micelles. Access to scattering data containing lower q-values are therefore needed to fully characterize the length of the micelles at this concentration.

The same analysis was repeated for 6.3 mg/mL SDS in aqueous solutions with different concentrations of $MgCl_2$. In Figure 31 (a) and (b), the scattering curves from 0 M (pure water), 0.0835 M, 0.167 M and 0.250 M $MgCl_2$ are shown together with the corresponding pair-distance distribution functions calculated from the fits in (a). These concentrations were again selected to illustrate the possible globule-to-cylinder transition occurring in this regime, and the remaining fits can be found in the Appendix Section 6.3. All fits show excellent overlap with the experimental data apart from slight deviations at low q-values

for all curves due to an unexpected upturn which could not be fitted with this approach. The values obtained from the fits might therefore deviate slightly from the physical values as the first q-values were left out of the fit. This upturn will be discussed further together with the fits to the analytical models in Section 4.1.4.

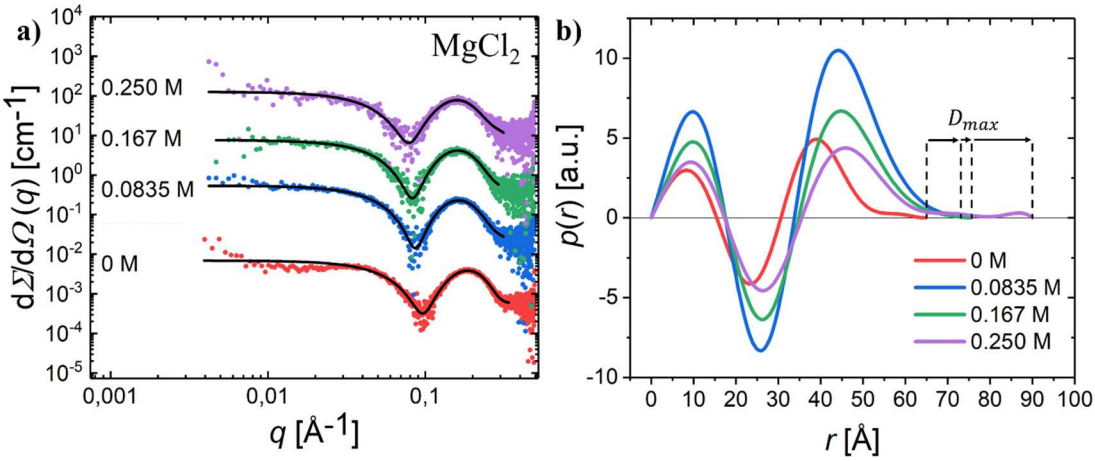

Figure 31: (a) Scattering curves from 6.3 mg/mL SDS in 0 M, 0.0835 M, 0.167 M and 0.250 M $MgCl_2$ at 37 °C. The black lines represent the fits of the coefficients of the Fourier transform used to calculate $p(r)$. The curves are multiplied by 5^{2n} where n runs from 0 to 3 for clarity. **(b)** Pair-distance distribution functions calculated from the curves in **(a)**. Here, a substantial increase in the maximum distance r can be seen from 0.167 M to 0.250 M, possibly indicating a transition from ellipsoids to rods.

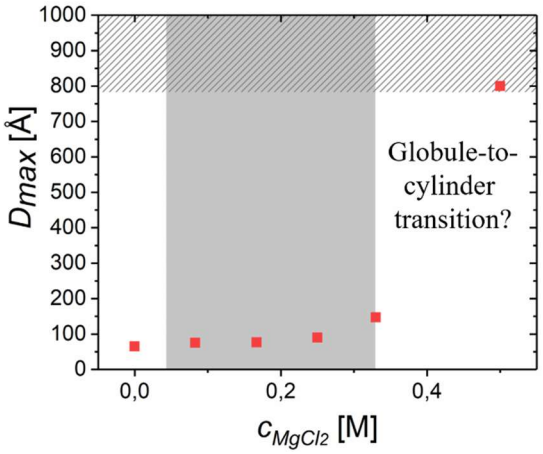

Figure 32: Plot of the maximum distance in the particles as a function of $MgCl_2$ concentration. The hatched area marks unresolvable distances due to the limited q-range in the scattering data, and the grey area marks a possible concentration regime for the globule-to-cylinder transition.

Table 6: Maximum dimension D_{max} and radius of gyration R_G obtained from indirect Fourier transformations. SDS concentration was 6.3 mg/mL.

c_{MgCl_2} [M]	D_{max} [Å]	R_G [Å]
0	64.8	28.9
0.0835	75.0	32.9
0.167	76.0	33.8
0.250	90.0	36.1
0.333	147	47.9
0.500	791	289

The values for the radius of gyration R_G and maximum dimension of the particles D_{max} obtained from the transformations can be seen in Table 6, and the maximum dimensions from the table are plotted against concentration of $MgCl_2$ in Figure 32. Here, a sharp increase in D_{max} from 0.167 M to 0.250 M can be seen, which indicate a transition from ellipsoidal to rod-like micelles in this concentration region. It is still difficult to pinpoint the exact concentration for the transitions, and a wider transition region is thus drawn in grey in Figure 32. In the same way as for SDS with NaCl, the value of D_{max} is increasing rapidly beyond

this point, and finally reaches the maximum resolvable distance at the highest $MgCl_2$ concentration which indicate the presence of very long and potentially flexible micelles.

To compare the growth behavior of SDS with NaCl compared to $MgCl_2$, the two data sets were plotted as a function of ionic strength in Figure 33. Ionic strength was used instead of concentration to account for the differences in ratio between the ions and the higher valence of the magnesium cation. While both exhibit a seemingly exponential growth behavior, the increase in D_{max} for SDS as a function of NaCl concentration happens at a higher rate than with $MgCl_2$. Since the curves from the two salts deviate from each other, the use of ionic strength does not seem to fully correct effect of $MgCl_2$, and other parameters such as the ionic radii might thus contribute to the growth behavior. The two curves were, however, found to coincide when a modification to the calculation of the ionic strength of $MgCl_2$ was applied. In the inset in Figure 33, the concentration of $MgCl_2$ was multiplied by a factor of 2 instead of the value of 3 which is used to calculate the correct ionic strength. It is nevertheless difficult to justify this modification theoretically as the detailed mechanisms of the elongation and the effects of ionic strength are not fully understood.

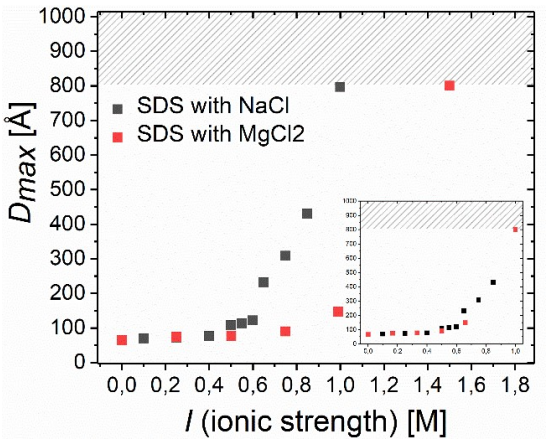

Figure 33: Plots of the maximum distance acquired from IFT in the particles as a function of ionic strength for solutions of 0.63 mg/mL SDS with NaCl (black) and $MgCl_2$ (red). The micelles with NaCl starts to elongate rapidly at a lower ionic strength than for micelles with $MgCl_2$. **Inset:** Same as the main plot, but the $MgCl_2$ concentration is multiplied by a factor of 2 instead of 3 as the curves was found to overlap with this modification to the ionic strength.

To summarize the results from indirect Fourier transformations, estimations of the concentration regions yielding transitions from globules to cylinders were found for both SDS with NaCl and $MgCl_2$. For NaCl, the transition appears to occur when increasing the NaCl concentration from 0.400 M to 0.500 M. The data from solutions with $MgCl_2$ were more difficult to analyze due to the fewer available concentrations and unexpected excess scattering at the lowest q-values. A possible transition was nevertheless found to occur from 0.167 M to 0.250 M. It is, however, difficult to pinpoint the exact concentration ranges for the transitions for both salts due to the similarity of the scattering patterns at these transitions and possible coexistence of the two morphologies. These concentrations ranges will therefore be confirmed by fitting analytical models to scattering data from small-angle scattering experiments in the following sections.

4.1.2 Fit of analytical model to scattering data from SDS in pure water

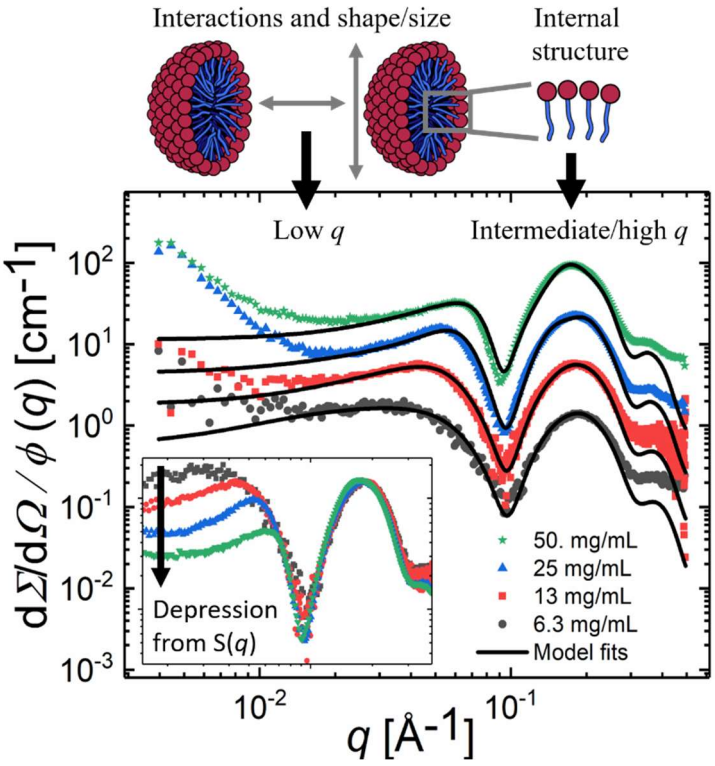

Figure 34: Points: Normalized scattering curves from a dilution series of SDS in pure water with illustrations of the corresponding real space length scales. **Lines:** Fits to the experimental points using the model of prolate ellipsoids and the Hayter Penfold structure factor. The curves are multiplied by 4^n where n runs from 0 to 3 for clarity. **Inset:** The same points and lines without scaling to illustrate the effect of the structure factor $S(q)$.

Normalized SAXS data from a dilution series of SDS in pure water at 37 °C can be seen in Figure 34. The SAXS curves displayed have the typical shapes for ellipsoidal core-shell surfactant micelles [12, 88]. At low q-values, corresponding to the size domain of a full micelle and larger, information about the particle size and shape in addition to the characteristics of the inter-particle interactions can be obtained. The inset in Figure 34 shows unscaled versions of the scattering curves to illustrate the depression in intensity at low q with increasing SDS concentration. This originates from the inter-micellar electrostatic repulsions and the associated structure factor. The contribution is weakest at the lowest SDS concentration, and the interference arising from the full shape of the ellipsoid is thus more dominating. The absence of a structure factor would give a flat curve as seen in the overview of form factors in Figure 17 in Section 2.2.1.

In addition to the depression, an increase in the scattering points at the lowest q-values can be observed. This was also seen when re-measuring freshly prepared samples at the in-house Bruker Nanostar SAXS instrument using the same concentrations and temperature. The curves scale as q^{-4}, which according to fractal scaling laws indicate the presence of large aggregates [49]. This was only observed for the micelles in pure water and was on the basis on the scaling law assumed to originate from aggregates of unknown origin.

At intermediate q-values and higher, scattering arising from the internal structure of the micelles can be seen. From this region, parameters such as the core radius R_{core} and head group thickness dR through model fitting can be obtained. There is in this part a distinct minimum arising from the negative contrast between the hydrocarbon chain and solvent. In a perfect, symmetric spherical micelle, this will cause zero scattering at a certain q-value, but small structure imperfections, polydispersity and resolution smearing will cause deviations from this. Hence, the more spherical the ellipsoid is (aspect ratio $\epsilon \rightarrow 1$), the deeper the minimum will become due to the increase in symmetry. This part of the scattering curve will therefore be important when later determining the aspect ratio ϵ from model fitting. A comparison between the normalized scattering curves of different SDS concentrations in the inset in Figure 34 shows an almost complete overlap at intermediate and higher q-values. This indicates only small variations in the structural parameters of the micelles as a function of SDS concentration which is expected due to the independence of the optimal aggregation number on concentration at these low volume fractions as explained in the Section 2.1.2.

To extract more detailed structural information, the scattering model for ellipsoidal core-shell micelles presented in Section 2.4.2 with a Hayter-Penfold structure factor was fitted to the data. This results in quantitative structural information which includes the core radius R_{core}, the head group thickness dR and aspect ratio ϵ. Additionally, parameters characterizing the structure factor by Hayter and Penfold explained in Section 2.5.1 are obtained. These are the hard-sphere radius R_{HS}, charge per micelle Z and the hard-sphere volume fraction η.

A potential problem when using the model-fit approach is that several models and combinations of parameters can yield equally good fits, especially when the number of fitted parameters is large. This is known as “over-parametrization”, and is important to consider when evaluating fitted scattering data. In the case of SDS micelles in pure water, however, the obtained fitting parameters are likely to be close to the actual parameters since the structure is relatively simple and literature values are available for reference.

For the fits, literature values for the specific volumes of the SDS molecule [89] and the C_{12} hydrocarbon chain [90] were used to calculate the scattering length densities of the core and shell. Moreover, an ionic dissociation of 73 % in pure water was assumed [89], and a polydispersity of 10 % was used for the core radius. The concentration of the stock solution is known from the sample preparation, and the CMC was set to the literature value of 8.1 mM in pure water [8]. Since the rest of the samples were made by dilution of the stock solution (25 to 6.3 mg/mL), these concentrations were initially set to a value half of the previous concentration while allowing for small variations in the fit due to possible inaccuracies while pipetting and deviations that arise from conversion of the scattering data to absolute units. It should be noted that the fitting model used concentration in units of $vol.\%$ as an input parameter.

Table 7: Parameters obtained by fitting scattering curves of SDS in pure water to an ellipsoidal core-shell micelle model. A full list of parameters used in the model can be found in the appendix. The errors are evaluated as described in the Appendix Section 6.2. Errors in the structure factor parameters are not given due to the unexpected increase in scattering at low q-values. * denotes fixed values.

c_{SDS}	Model	$vol.\%$	R_{core} [Å]	dR [Å]	ϵ	R_{HS} [Å]	Z	η
6.3 mg/mL	Ellipsoid	0.53(3)	13.7(5)	8.2(3)	1.38(5)	46.9	3.2*	0.007
13 mg/mL	Ellipsoid	1.04(3)	14.0(4)	8.2(3)	1.35(4)	37.0	3.2*	0.015
25 mg/mL	Ellipsoid	2.03(5)	14.2(4)	8.3(2)	1.32(4)	45.0	3.2*	0.025
50. mg/mL	Ellipsoid	4.00(9)	14.5(4)	8.5(2)	1.34(4)	36.8	3.2	0.026

Good fits were obtained at the intermediate q-range allowing giving an accurate determination of the core radius, head group thickness and aspect ratio. At the low and high q-range, however, the fits deviated substantially. The model was only fitted to the experimental data points prior to the upturn at low q to avoid contributions from the mentioned aggregates which could be expected to dominate the scattering here. While the micelle scattering should dominate at higher q-values, the obtained fit parameters should be analyzed with this in mind. The deviations at high q-values, however, can be attributed to the fact that the local structure at these short length scales are not fully incorporated in the model. While this could be accounted for by adding atomic form factor to the model, it would not yield any relevant information to this work and was thus left out.

The most relevant parameters obtained from the fits can be seen in Table 7. A full list of parameters can be found in the Section 6.5 in the appendix. For the core radius, values ranging from 13.7(5) Å to 14.5(4) Å were obtained. These lengths are less than the length of a fully stretched C_{12}-tail (16.6 Å [6]) and correspond well with values around 14 Å previously obtained in literature [12]. Furthermore, a head group thickness around 8 Å and an aspect ratio around 1.35 were obtained. It should be mentioned that an aspect ratio corresponding to oblate micelles ($\epsilon < 1$) could in some cases fit the data, but these two spheroids cannot be easily distinguished using static scattering methods [91]. Computer simulations using methods such as molecular dynamics are needed to conclude here. Since the micelles are expected to elongate and form rod-like structures in saline solutions, the prolate micelles were assumed to be the most reasonable. Regardless, both prolate and oblate micelles are likely to be present in the solution due to random fluctuations of the micelles [92]. Due to the unexpected increase in scattering intensity in the low q-range, the fit parameters that describe the structure factor was assumed to be inaccurate. The hard-sphere radii and hard-sphere volume fractions for the lowest to highest SDS concentrations were found to be 46.9 Å, 37 Å, 45 Å and 36.7 Å, and 0.007, 0.015, 0.025 and 0.026, respectively. The apparent charge per micelle of 3.2 was found to fit well for all concentrations and was fixed at this value to reduce the number of fit parameters. Despite the undescribed excess scattering at low q, the magnitude of the fit parameters fit well with the structure factor parameters obtained in a study of SDS in pure water with similar concentrations [12]. The increase in the hard-sphere radius for 25 mg/mL SDS and low value of the hard-sphere volume fraction for 50. mg/mL was, however, not expected, and can likely be attributed to the mentioned excess scattering at low q-values.

To summarize, fits of the model of prolate ellipsoids to the scattering curves from reference samples of SDS in pure water at concentrations ranging from 6.3 mg/mL to 50. mg/mL yielded optimized structural parameters which were in accordance to values in literature. Evidence of strong inter-particle interactions were also observed as depressions in the scattering curves at low q-values. Parameters describing the resulting structure factor were obtained, but due to possible aggregates or impurities in the samples, the values were assumed to be unreliable.

4.1.3 Fits of analytical models to scattering data from SDS in aqueous NaCl solutions

The obtained structural parameters of SDS micelles in pure water obtained as described in the previous section were used as a basis for fitting and analysis of the remaining synchrotron SAXS data from SDS in different salt solutions. It should be noted that certain samples with the highest concentrations of SDS and salt could not be measured using the automated sample changer at the BM29 SAXS instrument due to the high viscosity of the solutions. These were for this reason measured using the Bruker Nanostar SAXS instrument located at the University of Oslo (curves marked by *). Data was acquired from the same four concentrations of SDS as for the reference measurements (6.3 mg/mL, 13 mg/mL, 25 mg/mL and 50. mg/mL) in aqueous solutions with NaCl in concentrations ranging from 0 M to 1.00 M. This allowed us to capture the transition from globular to cylindrical micelles in detail for use in the construction of phase diagrams in Section 4.1.7 and evaluation of the effects of ionic strength. Different models were henceforth used for the model fits at different concentrations depending on the morphology indicated by indirect Fourier transformations (Section 4.1.1), qualitative analysis, fit quality and literature.

The normalized scattering data and corresponding fits for all concentrations of both SDS and NaCl studied in this work is shown in Figure 35 (a-d). At low salt concentrations and low q-values, the curves exhibit plateau-like scattering which indicates the presence of globular or short rod-like micelles of limited size. When the salt concentration is increased further, however, there is a significant upturn indicating elongation of the micelles [93]. This effect is highlighted in Figure 36 where the scattering curves from 13 mg/mL SDS in solutions of 0.100 M, 0.600 M and 1.00 M NaCl can be seen. The dotted line represents the theoretical low-q scattering from a self-avoiding worm-like micelle with finite flexibility and scales as $q^{-1.7}$ [93]. Clearly, the experimental data falls below this line and shows no signs of being worm-like. This behavior was seen for all concentrations of SDS and NaCl. To find the actual slope of the curve from 1.00 M, a linear fit was applied and the curve was found to scale as $q^{-1.1}$. This is close to the q^{-1} behavior expected for cylindrical micelles [93]. The small deviation from the theoretical value is likely due to the sensitivity of the slope to the background subtraction process.

At intermediate q-values, the minima are shifted leftwards with increasing concentration of NaCl while preserving the overlap of the curves at high q-values. This is due to the change in contrast from the increase in the salt concentration, in addition to the change of morphology from ellipsoids to cylindrical micelles.

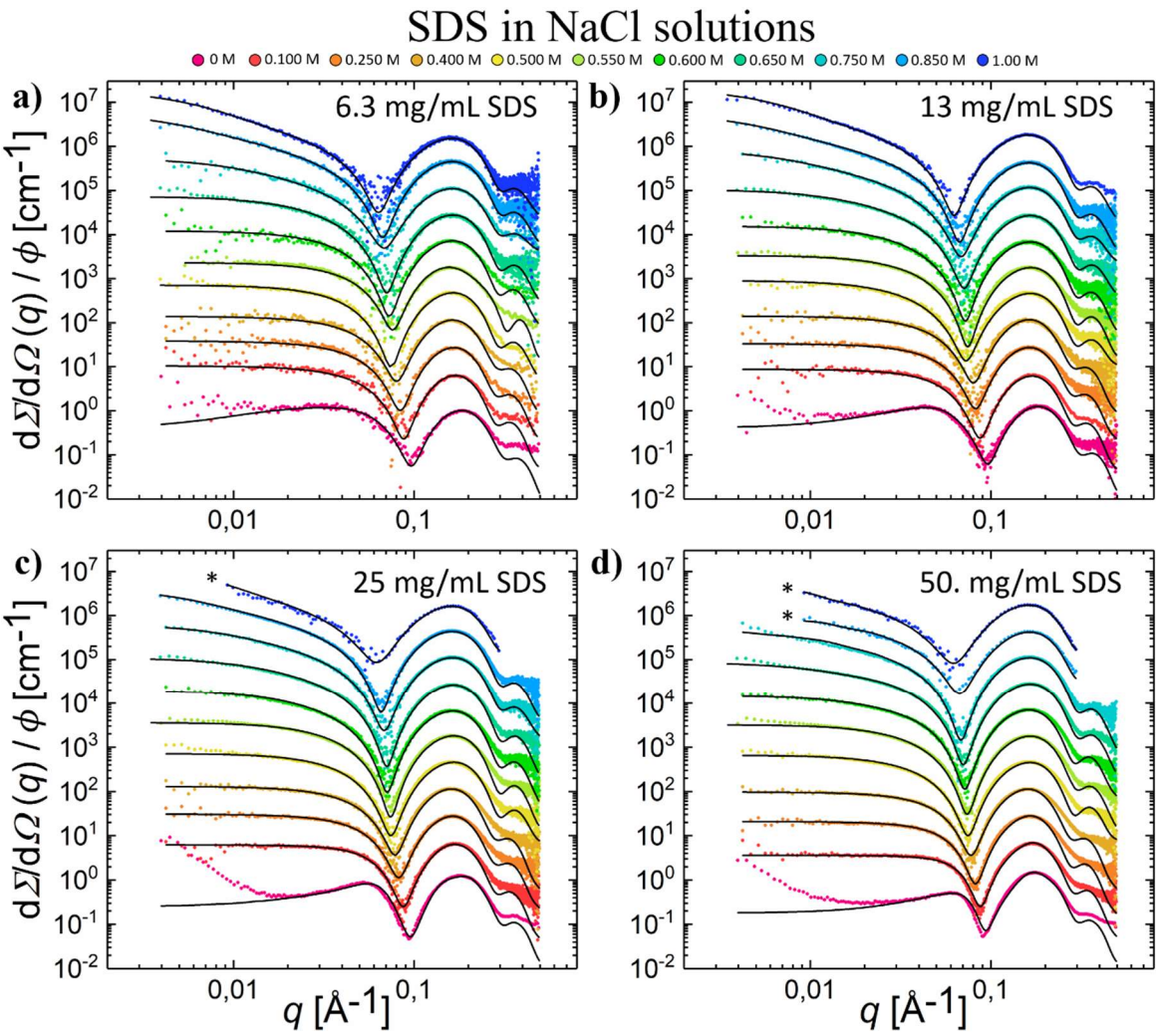

Figure 35: Points: Normalized SAXS data of **(a)** 6.3 mg/mL SDS, **(b)** 13 mg/mL SDS, **(c)** 25 mg/mL SDS and **(d)** 50. mg/mL SDS in aqueous solutions of NaCl at concentrations ranging from 0 M to 1.00 M at 37 °C. **Lines:** Model fits using core-shell models of prolate ellipsoids, short rods and long rods. All curves are multiplied by 4^n where n runs from 0 to 10 for clarity. * measured using the Bruker Nanostar SAXS.

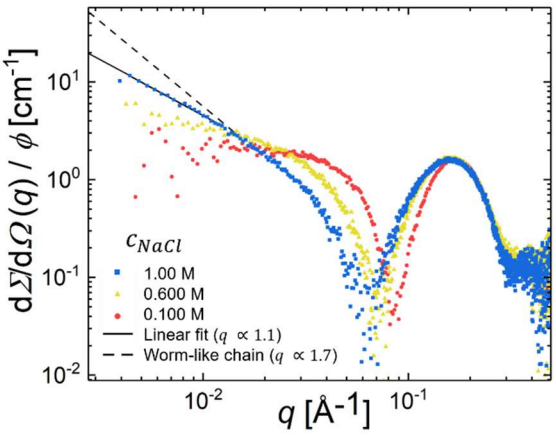

Figure 36: Points: Scattering curves from 13 mg/mL SDS at selected NaCl concentrations illustrating the increasing slope at low q-values due to elongation of the micelles. **Line:** Linear fit to the scattering curve from 1.00 M NaCl with a slope of 1.1. **Dotted line:** Theoretical scattering behavior for a self-avoiding worm-like micelle with finite chain flexibility. The scattering curves falls below this line which indicates non-flexible micelles.

The detailed results obtained from the fits of the scattering data in Figure 35 are summarized in Table 8. Due to the complexity and size of the data set, only results from 13 mg/mL SDS are included in this section. Data from this concentration was chosen as it features both good data quality and contains minor contributions from the structure factor. The remaining data can be found in the appendix Section 6.5 and is also presented graphically and discussed later in Section 4.1.6 and 4.1.7. Once again, certain parameters were set to literature values or chosen carefully. The concentrations were initially set to the concentrations expected from the dilution of the stock solution while allowing for small variations when fitting. The CMC was for all salt concentrations neglected as it is found to be very small in saline solutions [9]. The surfactant density was fixed at the literature value of 1.162 g/cm^3 for SDS in pure water and then fitted for the rest of the data set to account for the change in surfactant head group density and/or solvation layer introduced by the salt. This could be done relatively accurately since this value influences the position of the minima in the scattering curves. For the core radius of the cylindrical micelles, a polydispersity of 0.15 was used as lower values were found to produce poor fits. It is likely that an increase in the polydispersity compared to the fits of SDS in pure water in Section 4.1.2 was needed because a strictly circular cross-section was used in the analytical model. It has been argued in literature that the actual cross-section of such micelles is ellipsoidal, but it is difficult to distinguish this from a poly-disperse circular cross-section [94].

Table 8: Fit parameters from 13 mg/mL SDS in aqueous NaCl solutions. The errors are evaluated as described in the appendix Section 6.2. * denotes fixed parameters

c_{NaCl}	Model	$vol.\%$	R_{core} [Å]	dR [Å]	ϵ	L_{mean} [Å]	b [Å]	$S(Q)$?
0 M	Ellipsoid	1.04(3)	14.0(4)	8.2(3)	1.35(5)	N/A	N/A	Yes
0.100 M	Ellipsoid	0.95(3)	15.1(5)	9.0(4)	1.32(9)	N/A	N/A	Yes
0.250 M	Ellipsoid	1.15(4)	15.5(3)	8.8(6)	1.34(6)	N/A	N/A	Yes
0.400 M	Ellipsoid	1.12(4)	15.3(5)	8.8(4)	1.37(9)	N/A	N/A	No
0.500 M	Short rod	1.32(3)	13.1(5)	9.4(3)	N/A	68(7)	N/A	No
0.550 M	Short rod	0.88(4)	13.1(4)	9.4(2)*	N/A	61(6)	N/A	No
0.600 M	Short rod	1.15(3)	13.0(4)	9.4(3)*	N/A	79(8)	N/A	No
0.650 M	Long rod	1.18(3)	12.8(5)	9.4(2)*	N/A	138(12)	$> L_{mean}$	No
0.750 M	Long rod	1.20(4)	12.8(6)	9.4(4)*	N/A	276(25)	$> L_{mean}$	No
0.850 M	Long rod	1.08(3)	12.8(4)	9.4(2)*	N/A	526(40)	$> L_{mean}$	No
1.00 M	Long rod	0.98(5)	12.8(4)	9.4(3)*	N/A	628(42)	$> L_{mean}$	No

At low salt concentrations, the micelles are expected to be ellipsoidal [11, 12]. Moreover, since only cylindrical micelles are expected to grow rapidly in length as a function of salt concentration, the globular morphology was also indicated by the almost constant value of the maximum dimension D_{max} at NaCl concentrations up to 0.400 M acquired by IFT. For that reason, the data in this concentration range (0.100 M to 0.400 M) was analyzed using the model of core-shell ellipsoids, producing fits which exhibit excellent overlap with the experimental data. It should be mentioned that the model of short rod-like micelles could

to some extent also fit the data at these concentrations, but in addition to the above arguments, the quality of the fits was poorer compared to the fits using the model of prolate ellipsoids.

From 0.500 M to 1.00 M NaCl, the models of short or long rod-like micelles was fitted to the experimental data depending on the estimated lengths of the micelles. Apart from a few deviations at low q-values, the fits overlap well with the experimental curves. No signs of repulsion were found in the scattering patterns for an SDS concentration of 13 mg/mL as the normalized scattering curves overlapped at low q-values with the curves from 6.3 mg/mL SDS. The structure factor was thus left out of the model. At higher SDS concentrations, however, minor depressions of the scattering curves were observed at low q-values. In these cases, a modified version of the PRISM structure factor introduced in Section 2.5.2 was applied. A wider concentration range of SDS than what was available was needed to calculate precise values for β and $c(q)$ in the PRISM structure factor, and these were therefore combined in a new fit parameter B.

The transition into rod-like micelles introduced a significant change in the core radius from above 15 Å for the ellipsoids down to values around 13 Å. This happens mainly by geometrical reasons as the tails are located in a cylindrical structure instead of an ellipsoidal. The head group thickness was found to be $dR = 9.4$ Å for the lowest concentration and was fixed at this value for the remaining fits to reduce the number of fit parameters. This is slightly higher than for the lower concentrations and might be attributed to changes in the solvation layer and counter-ion binding at the micelle/water interface. Resolving the exact mechanisms behind this is beyond the scope of SAXS, and computer simulation are needed to draw conclusions. In contrast to the lower NaCl concentrations, the micelles now increase drastically in size as a function of salt concentration with lengths varying from around 70 Å to above 600 Å at 1.00 M NaCl. Just as in Figure 36, no signs of flexibility were found since Kuhn lengths larger than the mean length were required to produce good fits at low q-values. Thus, the value was fixed at an arbitrary value of $b > L_{mean}$. A significant increase in the aspect ratio ϵ of the ellipsoids with increasing salt concentration has previously been found in literature [12], but this was not seen in this work. This was surprising as the ellipsoids were thought to elongate before transitioning into rod-like micelles. However, since the shape of the minimum in the scattering patterns is very sensitive to the background subtraction process, the information contained in the minimum which describes the elongation might have been lost. It should also be considered that the temperature in reference [12] was different (25 °C), and that the increase in the aspect ratio might not occur at the conditions used in this work.

4.1.4 Fits of analytical models to scattering data from SDS in aqueous $MgCl_2$ solutions

Before the effect of ionic strength and different salts on the structures and morphology of the micelles could be studied and used to construct phase diagrams, SDS micelles in aqueous solutions with $MgCl_2$ were characterized by model fitting to synchrotron SAXS data. The data was measured at concentrations of $MgCl_2$ chosen to be comparable to selected concentrations of NaCl both in terms of ionic strength and molar concentration as seen in Table 9.

Table 9: Overview over the concentrations and ionic strengths of the NaCl and $MgCl_2$ solutions used in this work. The concentrations of $MgCl_2$ was chosen to be comparable to certain concentrations of NaCl both in terms of molar concentration and ionic strength.

c_{NaCl}	I_{NaCl}
0.100 M	0.100 M
0.250 M	0.250 M
0.400 M	0.400 M
0.500 M	0.500 M
0.550 M	0.550 M
0.600 M	0.600 M
0.650 M	0.650 M
0.750 M	0.750 M
0.850 M	0.850 M
1.00 M	1.00 M

c_{MgCl_2}	I_{MgCl_2}
0.0835 M	0.250 M
0.167 M	0.500 M
0.250 M	0.750 M
0.333 M	1.00 M
0.500 M	1.50 M

Normalized scattering curves and model fits for all concentrations of SDS and $MgCl_2$ can be seen in Figure 37. For the concentrations up to 0.250 M $MgCl_2$, the same plateau-like behavior as with NaCl is observed, which indicate ellipsoidal or short rod-like micelles of resolvable size. At higher concentrations, there is again an upturn indicating elongated structures. Figure 38 shows the scattering behavior of 13 mg/mL SDS for the highest $MgCl_2$ concentrations compared to the lowest, and also a dotted line showing the theoretical scattering of a flexible self-avoiding chain. The scattering curve from 0.500 M $MgCl_2$ follows the characteristic scattering from a flexible self-avoiding chain at higher q-values which indicates the presence of worm-like micelles. At the lowest q-values it has a slope following $q^{-2.6}$. This part of the curve is clearly falling above the line with a slope of $q^{-1.7}$, but also below the line showing the theoretical scattering of large aggregates. With the assumption that this is not caused by instrumental artefacts or impurities, it is likely caused by the formation of cross-links or branches between or in the worm-like micelles. This hypothesis is supported by the viscous and almost gel-like behavior of the solutions with the highest salt concentrations that was observed when performing the experiments. In scattering curves, this is known to give steeper slopes at low q-values due to the change in the fractal dimension [95], which indeed fits with the experimental data. Since the slope is very sensitive to the background subtraction process, the intensity of the background was manually shifted before the subtraction to get an estimation of the error in the slope arising from this process. The error was not, however, found to be high enough to account for the steeper slope, which further supports the hypothesis.

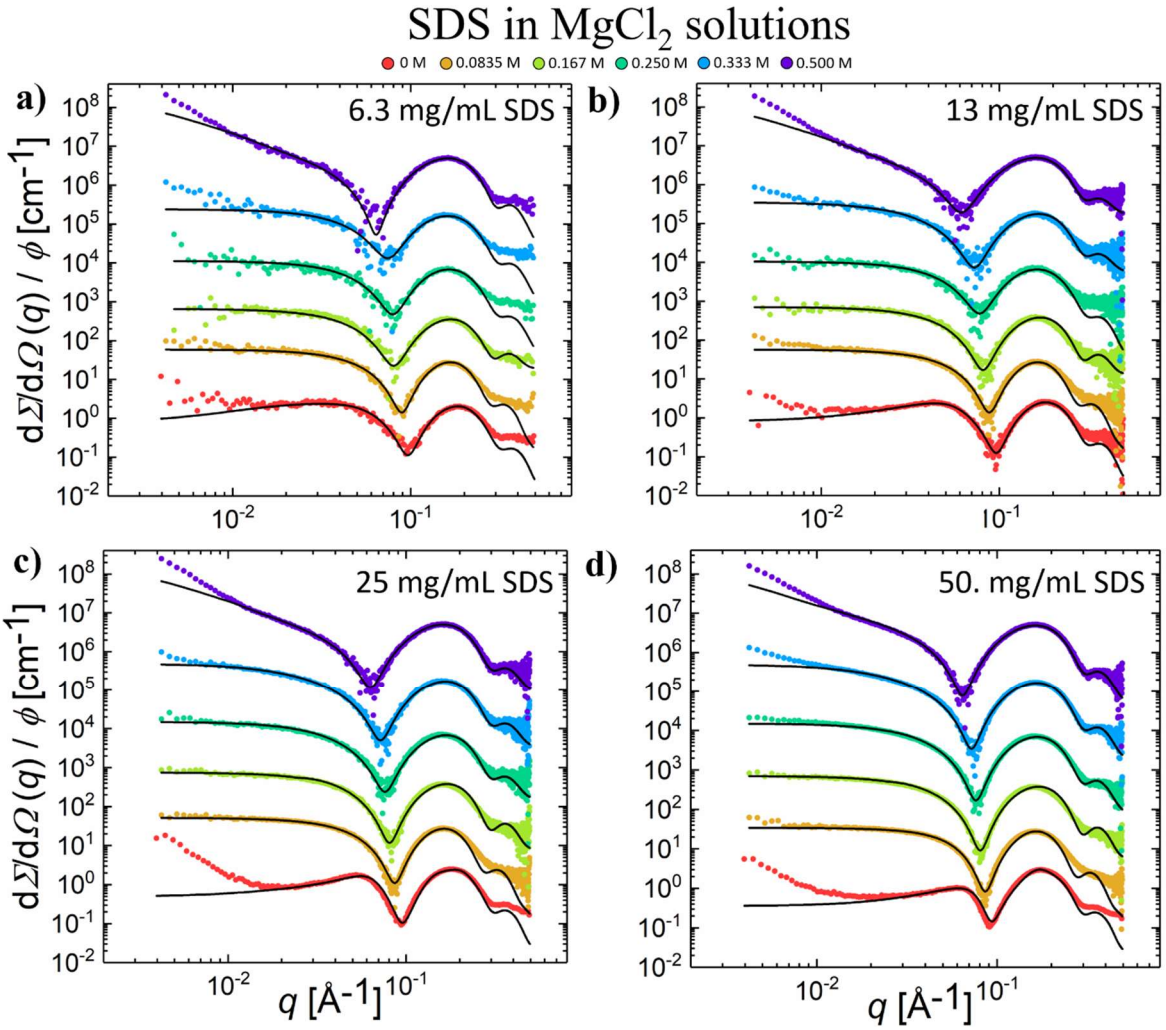

Figure 37: Points: Normalized SAXS data of **(a)** 6.3 mg/mL SDS, **(b)** 13 mg/mL SDS, **(c)** 25 mg/mL SDS and **(d)** 50. mg/mL SDS in aqueous solutions with $MgCl_2$ at concentrations ranging from 0 M to 0.500 M at 37 °C. **Lines:** Model fits using core-shell models of prolate ellipsoids, short rods and long rods/worms. All curves are multiplied by $(2n)^n$ where n runs from 1 to 6 for clarity.

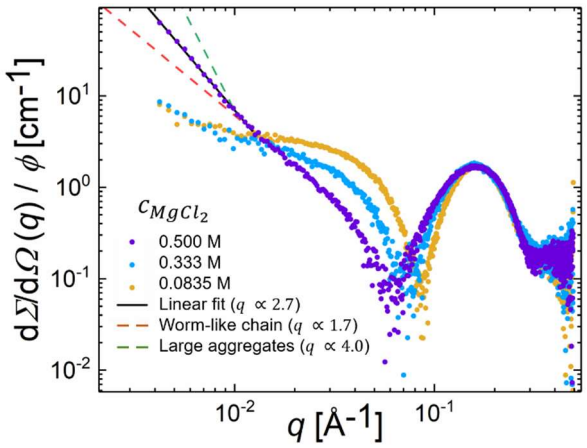

Figure 38: Points: Scattering curves for 13 mg/mL SDS at selected $MgCl_2$ concentrations showing the increasing slope at low q-values. **Lines:** Theoretical scattering behavior for a self-avoiding worm-like micelle with finite chain flexibility ($\propto q^{-1.7}$) and for large aggregates ($\propto q^{-4}$), and linear fit to the scattering curve of 0.500 M. Note that the curve first follows the behavior of a self-avoiding chain, but then falls above it at lower q-values. This might be attributed to cross-linking or branching of the micelles.

The fit parameters obtained from the fits of 13 mg/mL SDS in Figure 37 are summarized in Table 10. The remaining data can be found in the Appendix Section 6.5 and is also discussed in Section 4.1.6 and 4.1.7. The same fitting procedures and fixed parameters that were applied for SDS with NaCl were also used here. All fits explain the experimental curves well at most q-values. There are, however, some deviations from the scattering curves at low q-values for certain concentrations. These points could not be fitted using any of the models, and was expected to be artefacts from the SAXS instrument or background subtraction. It can also be due to cross-linking and/or branching, but this was thought to be unlikely at the lower concentrations.

The model of prolate ellipsoids were used to fit the data at 0.0835 M $MgCl_2$ as this morphology was expected at low salt concentrations and indicated by IFT in Section 4.1.1. Even though the calculations presented in this section indicated ellipsoids also at 0.167 M, if was not possible to obtain equally good fits to these scattering curves using the model of prolate ellipsoids. The model of short-rod like micelles was therefore employed from 0.167 M to 0.333 M. The model of prolate ellipsoids was also tested for higher concentrations, but the model was not found to fit equally well. Lastly, the model of long worm-like micelles was used to analyze the data at 0.500 M as the slope at low q-values indicated flexible structures. At these concentrations of SDS, the structure factor was left out as no signs of repulsion in the scattering curves were observed. This was again determined by plotting the normalized scattering curves for each concentration of salt and checking for depressions of the scattering curves at high concentrations of SDS. As for NaCl, a modified version of the PRISM structure factor was employed if signs of repulsion were observed.

The radius was again found to drop after the transition into cylindrical micelles, and the same head group thickness of 9.4 Å was used as this value is not expected to vary and was found to fit for all curves. No substantial changes in the aspect ratio ϵ was observed.

Table 10: Fit parameters from 13 mg/mL SDS in aqueous $MgCl_2$ solutions. The errors are evaluated as described in the appendix **Section 6.2**.

c_{MgCl_2}	Model	$vol.\%$	R_{core} [Å]	dR [Å]	ϵ	L_{mean} [Å]	b [Å]	$S(Q)$?
0 M	Ellipsoid	1.04(3)	14.0(4)	8.2(3)	1.35(4)	N/A	N/A	Yes
0.0835 M	Ellipsoid	1.22(3)	15.5(5)	9.4(4)	1.34(5)	N/A	N/A	No
0.167 M	Short rod	0.95(4)	13.3(4)	9.4(4)	N/A	44(5)	N/A	No
0.250 M	Short rod	1.10(3)	12.8(3)	9.4(3)	N/A	36(5)	N/A	No
0.333 M	Short rod	0.95(4)	12.8(3)	9.4(4)	N/A	75(7)	N/A	No
0.500 M	Worm	1.40(4)	12.8(3)	9.4(4)	N/A	1000	270	No

4.1.5 Fits of analytical models to scattering data from SDS in aqueous KCl and $CaCl_2$ solutions

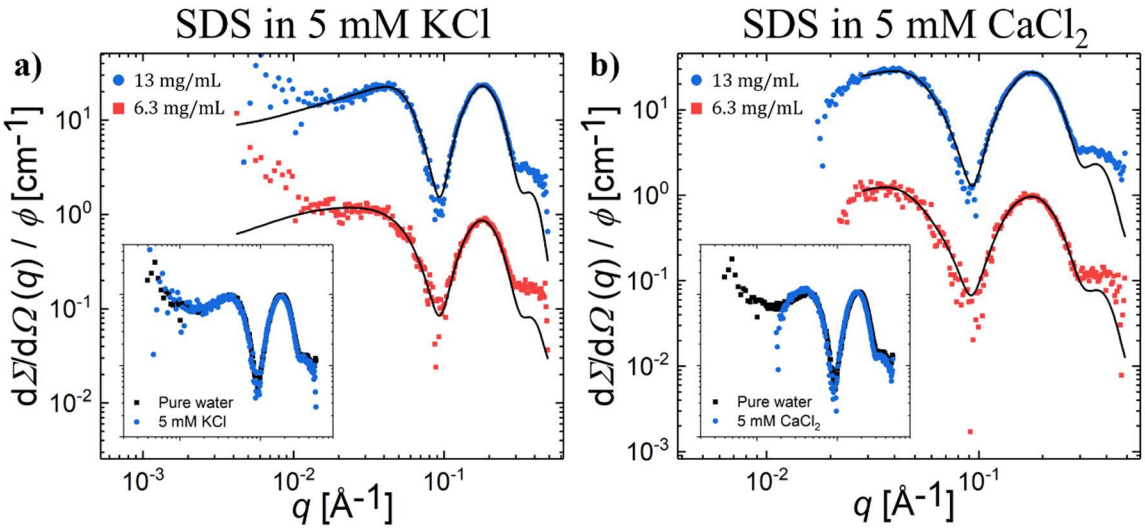

Figure 39: Points: Normalized SAXS data of **(a)** SDS in aqueous solutions of 5 mM KCl ($I = 5$ mM)) **(b)** SDS in aqueous solutions of 5 mM $CaCl_2$ (I = 15 mM) **Lines:** Model fits using core-shell models of prolate ellipsoids. The uppermost points and curves are multiplied by a factor 25 for clarity. **Insets:** Comparison of 13 mg/mL SDS in 5 mM KCl and 5 mM $CaCl_2$ (blue circles) to 13 mg/mL SDS in pure water (black squares).

To further investigate the effect of other cations on the micellar morphology, an attempt was made to dissolve SDS in solutions of KCl and $CaCl_2$ using similar concentrations as for NaCl and $MgCl_2$. Contrary to the solutions with other salts described in the two previous sections, these were all found to phase separate at 37 °C, and could therefore not be used in scattering experiments in the same concentrations ranges. To produce solutions that could be used for experiments, the concentration of SDS was brought down to 13 mg/mL and 6.3 mg/mL, and the concentration of KCl and $CaCl_2$ to 5 mM. Solutions of higher concentrations was found to phase separate.

In Figure 39, the normalized scattering data and corresponding fits for 13 mg/mL and 6.3 mg/mL SDS in 5 mM KCl ($I = 5$ mM) (a) and 5 mM $CaCl_2$ ($I = 15$ mM) (b) are shown. For KCl, the scattering curves look similar to the curves obtained from SDS in pure water. For $CaCl_2$, however, the scattering points at low q-values are missing due to problems in the background subtraction that was likely caused by the presence of Ca^{2+} which is known to cause difficulties with radiation damage. The parameters obtained from the fits might therefore be unreliable. The insets in Figure 39 show the normalized scattering curves from 13 mg/mL SDS in 5 mM KCl and 5 mM CaCl2 compared to the reference sample of 13 mg/mL SDS in pure water (black squares). The scattering curves from both salts overlap completely with the reference curves apart from in the low q-region for SDS in $CaCl_2$, and the structures does not seem to be impacted by these low ionic strengths.

The fitting was performed using the fits for SDS in pure water as a reference, and the obtained parameters were expected to be close to these due to the almost negligible salt concentration and the overlapping curves shown in the insets in Figure 39. An overview of the obtained fit parameters can be seen

in Table 11. The resulting parameters fit well with the experimental curves apart from for the low q-values for $CaCl_2$ due to the mentioned subtraction problems.

For the KCl solutions, core radii values R_{core} of 13.6(4) Å and 13.5(4) Å were obtained, which is indeed very similar to the values from the same concentrations in the pure system of 13.7(5) Å and 14(4) Å. The head group thickness dR is also similar at around 8 Å. The aspect ratio ϵ was found to be slightly larger than for the pure system, but is likely due to the sensitivity of this parameter to the background subtraction process as explained for the case of SDS in pure water.

The fits to the $CaCl_2$ solutions yielded similar values as for the pure system, but will not be further discussed due to the unreliability of the data.

Table 11: Fit parameters from SDS in aqueous solutions of 5 mM KCl and 5 mM $CaCl_2$. The errors are evaluated as described in the Appendix Section 6.2.

c_{SDS}	c_{Salt}	Model	$vol.\%$	R_{core} [Å]	dR [Å]	ϵ	R_{HS} [Å]	Z	S_{SQ}
6.3 mg/mL	5 mM KCl	Ellipsoid	0.6(1)	13.6(4)	8.0(3)	1.50(6)	52.7	2.8	7.8
13 mg/mL	5 mM KCl	Ellipsoid	1.2(3)	13.5(4)	8.3(3)	1.45(5)	52	2.8	11.9
6.3 mg/mL	5 mM $CaCl_2$	Ellipsoid	0.5(1)	14.0(4)	8.2(3)	1.45(5)	66.5	2.8	24.3
13 mg/mL	5 mM $CaCl_2$	Ellipsoid	1.2(3)	14.2(4)	8.4(3)	1.35(5)	56.5	2.8	11

4.1.6 Effect of salt on contour lengths and radii in SDS micelles

The core radius R_{core} and mean contour length L_{mean} are the two most important structural parameters characterizing the micelles and were found to vary considerably with both concentration of salt and SDS. Optimized values for these parameters obtained from the fits to the scattering data presented in Section 4.1.2 to 4.1.4, and can be seen plotted as a function of salt concentration in Figure 40 (a) and (b).

In the ellipsoidal concentration regime for both NaCl and $MgCl_2$, the core radii approach values between 15 Å and 16 Å. This is close to the literature value of a fully stretched C_{12}-tail (16.6 Å [6]), and indicates a possible elongation of the hydrocarbon tails caused by the salts. After the morphological transition to rods/worms indicated by the black vertical line, the core radii for both systems decrease to almost constant values which are lower than the for the pure system. This can as, mentioned earlier, be explained by geometrical arguments. The effect of SDS concentration on the core radii can also be seen in the plot, but the variations are small and insignificant in all cases. This is expected as the size of globular micelles are virtually concentration independent as explained in Section 2.1.2.

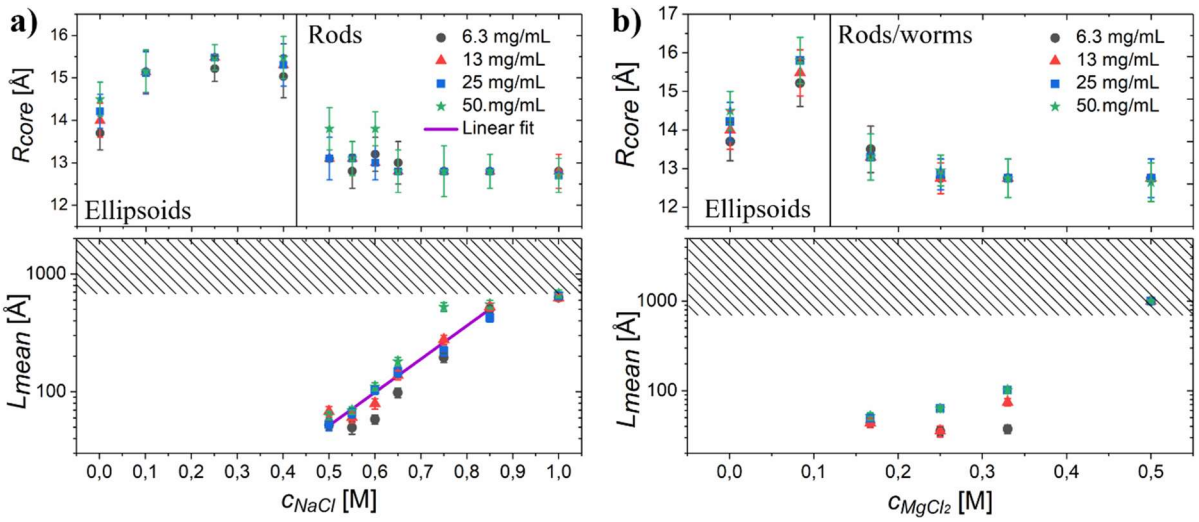

Figure 40: Plots of the core radii and mean contour lengths for the ellipsoids and rods/worms of SDS micelles in aqueous solutions of **(a)** NaCl and **(b)** $MgCl_2$. The hatched areas mark the lengths longer than the estimated maximum resolvable dimension obtained from the minimum q-value in the data set. The purple line was fitted to the data points from 13 mg/mL SDS in NaCl to illustrate the exponential increase in mean length (note the logarithmic vertical axis).

While the radii remain relatively constant as a function of salt concentration, the mean length of the cylindrical micelles was found to increase drastically. For the micelles with added NaCl, the data points followed a straight line in the semi-logarithmic plot indicating an exponential growth behavior as a function of salt concentration. To illustrate this, an exponential function was fitted to the data points from 13 mg/mL SDS, and this fit can be seen in Figure 40 (a) (purple line). This behavior is in agreement with what was observed in an extensive study by J. S. Pedersen et. al. of SDS micelles in aqueous solutions of NaBr at 40°C using small-angle neutron scattering [11]. Here, they presented an empirically derived growth law where the logarithm of the aggregation number was found to be proportional to the concentration of NaBr through the relation

$$B_1 = ae^{b[\mathrm{NaBr}]} \tag{80}$$

where B_1 is proportional to the aggregation number, and a and b are constants. Although this law is empirical, the following rationalization according to reference [11] can be made. The average aggregation number N_{ave} might be written as $N_{ave} \propto e^{\mu_{rod}/k_BT}$ for $c \gg c_{cmc}$ where μ_{rod} is the free energy of the end caps. Since B_1 is proportional to the aggregation number, one can write $B_1 \propto e^{\mu_{rod}/k_BT}$. The free energy of the end caps might be divided into several contributions, and of which the electrostatic contribution is affected by the salt concentration. It might thus be written as $\mu_{rod} = \mu_{el} + \mu_{othe}$, where μ_{other} includes other contributions than electrostatics. The contribution from electrostatics is known to be negative, and it will completely disappear at infinite concentrations of salt. This means that $\mu_{rod} \to \mu_{other}$ when [NaBr] $\to \infty$. According to Equation 80, $\mu_{rod} = \ln(a) + b[\mathrm{NaBr}]$, and for the limit of infinite salt concentration $\mu_{othe} = \lim_{[\mathrm{NaBr}]\to\infty} (\ln(a) + b[\mathrm{NaBr}])$. This means that μ_{othe}, and also the size of the micelles, will reach a maximum value for some large value of [NaBr] thereby implying growth of the micelles.

A drastic increase in the mean length was also observed for SDS in solutions of $MgCl_2$. While the growth of these micelles are also likely to exhibit a similar growth behavior, more data points between

0.333 M and 0.500 M $MgCl_2$ are needed conclude on the comparison of the growth in length of the two systems. There is furthermore some unreliability of the first data points in the scattering curves from SDS with $MgCl_2$ which are important when determining the length.

The effect of SDS concentration on the contour lengths is more pronounced compared to the effect on the radii. It is clear from the plots that the lengths increase significantly as a function of SDS concentration alone. This has been observed in similar studies [9, 11, 12, 96] and was also expected from theory as explained in Section 2.1.3.

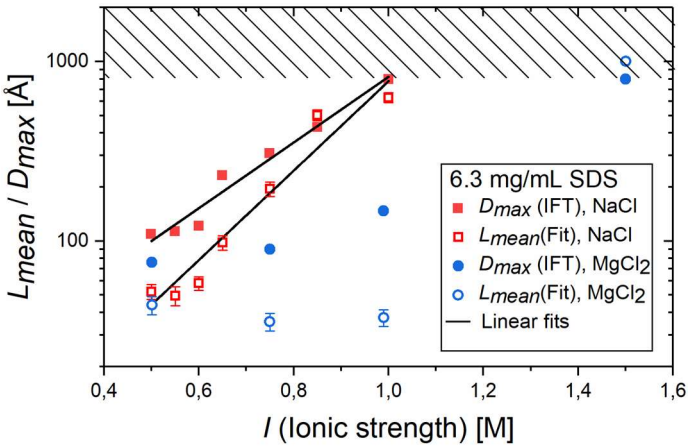

Figure 41: Comparison of the obtained estimations of the lengths from indirect Fourier transformations (IFT) and from fitting analytical models to SAXS data from SDS micelles with NaCl (red) and MgCl2 (blue). Note that the obtained values from IFT calculations are systematically higher. The shaded area marks the lengths longer than the estimated maximum resolvable dimension obtained from the minimum q-value in the data set.

It is also interesting to compare the SAXS data to the results from the indirect Fourier transformations as these calculations gives another indication of the micellar lengths. This comparison can be seen in Figure 41 together with linear fits to the data from NaCl. The data derived from IFT of SDS in both NaCl and $MgCl_2$ did indeed show a seemingly exponential increase in the maximum dimension D_{max} which is a parameter that can be interpreted as a measure of the contour length of the micelles. The values are, however, systematically larger compared to the values obtained from the fitting to the scattering data. This is attributed to the fact that the D_{max} parameter describes the contour length of the longest micelles in the solution, while the values obtained from model fitting is a mean contour length obtained from a distribution of lengths and should by this argument be shorter. It should also be noted that the length of the micelles obtained from the fits for some of the $MgCl_2$ samples seems to be underestimated as the lengths are decreasing after the first point and deviates strongly from the values obtained from IFT. This was, however, not seen to the same degree for higher concentrations of SDS.

4.1.7 Experimental phase diagrams of SDS in aqueous solutions of NaCl and $MgCl_2$

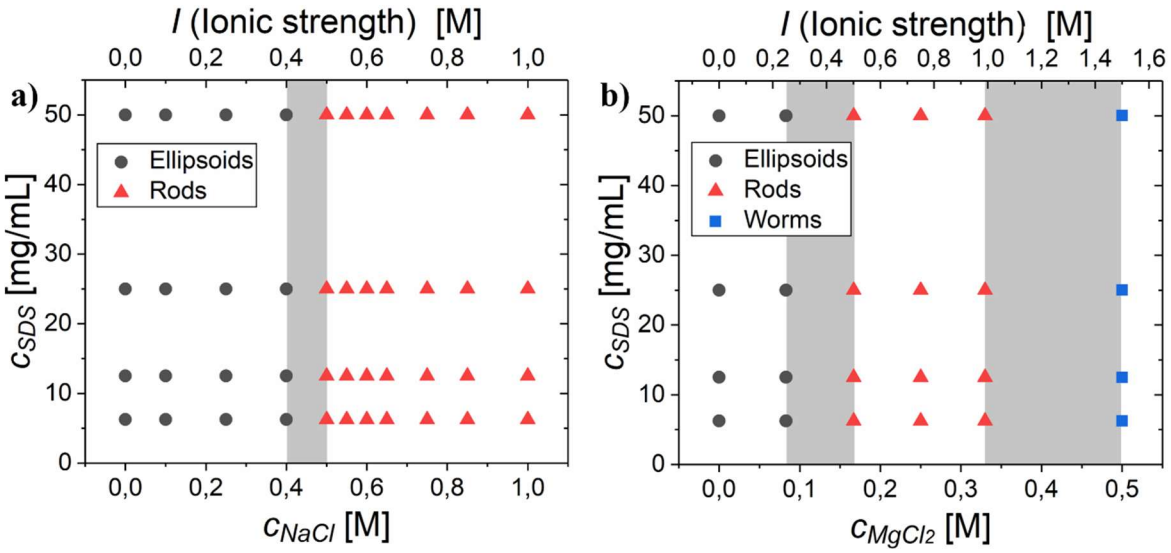

Figure 42: Experimental phase diagrams of SDS micelles in aqueous solutions of **(a)** NaCl and **(b)** $MgCl_2$ obtained by fitting SAXS data to analytical models. The grey areas highlight the transitions between ellipsoids and rods, and rods and worms.

Based on the model fits to the scattering data described in the previous sections, morphological phase diagrams for SDS micelles in aqueous solutions of NaCl and $MgCl_2$ could be derived. These diagrams can be seen in in Figure 42 (a) and (b) and illustrate the effects of SDS concentration, salt concentration, and ionic strength of the solution on the morphology of the micelles.

At low salt concentrations, ellipsoidal micelles are present in the solutions (black circles) as indicated by indirect Fourier transformations and model fits. Then, from 0.400 M NaCl and 0.0835 M $MgCl_2$, a transitional region drawn in grey is shown to indicate where the morphology changes from ellipsoidal to short rod-like micelles. Due to the similarity in the scattering patterns arising from prolate ellipsoids and short rods, it is difficult to pin-point the exact transitional concentration and the region might be wider than what is indicated in the figures. It is also a dynamical system where both morphologies are likely to be present at certain concentrations. In terms of molar concentration, the transition occurs earlier for SDS with NaCl than with $MgCl_2$, which was expected behavior due to the higher valence of the magnesium cation. It is thus more convenient to compare the two salts in terms of the ionic strength of the solution as explained in Section 2.1.3. The transitions then occur in the interval 0.400 M $< I <$ 0.500 M for SDS with NaCl and 0.250 M $< I <$ 0.500 M for $MgCl_2$. When the effect of the higher valence of the magnesium cation and ratio between the ions are accounted for, the transition regions from the two salts overlap. However, more data points in the $MgCl_2$ phase diagram are needed to obtain a narrower transition interval to fully conclude that the transitions truly coincide.

Above these salt concentrations, the micelles were first found to exist as rod-like micelles (red triangles). Here, the micelles start to increase exponentially in the contour length with increasing salt concentrations and can potentially become flexible at the highest concentrations. However, no signs of

flexibility and worm-like micelles were found for most concentrations of salt and SDS as setting the Kuhn length $b > L_c$ was required for the model to fit the data. The only clear evidence for an apparent Kuhn length lower than the contour length was found for SDS in 0.500 M $MgCl_2$. These observations contradicts results from similar systems studied in references [11, 12] where worm-like micelles were observed at similar concentrations of SDS and NaBr or NaCl.

The phase diagrams can also illustrate the effect of SDS concentration on the micelle morphology. Although the cylindrical micelles increased in length, no transitions from ellipsoids to cylindrical micelles were detected as a function of SDS concentration alone.

To summarize, these results show that the morphology of SDS micelles is impacted by the change in salt concentration and ionic strength. The transition regions from ellipsoids to cylindrical micelles in the phase diagrams of SDS with NaCl and $MgCl_2$ did not overlap in terms of molar concentration, but rather in terms of the ionic strength. For the contour lengths of the cylindrical micelles, on the other hand, large differences were found when comparing SDS solutions from the two salts. The lengths were systematically lower for $MgCl_2$, both when comparing the solutions in terms of salt concentration and ionic strength. Measurements of more concentrations of $MgCl_2$ are still needed to draw firm conclusions on the comparisons between the salts. Although it is slower and less available, it could also be useful to complement the result with measurements from SANS due to the more convenient contrasts. Furthermore, to find a mechanism explaining the effects of the cation and ionic strength using scattering techniques alone is difficult as it requires detailed knowledge of the complex interactions between the counter-ions and the layer of head groups in the micelles. Computer simulations using molecular dynamics can, however, in combination with data from scattering techniques contribute to the understanding of this behavior as it can model the dynamics of the molecules at these length scales [23, 24, 40-43].

4.2 Investigation of the structure and water permeability of PBLG-PLL nanostructures

The PBLG-PLL copolypeptides (I, II and II) were assumed to form vesicles in aqueous solution. To investigate this assumption, transmission electron microscopy and dynamic light scattering experiments were performed and the results from these measurements will be presented in Section 4.2.1. and 4.2.2. These results were then used as a basis for modelling and interpretation of synchrotron small-angle X-ray scattering data from solutions of the different copolypeptides PBLG-PLL I, II and II as presented in Section 2.4.5. The copolypeptides were measured in solutions of varying pH, salt concentration, temperature, as well as from solutions disturbed by sonication. The results from these measurements and analysis will be presented in Section 4.2.3. Lastly, results from the study of water transport across the membrane of the copolypeptide vesicle using time-resolved small-angle neutron scattering is presented and discussed in Section 4.2.4. Before analyzing results from DLS and TEM, it is advantageous to have estimates of the sizes of potential self-assembled nanostructures formed by the copolypeptides. Calculating the minimum and maximum lengths of the PBLG-PLL chains gives reasonable approximations for these values. The contour length of each amino acid in a typical protein varies from 0.34 nm to 0.40 nm [97]. Assuming a contour

length a of 0.4 nm in PBLG-PLL I, II and III, the length of a fully extended chain with n amino acid units, and thus also the maximum possible radii of a PBLG-PLL micelle, will be given by $l_{max} = na$. The actual radius of such a micelle, however, is expected to be considerably shorter than the length of the fully extended chain due to the flexible and foldable nature of polymer molecules. A more realistic value is given by the so-called end-to-end distance of the chain, illustrated in Figure 43. An estimate of this distance can be calculated by considering a chain consisting of n monomers each with the same length a following a random walk behavior without any interactions between the monomers. The mean end-to-end distance is then given by $l_{ee} = \sqrt{\langle \bar{r}^2 \rangle} = \sqrt{n}a$ [16]. Although this model is likely to miscalculate the actual length by not including restrictions in bond angles, rotations and intramolecular interactions, it should be accurate enough to distinguish micelles from vesicles in the later analysis. The two morphologies can be separated if the particle radii are known because micelles would have radii around twice the estimated end-to-end distances of the PBLG-PLL chains (Figure 43). Vesicles, on the other hand, would have radii much larger than these values due to the large internal void and the surrounding bilayers. An overview over the calculated contour lengths and end-to-end distances for PBLG-PLL I, II and III can be seen in Table 12. As seen here, the lengths of the fully extended chains are approximately ten times longer than the calculated end-to-end distances. The actual lengths present in solutions were assumed to be closer to the end-to-end distance.

Table 12: Overview over the calculated minimum lengths (end-to-end distances) and maximum contour lengths for PBLG-PLL I, II and III.

	l_{ee}	l_{max}
PBLG-PLL I	4.8 nm	57 nm
PBLG-PLL II	5.6 nm	68 nm
PBLG-PLL III	6.0 nm	88 nm

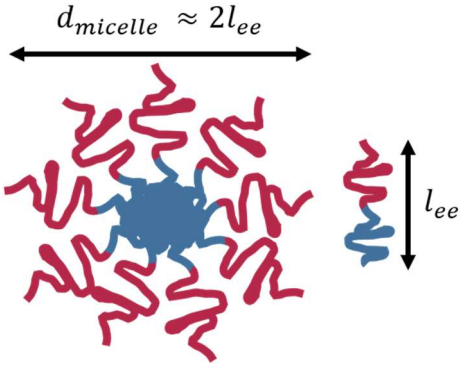

Figure 43: Schematic drawing illustrating the end-to-end distance l_{ee} and the estimated diameter $d_{micelle}$ of a copolymer micelle.

4.2.1 Global structure characterization using transmission electron microscopy

Selected images obtained using transmission electron microscopy of dried and stained (4 % uranyl acetate) solutions of PBLG-PLL I in water at room temperature can be seen in Figure 44 (a-f). The samples were prepared according to the protocol in Section 3.1.4. The images (a-c) show clear evidence of vesicles with diameters varying around 100 nm. Most importantly, a thick, bright layer surrounding the black core can be observed for all these structures which is typical appearance for negatively stained bilayer membranes [73, 74]. The vesicles were, however, not found abundantly, and a variety of other structures were also

frequently observed and found to dominate certain areas. Interestingly, image (d) shows the presence of numerous bright spherical particles in the background with diameters approximately ten times smaller than the vesicles (10 – 20 nm). This coincides with the size of micelles formed by PBLG-PLL I as the diameters are slightly larger than twice the end-to-end distances in Table 12. Next, image (e) shows dark micrometer sized crystalline structures that are assumed to be uranyl acetate residues from the staining. It cannot, however, be ruled out that these are formed by the copolypeptides. Lastly, image (f) shows a pattern that was observed frequently and is of unknown origin. One possible explanation is that a substantial amount of the copolypeptides aggregate into amorphous structures due to the increase local concentration and precipitate upon drying and creates these drying patterns.

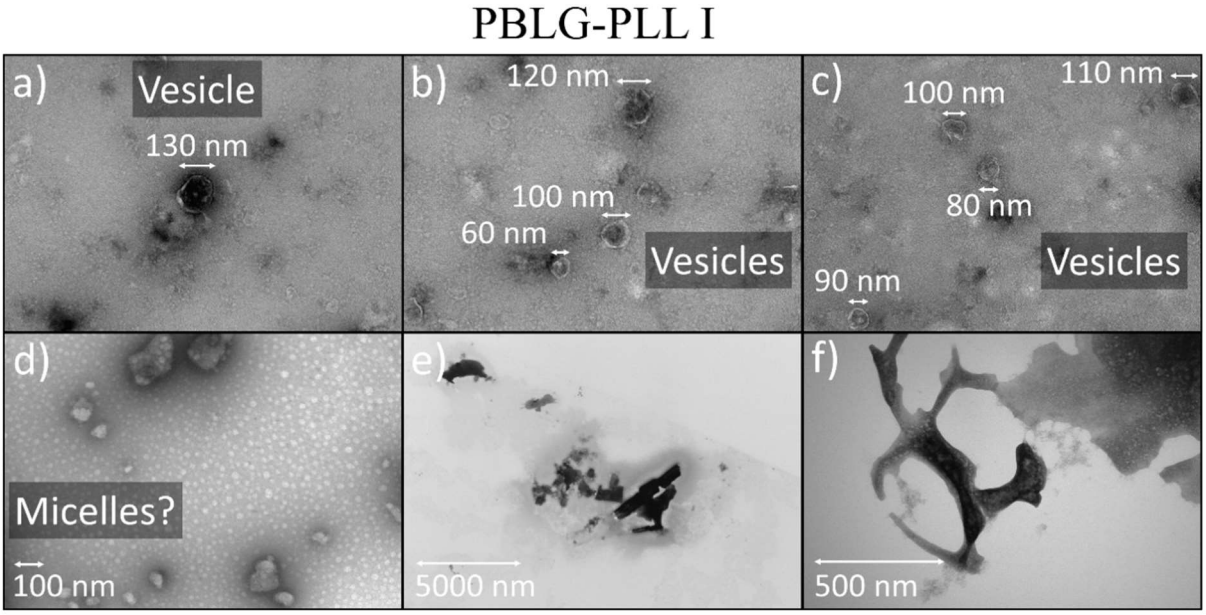

Figure 44: TEM micrographs from selected areas of dried samples of PBLG-PLL I in water stained with uranyl acetate. **(a-c)** The spherical structures with diameters around 100 nm are assumed to be vesicles due to the apparent bilayers visible in the micrographs. **(d)** Larger aggregates in addition to numerous small spherical structures with diameters approximately 10 - 20 nm in the background that coincide with the size of micelles. **(e)** Large crystalline structures possibly being crystalized uranyl acetate. **(f)** Large drying pattern of unknown origin.

TEM was also performed on dried and stained PBLG-PLL III, and a selection of the micrographs can be seen in Figure 45. The solvent was in this case tris 7.40 buffer which could potentially influence the results. To remove the buffer components, the washing procedure described in the sample preparation protocol was thus applied. As opposed to the micrographs of PBLG-PLL I, apparent self-assembled structures of sizes around 100 nm now dominate the images as seen in images (a-c).

Magnified versions of these are shown in images (d-f) to illustrate the different shapes and sizes of these structures. Evidence of vesicles with diameters up to 100 nm with apparent bilayers were found quite frequently, with an example shown in image (d). Numerous other particles with similar sizes and shapes as these vesicles were also found, but without any clear evidence of bilayers, possibly due to inadequate staining. It should be noted that the particles are in this sample apparently stained oppositely compared to the PBLG-PLL I particles in Figure 44 which had a dark core and a bright membrane. It is therefore a good chance that the particles suffered from dehydration and subsequent absorbance of the stain, or that the

stain was repelled [73]. Although with less occurrence, structures of cylindrical and worm-like shapes were observed as seen in image (e) and (f). No bilayers were observed for these, but this might also be due to the improper staining.

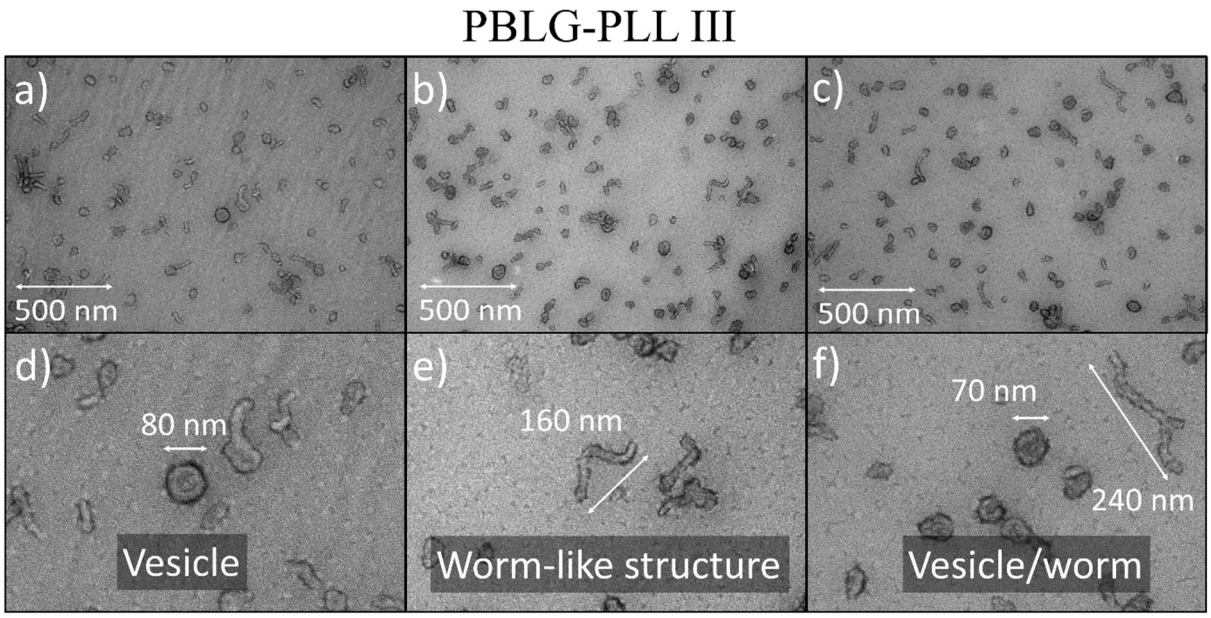

Figure 45: Selected TEM micrographs of dried samples of PBLG-PLL III (originally prepared in tris 7.40 buffer) stained with uranyl acetate. **(a-c)** Low magnification images showing a variety of spherical and cylindrical structures. **(d)** Example of possible vesicle with a diameter of 80 nm and an apparent bilayer. **(e)** Worm-like structure with a length longer than 160 nm. **(f)** Another possible vesicle and worm-like structure.

Even though drying is one of the most common methods used to image soft materials with TEM, it is also one of the riskiest as it might not produce structures fully representative of the structures in solution [73]. During drying, the concentration of copolypeptide increases dramatically before the sample is fully dehydrated. The potential vesicles are furthermore deposited on a grid coated with a carbon/Formvar composite material that the copolypeptides might interact with. It is thus not possible to conclude with absolute certainty on what is present in the original solution from images of dried samples alone. Nonetheless, the PBLG-PLL copolypeptides were expected to be decent candidates for the drying method. Although the size of such vesicles might change at high concentrations, they usually have a stable and rigid structure and a morphology that is conserved over a wide concentration range.

The micrographs from both PBLG-PLL I and III showed clear evidence of vesicle-like structures and it is possible that these were present in the original solution. The diameters were found to be considerably longer than twice the end-to-end distance of the individual copolypeptide chains making it implausible that the these are micelles. Due to the dramatic increase in concentration during drying and the final dehydration, the vesicles might enlarge or shrink in size, requiring complementary experiments to precisely determine their size. The micrographs also showed possible evidence of structures such as crystals, aggregates, drying patterns, micelles and cylinders/worms which cannot be ruled out from being present in solution together with the vesicles and potentially impact results obtained from DLS and SAS. It is, however, likely that at least some of these structures arise from the drying, from the staining.

4.2.2 Global structure characterization using dynamic light scattering

When performing structure analysis of particles using small-angle scattering data, information about the rough shape and size of the particles is useful as starting points for the model fitting. Moreover, to analyze images acquired using TEM of dried and stained samples, supporting data is needed to conclude on how representative the dried structures are to what is present in the original solution. Dynamic light scattering is a method which can be used to accomplish this quickly and reliably with small sample volumes. In this case, it was used to find the size, size distributions and possible morphologies of the self-assembled structures in samples containing PBLG-PLL I and PBLG-PLL III. If the obtained radii were found to be larger than the predicted maximum radii of micelles formed by the same copolypeptides, it would strengthen the assumption that vesicles and/or other large bilayered structures are present. Due to low availability, PBLG-PLL II could not be used for these experiments.

Dynamic light scattering measurements were first performed on a dilution series of PBLG-PLL I in water at 37 °C. Due to indications of multiple scattering at concentrations above 0.63 mg/mL, only this concentration was used in the analysis to ensure reliable results and is discussed further in the appendix Section 6.4. Measurements using DLS were later performed on 0.63 mg/mL PBLG-PLL III in tris 7.40 buffer. All measurements were repeated three times to check for reproducibility, and the errors (standard deviations) are derived from these three measurements.

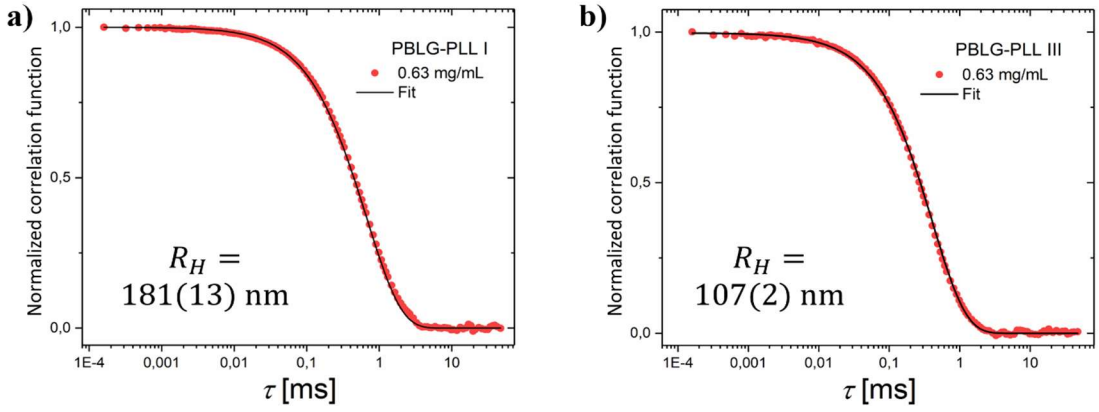

Figure 46: Plots showing example of fits to normalized cross-correlation functions obtained using DLS on solutions of **(a)** 0.63 mg/mL PBLG-PLL I in pure water and **(b)** 0.63 mg/mL PBLG-PLL III in tris 7.40 buffer at 37 °C. The hydrodynamic radii for PBLG-PLL I and III was found to be $R_H = 181(13)$ nm and $R_H = 107(2)$ nm, respectively, by fitting the stretched exponential functions to cross-correlation functions from three consecutive measurements of each sample.

In Figure 46 (a), an example of a normalized cross-correlation function obtained from DLS of 0.63 mg/mL PBLG-PLL I in pure water can be seen together with a fit using a stretched exponential function (Equation 46). The fits yielded a β-value of 0.90(2), indicating a moderate size distribution of the particles. The values from the fits were used to calculate values for the mean relaxation time, $\langle \tau_c \rangle$, and subsequently the diffusion coefficient D. By lastly using the Stokes-Einstein relation, an apparent hydrodynamic radius of $R_H = 181(13)$ nm was obtained. This is expected to be slightly larger than the actual radius due to the accompanying hydration layer. The same process was applied for the cross-correlation functions obtained

from PBLG-PLL III in tris 7.40, and the result can be seen in Figure 46 (b). It yielded an apparent hydrodynamic radius of $R_H = 107(2)$ nm with $\beta = 0.91(1)$, which again indicates a moderate distribution in size.

Due to the indicated distributions, the cross-correlation function were fitted using the NNLS evaluation algorithm explained in Section 2.2.2 to characterize the potential multimodalities and distributions of the systems. Excellent fits were obtained, and examples of these together with the corresponding weight and number weighted distributions curves for PBLG-PLL I and PBLG-PLL III can be seen in Figure 47 and Figure 48, respectively. For PBLG-PLL I, the distribution curves indicated the presence of two particle populations centered around hydrodynamic radii of 42(2) nm and 181(13) nm and with full width at half maximum (FWHM) values of 20(2) nm and 91(9) nm, respectively. The distributions curves from PBLG-PLL III also indicated two populations, but with the slightly larger hydrodynamic radii of 65(6) nm and 265(17) nm, and with FWHM values of 27(2) nm and 108(6) nm, respectively. The hydrodynamic radii are mean values of the particle sizes at the maxima of the distribution functions from three consecutive measurements with corresponding standard deviations. The FWHM values were calculated by fitting the peaks with Gaussian functions, and are also specified as the mean value from three measurements with corresponding standard deviations.

The obtained hydrodynamic radii from both samples and fitting procedures are all larger than the calculated end-to-end distances of the PBLG-PLL chains presented earlier. The solutions can thus be assumed to be dominated by structures larger than micelles, and these structures are therefore likely to be bilayered. DLS cannot in this set-up, however, distinguish between vesicles and other bilayered structures such as hollow cylinders. The obtained radii are furthermore based on the calculation of the radius of a sphere moving by Brownian motion and will not give correct values for cylindrical structures. Interestingly, the populations with the smallest radii in Figure 47 (b) and Figure 48 (b) are both centered around radii corresponding to particle sizes close to 100 nm which match the measured diameters of the vesicles seen using TEM in Section 4.2.1.

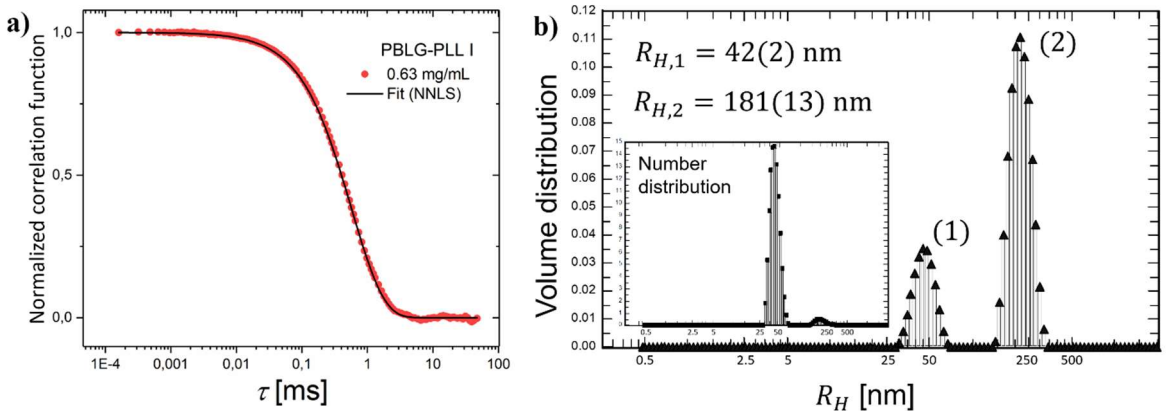

Figure 47: Example of a fit to the cross-correlation function obtained using DLS on solutions of (a) 0.63 mg/mL PBLG-PLL I in pure water at 37 °C. **(b)** Calculated distribution curve from the presented fit using the NNLS evaluation algorithm. The hydrodynamic radii and standard deviations displayed in the plot are calculated from the particle size at the maxima of the distribution functions from three consecutive measurements. The inset shows the number weighted distribution function.

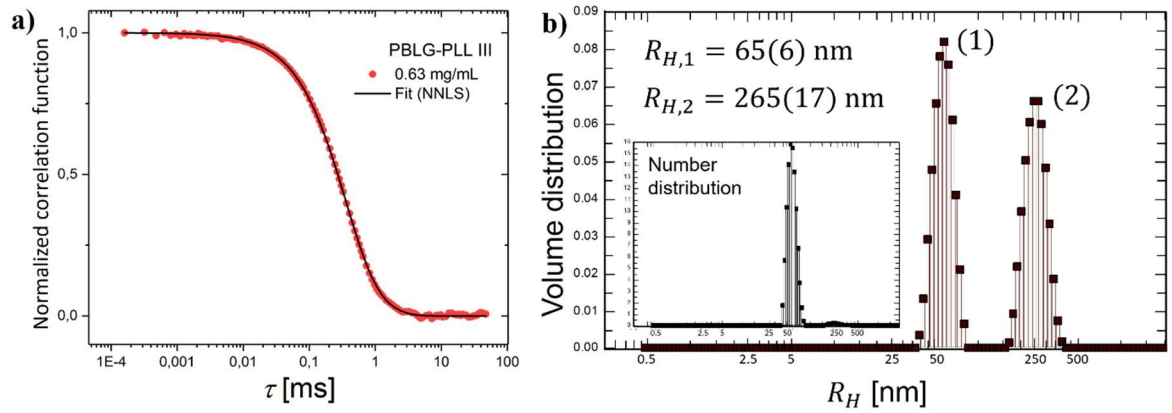

Figure 48: (a) Example of a fit to the cross-correlation function obtained using DLS on a solution of 0.63 mg/mL PBLG-PLL III tris 7.40 buffer at 37 °C. **(b)** Calculated distribution curve from the fit using the NNLS evaluation algorithm. The hydrodynamic radii and standard deviations displayed in the plot are calculated from the particle size at the maxima of the distribution functions from three consecutive measurements. The inset shows the number weighted distribution function.

4.2.3 Detailed structure characterization using SAXS

For the characterization of the detailed internal structure of the potential PBLG-PLL copolypeptide vesicles in pure water, SAXS data from this system was collected at the ID02 beamline at ESRF. Figure 49 shows the normalized scattering curves from PBLG-PLL I, II and II with a q-range corresponding to the approximate size domain ranging from 0.4 nm to 1400 nm in real space (according to Equation 51 in Section 2.4). Scattering data from larger q-values were also obtained (wide-angle X-ray scattering), but are not included here due to a weak scattering signal which yielded non-reproducible scattering curves.

Qualitatively, all three curves exhibit features at low q-values indicating the presence of structures with sizes up to 1400 nm. If they were smaller, one would expect a plateau-like behavior at the lowest q-values which is not seen in the scattering curves. There might nevertheless be smaller structures present in the solution that are not as visible due to the intense scattering from large structures compared to smaller structures. The large structures might be attributed to long, cylindrical bilayered structures similar to those seen using in TEM. The presence of large structures was also seen using DLS in the previous section.

From a qualitative comparison of the three curves from the inset in Figure 49, one can observe noteworthy differences in the scattering patterns at q-values lower than 0.01 $Å^{-1}$ for PBLG-PLL I compared to II and III. The only major difference between the three copolypeptides are the length of the hydrophilic PLL block, being 82, 120 and 151 blocks for PBLG-PLL I, II and III, respectively. Based on this, the change in the scattering pattern indicates a change in the large scale structure arising from the increased PLL block length. This confirms the results from DLS where the PBLG-PLL III particles were found to be slightly larger than those formed by PBLG-PLL I. Since the scattering overlaps for the three systems at higher q-values, the structure at smaller length scales in real space appears to be conserved.

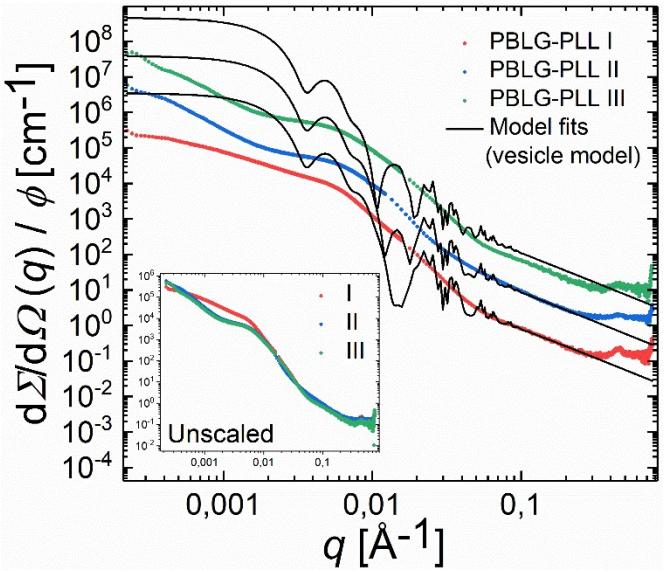

Figure 49: Points: Normalized synchrotron small-angle scattering curves from 5.0 mg/mL PBLG-PLL I, II and III in aqueous solutions at 37 °C obtained from the ID02 beamline at ESRF, Grenoble, France. **Lines:** Simulated scattering curves using the vesicle model with values from DLS and TEM. The curves are multiplied by 10^n where n runs from 0 to 2 for clarity. **Inset:** Normalized scattering curves to illustrate the differences at low q-values when increasing the PLL block length. The length is increased from PBLG-PLL I to III.

An attempt was made to fit the analytical vesicle model presented in Section 2.4.5 to the scattering curves in Figure 49. The scattering length densities for the polymer chains were estimated using literature values for the partial specific volumes of PBLG (0.75 cm^3/g [98]) and PLL (0.71 cm^3/g [33]) chains yielding $1.2 \cdot 10^{11}$ cm^{-1} and $1.3 \cdot 10^{11}$ cm^{-1}, respectively. Apart from the SLDs and concentrations, the rest of the parameters were set as fit parameters.

Interestingly, the vesicle model was not able to produce fits which overlapped satisfyingly to the experimental data. An attempt was made to vary the SLDs manually and performing the fit procedure using a different code with the same form factor to rule out potential sources of errors, but this also failed to describe the data. Moreover, the poor fits are not due to possible non-equilibrium structures or errors made during the experiments as the scattering patterns were found to be reproducible and stable over time (discussed later in Section 4.2.4). The simulated curves presented in Figure 49 were produced using values based on the results from TEM and DLS to illustrate the discrepancy between these results. The parameters used to produce the curves can be seen in Table 20 in the Appendix Section 6.5. While vesicles of these sizes might be present, the failure of the vesicle model to explain the data can be explained to the presence of other large structures in the solution which dominate in the scattering signal.

4.2.4 Stability and reproducibility

Since the structure of the PBLG-PLL particles could not be resolved in the previous section using the analytical model describing vesicle scattering, the data was checked for issues with reproducibility and stability to rule out the presence of possible non-equilibrium structures and experimental errors. Scattering data from the ID02 and BM29 beamlines at ESRF, Grenoble, France were therefore compared and can be

seen in Figure 50 (a) and (b). For PBLG-PLL I in (a), two freshly prepared samples yielded overlapping scattering curves at two different instruments measured at two different occasions. The same was true for PBLG-PLL III in (b), which also compare the scattering from a freshly prepared sample to a three months old sample. It can from these results be assumed that the particles contributing to the scattering are stable over time and in equilibrium, and that the results are the same independent of which instrument being used.

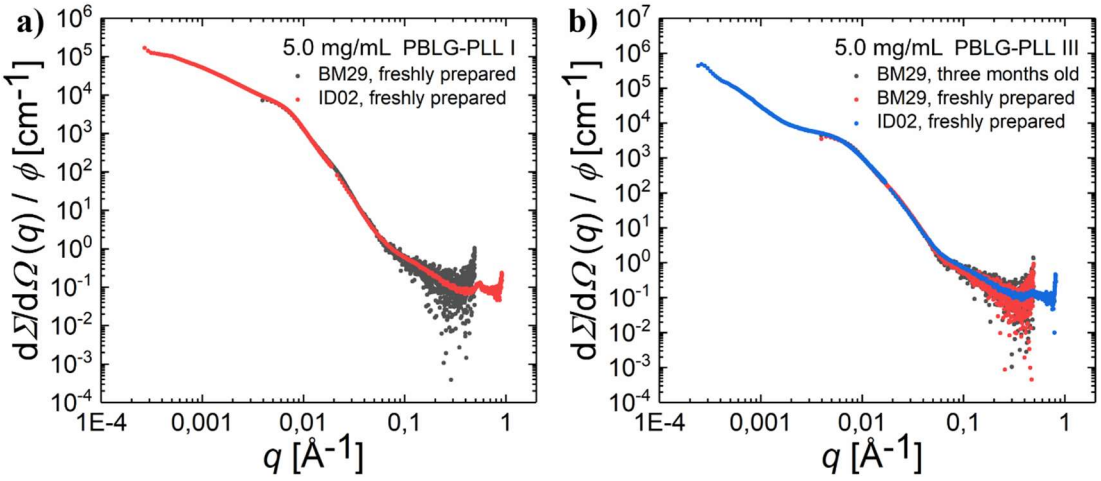

Figure 50: **(a)** The comparison of scattering curves from two different samples containing 5.0 mg/mL PBLG-PLL I in water measured at two different instruments (BM29 and ID02, ESRF, Grenoble) shows excellent reproducibility. **(b)** Overlapping scattering curves from the same sample containing 5.0 mg/mL PBLG-PLL III in tris 7.40 buffer measured twice three months apart (BM29, ESRF, Grenoble) indicates stability over time. 5.0 mg/mL PBLG-PLL III in pure water was also measured using another instrument (ID02, ESRF, Grenoble) which confirms this stability and shows that the scattering curves are reproducible.

4.2.5 Effects of variations in solvent conditions

A series of experiments were conducted to investigate the effects of copolypeptide concentration and of different solvent conditions such as different pH, temperature and presence of salts, as well potential non-equilibrium structures that might be provoked by sonication of the solution. Due to the issues in the model fitting, the scattering curves were only analyzed qualitatively. The effects were mainly studied on samples containing PBLG-PLL III in tris 7.40 buffer using SAXS data from the BM29 beamline at ESRF, Grenoble, France with a q-range corresponding to the approximate size domain ranging from 6 nm to 800 nm in real space. Only PBLG-PLL III was chosen for these experiments due to difficulties in dissolving PBLG-PLL I in buffers, low availability of PBLG-PLL II and limited amount of synchrotron beam-time.

First, the effect of copolypeptide concentration on the scattering patterns was investigated. The normalized scattering curves from dilution series of PBLG-PLL I in water and PBLG-PLL III in tris 7.40 buffer can be seen in Figure 51 (a) and (b), respectively. For PBLG-PLL I, there appears to be a small effect of concentration on the scattering in the low q-range when increasing the concentration from 0.63 mg/mL to 1.3 mg/mL. Above this concentration, the curves overlap completely. Since PLL is charged and basic, it was desirable to dissolve the copolypeptides in tris 7.40 buffer to stabilize the pH and mimic biological conditions. However, due to problems with phase separation when dissolving PBLG-PLL I in buffer, this was only achieved for PBLG-PLL III. The concentration effect might therefore be caused by the lack of buffer as

no signs of this kind of shift was seen in the scattering patterns for PBLG-PLL III with buffer in Figure 51 (b).

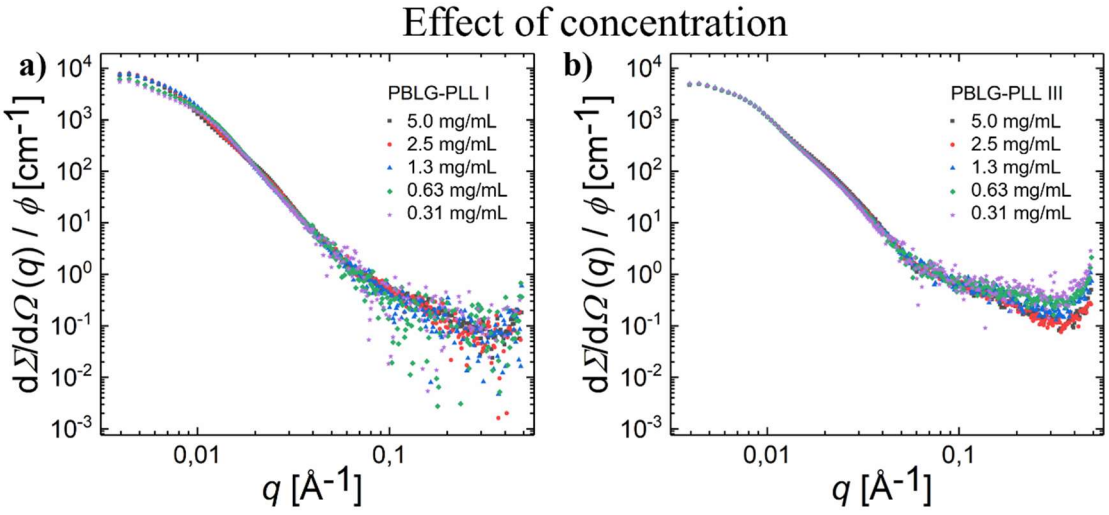

Figure 51: Normalized scattering curves from dilution series of PBLG I in water **(a)** and PBLG III in tris 7.40 buffer **(b)**. A small concentration effect can be seen for PBLG-PLL I.

Next, the impact of variations in pH on the scattering patterns and potential vesicles were investigated. As mentioned in the introduction (Chapter 1), PLL chains exhibit a transition in the secondary structure from random coils to alpha helices at a pH close to the $pK_a \sim 10.5$ of PLL [33, 34] which is known to cause morphological changes in other PLL-based vesicles [32]. This behavior could be exploited drug-delivery applications where a shift in pH can act as a potential trigger for the release of drugs by affecting the permeability of the membrane or by changing the morphology of the vesicle. It was therefore attempted to investigate this transition and its potential effect on the vesicles by using SAXS to measure samples containing PBLG-PLL III dissolved in buffers with pHs ranging from 3.50 to 11.5 (buffer compositions are described in Section 3.1.2). The samples with buffers of pH 3.50, 10.0 and 11.5 were all found to have phase separated as crystals could be observed in the solutions. Different types of buffers were also tried to check for possible incompatibilities with certain chemicals, but the same behavior was seen. Based on these results, the charges seem to affect the inter-particle interactions, and structure cannot be maintained with alpha helical PLL blocks.

Despite the issues, SAXS measurements were performed on the solutions, and the resulting normalized scattering curves can be seen in Figure 52. The scattering curves from pH 10.0 and 11.5 are clearly affected by the phase separation as the intensity is substantially lowered compared to pH 7.40. The lowered intensity is not seen for pH 3.50, but due to the observed crystals, the data was assumed to be unreliable and it is not possible characterize the alpha helical PLL blocks and their effect on the vesicles. The only reliable information gathered from the experiment was from pH 7.40 and 9.00, where the scattering profile for the two samples overlap completely. A change in secondary structure would be visible in this q-range, and it can therefore be concluded that the transition has not yet happened at pH 9.00. This confirms the known point of transition close to a pH of 10.5.

.

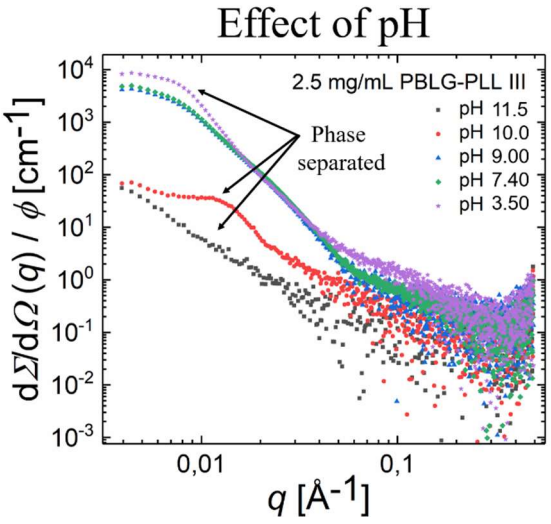

Figure 52: Normalized scattering curves from 2.5 mg/mL PBLG-PLL III dissolved in buffers with varying pH. The solutions with pH 3.50, 10.0 and 11.5 were found to phase separate and consequently these measurements could not yield reliable data.

Another external parameter that can potentially impact the structure of copolypeptide vesicles is the solvent temperature. To study this, scattering data from 2.5 mg/mL PBLG-PLL III in tris 7.40 buffer was acquired using SAXS while the temperature of the solution was varied from 10 °C to 40 °C in steps of 5 °C (expect for one measurement at 37 °C). The samples were allowed to equilibrate between the temperature jumps and subsequent measurements. In Figure 53, the normalized scattering curves can be seen. Surprisingly, the scattering curves overlap completely at all temperatures and no effect of temperature on the structure can be observed in this q-range.

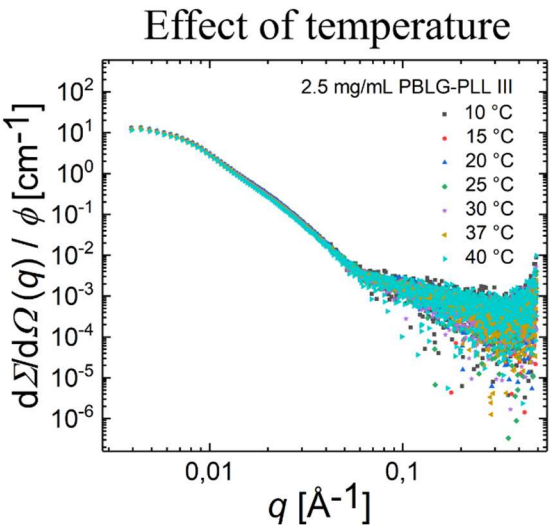

Figure 53: Normalized scattering curves from 2.5 mg/mL PBLG-PLL III in tris 7.40 buffer at temperatures varying from 10 °C to 40 °C. No effect on the scattering curves can be observed.

Next, NaCl was added to the samples in a similar way as for the SDS system to investigate the role and effects of charges in the PBLG-PLL copolypeptides. The scattering curves from samples of 2.5 mg/mL PBLG-PLL III in tris 7.40 buffer with varying concentrations of NaCl can be seen in Figure 54. It should be noted that phase separation occurred when the salt concentration was increased above 0.250 M. These samples were for this reason not included in the measurements. The scattering curves from the solutions with added salt with concentrations ranging from 0.0625 M to 0.250 M completely overlap with the reference sample without salt. This implies that the structures present in the solution are unaffected by the increase in salt concentration in the size domain available for study in this experiment. Since PLL chains are highly charged at pH 7.40 [34], added salt will screen the charges in a similar way as for the shielding of the charges in SDS micelles. As no effects on the scattering curves can be observed, it is likely that the charge of the PLL chains is not important for the internal structure of the vesicles. The observed phase separation occurring at high salt concentrations, however, suggests that the charges are important for the inter-particle interactions. These arguments can also be applied for the measurements with varying pH where phase separation occurred at a pH above 9. Raising the pH from 7.40 to 9.00 did not cause any apparent changes in the internal particle structure even though the charges of the PLL chains are reduced from pH 7.40 to pH 9.00. Phase separation finally occurred at pH 10.0 and above as the charges are reduced even further, which indicates that the lower charge influences the inter-particle interactions.

.

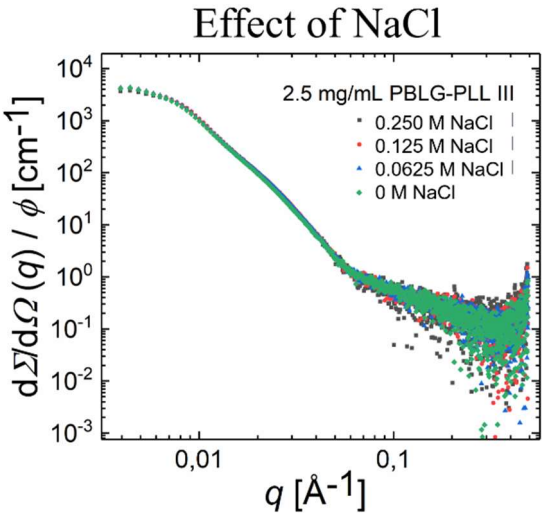

Figure 54: Normalized scattering curves from 2.5 mg/mL PBLG-PLL III in tris 7.40 buffer with added NaCl. No effect of salt can be observed in the scattering curves.

Lastly, a sample containing 2.5 mg/mL PBLG-PLL III in tris 7.40 buffer was sonicated with a frequency of 37 kHz for 5 minutes in an ultrasonic thermal bath (Elmasonic P from Elma Schmidbauer GmbH, Germany) at 37 °C. The sample was then measured as soon as possible to capture and characterize potential non-equilibrium structures and kinetics. The time from sonication to the measurement was approximately 5 minutes. In Figure 55 the resulting normalized scattering curve can be seen together with the non-sonicated reference. Again, the curves show a complete overlap and no potential non-equilibrium structures could be captured with this experimental set-up. Non-equilibrium structures might still have

been present before the measurement started. It should again be noted that the scattering curves are reproducible and stable over time as seen in Section 4.2.4. Based on this, the vesicles are assumed to be in equilibrium in the non-sonicated sample.

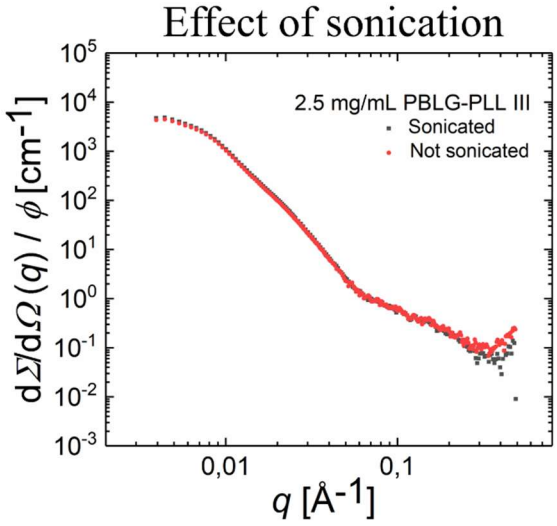

Figure 55: Normalized scattering curve from 2.5 mg/mL PBLG-PLL III in tris 7.40 buffer before and after 5 minutes of sonication in an ultrasonic thermal bath. The sonication was performed approximately 5 minutes prior to the measurement. The scattering curve is unaffected by sonication at the time of measurement.

To summarize, all SAXS measurements used to study the effect of varying solvent conditions on the copolypeptide self-assemblies show evidence of remarkably stable structures in the q-range that was available for study. The scattering from PBLG-PLL I in pure water showed a minor sensitivity to copolypeptide concentration, while the scattering from PBLG-PLL III in tris 7.40 buffer remained unchanged. The rest of the experiments were conducted on PBLG-PLL III. Also no effects on the scattering curves were observed by changing the pH from 7.40 to 9.00. However, due to phase separation, it was not possible to study the potential alpha helix transition at higher pHs. Furthermore, the scattering curves proved to be insensitive to temperature, added salt and to sonication.

It should be noted that the nanostructures present in the solutions are only assumed to be vesicles, and other morphologies such as long bilayered cylinders are likely to co-exist with the vesicles due to the presence of scattering curve features at very low q-values. Still, by qualitatively studying the effects on the scattering patterns, one can to a certain degree conclude on the overall structural stability of the structures present in the solution. The use of other analytical models and/or more experimentation on the vesicle preparation protocol can potentially solve this problem. Other combinations of techniques, concentrations and solvents can possibly produce solutions containing only the vesicular phase that can produce resolvable scattering curves.

Assuming that the main structures present in the solutions are vesicles, their remarkable stability to variations in the solvent conditions make them intriguing candidates in applications such as site-specific drug delivery. If future experiments can lead to a method of deliberately reducing their stability and completely change the structure by i.e. changing the pH, this would further support their potential for use in these applications. In this way, drugs can be loaded into the water-filled core and stay fully contained

under the variety of solvent conditions and environments encountered in a biological system, before the drug is being released by a local or external trigger.

Furthermore, it is interesting to compare the copolypeptide system to the SDS micelles in aqueous solutions with and without salt. Although with different block length ratios, both systems share the feature of being composed of one hydrophobic part and one charged hydrophilic part. For SDS, the charge of head groups is the driving force in the morphological transitions and the system is very sensitive to changes in the solvent conditions. It was showed that adding salt introduced major changes in the morphology of the system by screening the head group charges. The internal structure and morphology of the PBLG-PLL self-assemblies, on the other hand, proved to be remarkably stable and insensitive to charge screening from salt and moderate changes is pH.

4.2.6 Permeability of vesicle membranes studied using time-resolved small-angle neutron scattering

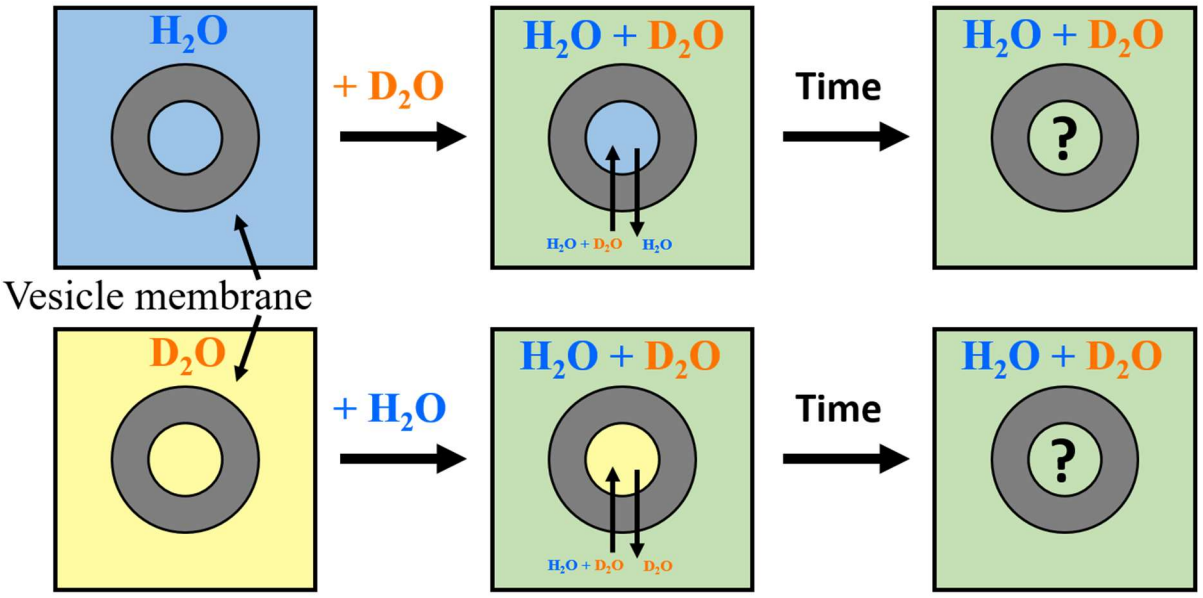

Figure 56: Illustration depicting how water transport through vesicle membranes can be studied by utilizing the difference in scattering length density between H_2O and D_2O in neutron scattering.

As already mentioned, in applications such as site-specific drug delivery, it is essential to know the characteristics of the permeability of the vesicle membrane as the encapsulation, containment and release of the drug depend on this property. Time-resolved small-angle neutron scattering is a technique that can be used to study this by measuring the rate of water transport through the vesicle membranes. It is accomplished by taking advantage of the difference in scattering length density between H_2O and D_2O in neutron scattering which arises from the sensitivity of neutrons to different isotopes of the same element. Although other more accessible techniques can be used to study membrane permeability, they cannot give the same simultaneous detailed structural information as with SANS and it is therefore of great value to test and develop this method further. The other techniques are, however, more common, and includes the use

of NMR [99] and fluorescence microscopy [100] to study the water transport in copolymer vesicles. It should also be mentioned that SAXS cannot be used to perform the same experiment due to the lack of contrast between H and D with X-rays. It can still be a purposeful complementary technique by confirming that the vesicle structure is unaffected by changing the solvent from H_2O to D_2O.

Even though the previous experiments failed to characterize the self-assembled structures produced from PBLG-PLL in tris 7.40, the permeability experiments were carried out under the assumption that the vesicles and/or bilayered cylinders dominated the solution. This should be taken into account when analyzing the results as it could influence the diffusion rates.

The experimental set-up can be seen illustrated in Figure 56. PBLG-PLL III vesicles were first prepared in separate solutions containing tris 7.40 buffer made with H_2O (top) and D_2O (bottom) to yield a concentration of 10 mg/mL. As close in time to the measurement as possible ($\sim 60\ s$) , the solutions were mixed in a 1:1 ratio of D_2O and H_2O buffer, respectively, yielding 5.0 mg/mL solutions. Contrast between the solvent inside and bulk solvent outside of the vesicles has then been created as the interior of the vesicles contains either H_2O or D_2O, while the exterior solvent is a 1:1 mix of the two. Over time, the interior and exterior solvent might exchange through the membrane, resulting in a reduction in contrast. By tracking the reduction in intensity in the scattering pattern from the reduction in contrast over time, the rate of water transport can be characterized.

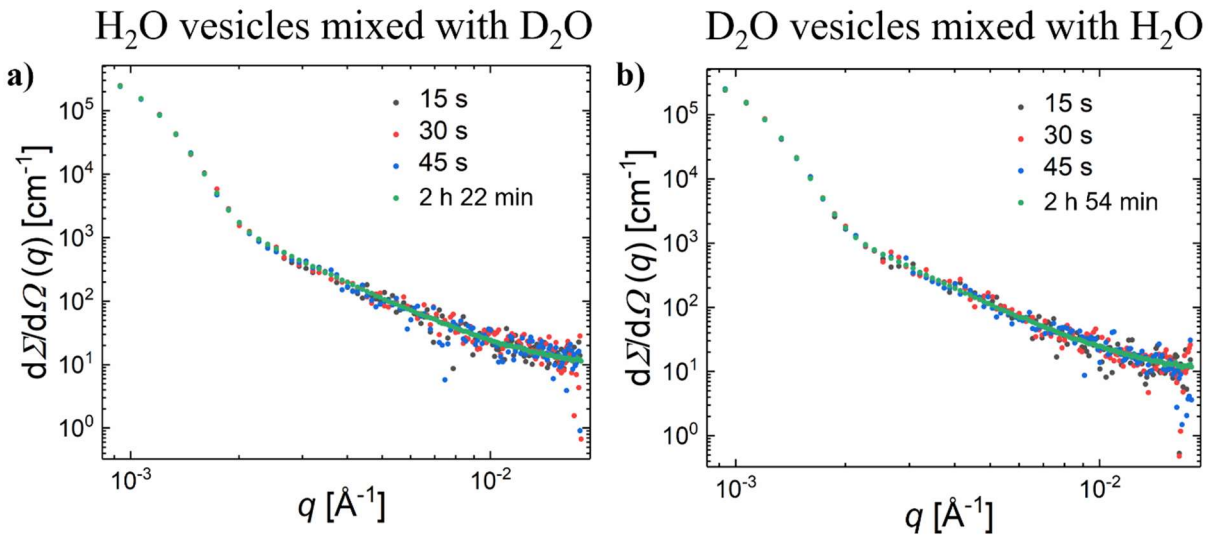

Figure 57: Selected scattering curves from SANS measurements of PBLG-PLL III vesicles prepared in **(a)** H_2O tris 7.40 buffer and **(b)** D_2O tris 7.40 buffer mixed 1 minute prior to the first captured frame in a 1:1 ratio with D_2O and H_2O tris 7.40 buffers, respectively. The scattering from the solvent is not subtracted. Frames were captured every 15 seconds for 20 minutes, before measuring again after 2 h 22 min and 2 h 54 min. As no change in the intensities could be observed after the first captured frame, the transport of water across the membrane occurred faster than what was possible to measure with this experimental set-up.

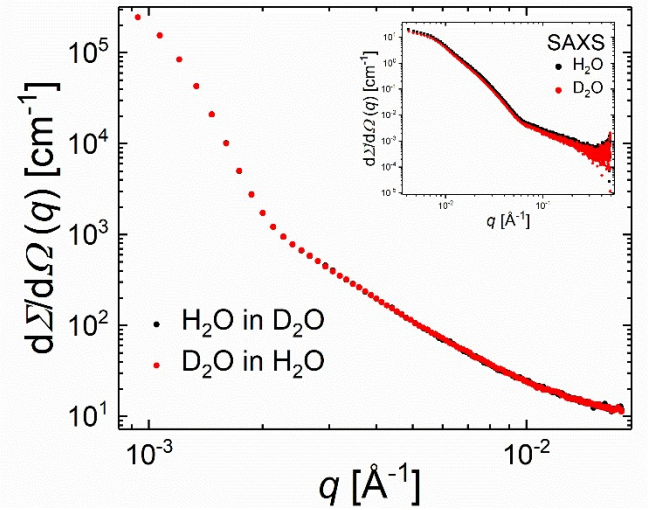

Figure 58: Comparison of scattering curves from SANS measurements of PBLG-PLL III in prepared in H2O and D2O (tris 7.40) mixed in a 1:1 ratio with D2O and H2O (tris 7.40), respectively. **Inset:** SAXS data of the same solutions, but without mixing with the opposite solvent. Apart from the small difference in scale of the intensity due to a small difference in concentration, the curves have the exact same shape indicating no influence of the deuterium on the structures present in the solution.

In Figure 57 (a) and (b), the results from the water transport measurement of the potential PBLG-PLL III vesicles are shown. In (a), data from vesicles initially prepared in H_2O can be seen, while the vesicles prepared in D_2O can be seen in (b). Both plots present the scattering at different time points which includes the first three captured frames and a longer measurement after 2-3 hours. The longer measurement time used for the last measurement is the reason for the improved statistics. In both plots, no change in intensity as a function of time can be observed. This result alone implies that the water transport occurred either faster or slower than the time scale available in this experimental set-up, and it is thus not possible to deduce the detailed kinetics of the water transport. To conclude on the time scale, the two scattering curves from both mixes after 2 h 22 min and 2 h 54 min were compared and can be seen in Figure 58. The curves overlap completely, indicating fast water transport which occurred before the first frames were captured. It furthermore shows that the addition of D_2O does not influence the structure of the self-assemblies present in the solution. This was further confirmed by measuring the same unmixed samples prepared in both H_2O and D_2O using synchrotron SAXS. The results from these measurements can be seen in the inset in Figure 58, and apart from a difference in the scale of the intensity due to small differences in concentration, the curves have the exact same shape and thus the same structure in this q-range.

The fast water transport is surprising as most known diblock copolymer vesicles are known to have thick and sometimes kinetically frozen membranes with low permeability to water [7, 28, 101]. This is in contrast to liposomes which were initially studied as potential carriers for drug molecules, but was found to be very permeable to water due to their thin and fluid bilayers [102]. For drug-delivery applications, this is usually unwanted as it can cause premature release of the drug. A possible explanation for the fast transport might be the presence of defects in the vesicle membranes which could be enough for water molecules to diffuse through. It is likely that larger drug molecules would exhibit slower rates of diffusion.

It should, however, be emphasized again that based on the findings in Section 4.2.1 - 4.2.4 it is likely that vesicles are not the only morphology present in the solutions and this could also affect the diffusion rates.

Assuming vesicles were present and the water transport occurred before the first frame was captured, another experimental set-up and neutron source is likely needed to successfully characterize the kinetics of the water transport. By using a stopped-flow device capable of mixing the vesicle solutions with H_2O or D_2O automatically, and measuring the scattering with neutrons from a modern high flux spallation source, one can possibly reach the correct time scales to follow this process. Even though the experiment was not entirely successful, it was valuable to test this type of experimental set-up as TR-SANS has not yet been extensively used in literature to study the permeability of vesicle membranes. Future developments and modern spallation sources can make the technique more accessible and improve the resolution in time, which makes the testing and development of this technique intriguing.

5 Conclusions

In this thesis, scattering techniques have been applied to obtain deeper knowledge of how self-assembled nanostructures formed by surfactants and copolypeptides in aqueous solution respond to variations in external conditions such as temperature, pH and ionic strength. The work is divided into two parts, namely, the structural characterization of SDS micelles and the investigation of the structure and water permeability of PBLG-PLL nanostructures. For SDS micelles in aqueous solutions with NaCl and $MgCl_2$, the globule-to-cylinder transition was successfully characterized using synchrotron SAXS. While the PBLG-PLL system was expected to form well-defined vesicles, it was not found possible to characterize the self-assembled structures using an analytical vesicle model. Evidence of other morphologies were found with TEM and DLS, and additional experiments are required to fully characterize the system. Lastly, the permeability to water in the proposed vesicles was measured using TR-SANS. The complete exchange of water was found to happen faster than the accessible time scale of the instrumental set-up.

The SDS micelles were found to transition from globular to cylindrical micelles at high concentrations of both NaCl and $MgCl_2$. No transitions were found as a function of SDS concentration alone, which indicate that a change in ionic strength is needed to induce the transition. For NaCl, the transition was estimated to occur at ionic strengths between 0.400 M and 0.500 M, and the transition for SDS with $MgCl_2$ was estimated to occur in a slightly wider range of 0.250 M to 0.500 M. Data from additional concentrations of $MgCl_2$ in this concentration regime are needed to draw firm conclusions on how the two transition regions coincide. It should also be noted that the addition of KCl and $CaCl_2$ caused a phase separation of the solutions and their effect on the micelles could therefore not be studied. While it is difficult to deduce the exact mechanisms of the morphological transitions using small-angle scattering techniques alone, it can be accomplished by combining the experimental results with molecular dynamics simulations; these simulations allow for a detailed study of how the counter-ions binds to the micelles and the resulting effect on the morphology can then be compared with the experimental data.

The contour lengths of the cylindrical SDS micelles grew exponentially as a function of concentration for both NaCl and $MgCl_2$, and were even found to elongate to lengths beyond the maximum resolvable distance for the SAXS set-up at the highest salt concentrations. The growth was, however, seemingly steeper for NaCl as a function of ionic strength compared to $MgCl_2$, which indicates that the growth mechanism is also affected by properties other than the ionic strength. While no signs of flexibility in the cylindrical micelles were seen with NaCl, the micelles with $MgCl_2$ formed worm-like micelles with possible branching and/or cross-linking at the highest salt concentration. It should be noted that the same ionic strength was not tested for NaCl, and the same behavior might be seen for both salts if studied at this ionic strength. Furthermore, the salts caused an apparent increase in the core radii and head group thicknesses in the globular concentration regime. After the transition into cylindrical micelles, however, the core radii decreased to a value below the value in pure water, while the head group thickness increased slightly. No significant differences between the two salts were found here. These changes can likely be attributed to geometrical constraints from the morphological transitions and changes in the layer of counter

ions and solvent at the micelle/water interface. This can again be studied in more detailed with computer simulations using molecular dynamics.

The solutions of PBLG-PLL I and III were dominated by at least two different structures which were likely to be bilayered vesicles and/or bilayered hollow cylinders as indicated by TEM images and size estimations from DLS. The characterization of the structure by fitting an analytical vesicle model to SAXS data was therefore not successful. Nevertheless, the structures were by qualitative analysis of the scattering data found to be remarkably stable when subjected to changes in the solvent conditions. No apparent structural changes were observed by varying pH, salt concentration, temperature or when applying sonication. High concentrations of salt and major shifts in the pH did, however, cause a phase separation of the solution. Based on this behavior, it is likely that the charges of the PLL chains are important for the inter-particle interactions and not for the internal structure. Moreover, the increase in length of the PLL chain from PBLG-PLL I to III were found to cause a shift in the scattering pattern at q-values corresponding to large distances in real space. This confirmed results from DLS that showed an increase in particle sized from PBLG-PLL I to PBLG-PLL III. More experiments and analyses are needed to draw firm conclusions on the behaviors of the system as it is not certain what type of structures that dominated the scattering signals.

Using time-resolved SANS, the water transport through the presumed bilayered vesicles were found to have happened before the first scattering pattern was captured. This indicated that the complete exchange of water happened at a time scale of second or less, which is not typical for copolymer vesicles due to the thick and hydrophobic inner shell. This could, however, be explained by the presence of defects in the bilayer that could allow water molecules to penetrate. While this can lead to premature release of drugs in drug delivery applications, it is likely that the membrane is less penetrable to larger molecules. It should also be emphasized that the presence of other morphologies than vesicles could impact the diffusion rates. Measurements using a stopped-flow set-up and a modern spallation sources is more likely to capture this process and can be used to further develop this method of measuring membrane permeability.

Both of the studied systems consisted of amphiphilic molecules with charged hydrophilic parts which self-assembled in aqueous solutions. This allowed for studies of the effects of different solvent conditions on the structure of several different nanomorphologies. As explained in the introduction, structures formed by amphiphilic molecules like the ones used in this work are usually very sensitive to parameters such as ionic strength and temperature as the predominant physical behaviors happen at an energy scale comparable with the thermal energy at room temperature. This was, however, only the case for one of the systems. The SDS system proved to be highly dynamic and sensitive to the addition of salt due to the importance of the head group charges on both the internal structure of the micelles and the interactions between micelles. Conversely, the internal structure formed by the self-assembly of the PBLG-PLL copolypeptides were found to be extraordinarily stable over a wide range of solvent conditions. While the charges of the hydrophilic PLL block did not seem to be important for the internal structure, they were found to be important for the inter-particle interactions. The increase in length of the PLL block did, however, seem to increase the overall size of the particles. Some of the properties of the copolypeptides vesicles proposed in this work are highly wanted in applications such as site-specific drug delivery to ensure proper containment of the drugs. With more research on potential triggers for the safe release of the drugs

from the water-filled core and on the membrane permeability, copolypeptide vesicles similar to those presented here might be used with success in such technologies in the future.

6 Appendix

6.1 List of chemicals

Table 13: List of all chemicals used for the experiments in this work.

Chemical	Supplier
Used for all systems	
Milli-Q ultrapure water (type I)	Merck Millipore
Sodium chloride ≥ 99.9 %	VWR Chemicals
Used for SDS experiments	
Sodium dodecyl sulfate ≥ 99.0 %	Sigma-Aldrich
Magnesium chloride anhydrous ≥ 98.0 %	Sigma-Aldrich
Calcium chloride anhydrous ≥ 97.0 %	Sigma-Aldrich
Potassium chloride ≥ 99.0 %	Sigma-Aldrich
Used for PBLG-PLL experiments	
Deuterium oxide 99.9 atom %	Sigma-Aldrich
Trizma base ≥ 99.9 %	Sigma-Aldrich
Trizma hydrochloride ≥ 99.0 %	Sigma-Aldrich
Sodium phosphate monobasic monohydrate ≥ 99.5 %	Sigma-Aldrich
Sodium phosphate dibasic ≥ 99.0 %	Sigma-Aldrich
Sodium hydroxide ≥ 99.0 %	VWR Chemicals
Sodium carbonate ≥ 99.5 %	Sigma-Aldrich
Sodium bicarbonate ≥ 99.5 %	Sigma-Aldrich
Citric acid ≥ 99.5 %	Sigma-Aldrich
CHES ≥ 99.0 %	Sigma-Aldrich
CAPS ≥ 98.0 %	Sigma-Aldrich
Uranyl acetate (4 % aqueous solution) ≥ 98.0 %	Electron Microscopy Sciences

6.2 Error estimations of concentrations and fit parameters

The salt solutions used to dissolve both SDS and PBLG-PLL were prepared with a relative uncertainty of 0.0012 M. Based on this, all salt solutions are specified with three significant digits. This was calculated from

the precision of the scale (± 0.1 mg) and the volumetric flask (± 0.06 mL) used to prepare the samples. The concentrations can be found in Section 3.1.1 and 3.1.2.

The concentrations of SDS and PBLG-PLL samples are all specified with two significant digits as the majority of these samples were prepared by dilution. Although the number of significant digits that is found by using the relative uncertainty of the pipette (0.6 %) and the precision of the scale (±0.1 mg) is higher, two digits were used to account for possible imprecise pipetting before experiments.

To estimate errors in the obtained fit parameters from the fitting of scattering data from solutions of SDS, the optimized parameters were varied manually until the coefficient of determination, R^2, which is calculated automatically in the QtiKWS software, dropped by 10 %. If two parameters were co-dependent, one of the parameters were shifted manually until a maximum error was obtained before it was attempted to fit the other dependent variable. In the case of a non-satisfactory fit, the parameter was adjusted towards the original value until a satisfactory fit was obtained. The error for the dependent parameter was then taken as the difference between the new and the original value.

For DLS measurements, the same sample was measured three consecutive times to check for reproducibility and estimate the error in the hydrodynamic radii. The error was found by calculating the standard deviation of the three radii. The same procedure was applied for the FWHM calculations.

6.3 Indirect Fourier transformation fits

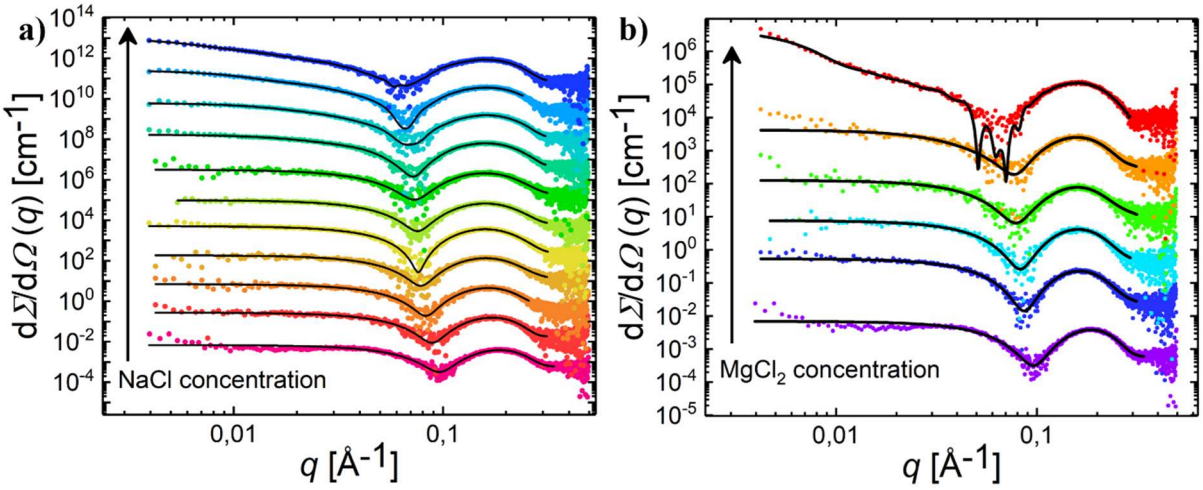

Figure 59: Scattering curves from 6.3 mg/mL SDS in aqueous solutions with **(a)** NaCl and **(b)** $MgCl_2$. The black lines are fits used to calculate $p(r)$. The curves are multiplied by 5^{2n} where n runs from 0 for clarity. Excellent fits were obtained for most concentrations apart from discrepancies from the first few scattering points for SDS in $MgCl_2$. It was also not possible to fit the minimum of the scattering curve from the highest concentration of $MgCl_2$ (red points), but this should not impact the determination of D_{max}.

6.4 Multiple scattering in DLS

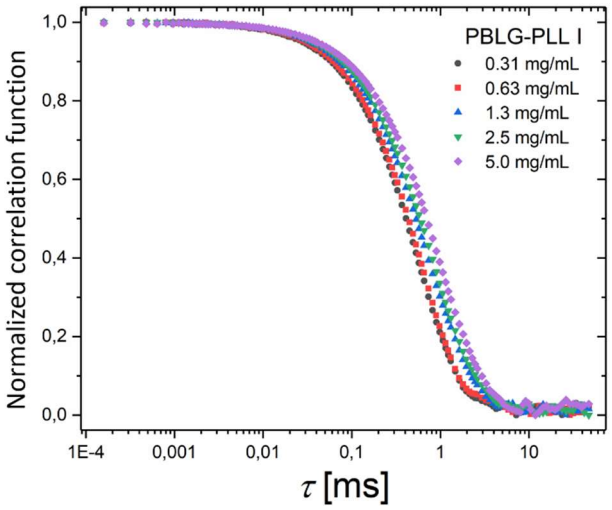

Figure 60: Plot showing the normalized cross-correlation functions obtained using DLS on a dilution series of PBLG-PLL I in pure water at 37 °C. Because the curves obtained from 0.63 mg/mL and 0.31 mg/mL overlap, multiple scattering was assumed to be negligible at these concentrations.

Data obtained from concentrated samples measured using DLS are usually not reliable due to possible multiple scattering and strong inter-particle interactions. This will show up as a dependency of concentration in the cross-correlation functions. By measuring a dilutions series of the stock solution and comparing the resulting cross-correlation curves, the highest possible concentration yielding reliable data can be found. A high concentration was desirable as the DLS data would later be compared to data from SAXS which is a technique requiring concentrated solutions. Although problems with multiple scattering should be minor due to the use of PCCS, the analysis was still done to ensure reliable results.

Figure 60 shows the normalized cross-correlation functions obtained using DLS on a dilution series of PBLG-PLL I in pure water at 37 °C. A dependency of concentration can here be observed which disappears at concentrations of 0.63 mg/mL and lower. While the effect could arise from a change in structure as a function of concentration or inter-particle interactions, multiple scattering was assumed to be the cause and the 0.63 mg/mL samples were chosen for the subsequent DLS experiments.

6.5 Full list of fit parameters

Table 14: Fit parameters obtained from fitting the model of prolate ellipsoids to scattering curves from SDS in pure water. The errors are evaluated as described in the Appendix Section 6.2. Errors in the structure factor parameters are omitted due to an unexpected upturn at low q-values which made it difficult to fit the structure factor. * denotes parameters that are not fitted.

Parameter	SDS in pure water			
conc [mg/mL]*	**6.3 mg/mL**	**13 mg/mL**	**25 mg/mL**	**50. mg/mL**
conc [vol. %]	0.53(3)	1.04(3)	2.03(5)	4.00(9)
ϵ	1.38(5)	1.35(4)	1.32(4)	1.34(4)
R [Å]	13.7(5)	14.0(4)	14.2(4)	14.5(4)
dR [Å]	8.2(3)	8.2(3)	8.3(2)	8.5(2)
N_{ave}*	42	44	45	49
d_{surf} [g/cm^3]*	1.162	1.162	1.162	1.162
R_{HS} [Å]	46.9	37.0	45.0	36.8
Z	3.2*	3.2*	3.2*	3.2
η	0.007	0.015	0.025	0.026
σ_{PD}*	0.1	0.1	0.1	0.1

Table 15: Fit parameters obtained from fitting the model of prolate ellipsoids to scattering curves from SDS in aqueous solutions with NaCl. The errors are evaluated as described in the Appendix Section 6.2. * denotes parameters that are not fitted.

Parameter	0.100 M				0.250 M				0.400 M			
	6.3 mg/mL	**13 mg/mL**	**25 mg/mL**	**50. mg/mL**	**6.3 mg/mL**	**13 mg/mL**	**25 mg/mL**	**50. mg/mL**	**6.3 mg/mL**	**13 mg/mL**	**25 mg/mL**	**50. mg/mL**
conc [vol. %]	0.43(3)	0.95(3)	2.04(5)	4.1(1)	0.45(3)	1.15(4)	2.12(4)	4.01(9)	0.54(3)	1.12(4)	2.2(5)	4.15(8)
ϵ	1.30(9)	1.32(9)	1.32(5)	1.30(4)	1.34(8)	1.34(6)	1.36(4)	1.29(6)	1.4(7)	1.37(9)	1.35(5)	1.35(4)
R [Å]	15.1(6)	15.1(5)	15.1(5)	15.2(3)	15.2(5)	15.5(3)	15.5(4)	15.5(3)	15.0(4)	15.3(5)	15.3(3)	15.5(3)
dR [Å]	9.0(3)	9.0(4)	9.0(3)	9.0(3)	8.8(3)	8.8(6)	8.8(2)	9.4(3)	8.8(5)	8.8(4)	9.4(3)	9.4(3)
N_{ave}*	54	55	54	54	56	60	60	57	57	60	58	60
d_{surf} [g/cm^3]	1.154(5)	1.154(3)	1.154(3)	1.154(3)	1.150(4)	1.150(3)	1.150(3)	1.150(3)	1.148(5)	1.148(3)	1.148(2)	1.147(3)
R_{HS} [Å]	N/A	50.0(4)	39.1(5)	34.8(5)	N/A	36.3(3)	34.8(4)	35.6(4)	N/A	N/A	N/A	35.6(5)
Z	N/A	0	0	0	N/A	0	0	0	N/A	N/A	N/A	0
η	N/A	0.019(2)	0.066(7)	0.141(15)	N/A	0.020(2)	0.031(3)	0.071(7)	N/A	N/A	N/A	0.033(3)
σ_{PD}*	0.1	0.1	0.1	0.1	0.1	0.1	0.1	0.1	0.1	0.1	0.1	0.1

Table 16: Fit parameters obtained from fitting model of short and long rod-like micelles to scattering curves from SDS in aqueous solutions with NaCl. The errors are evaluated as described in the Appendix Section 6.2. * denotes parameters that are not fitted.

Parameter	0.500 M				0.550 M				0.600 M			
	6.3 mg/mL	13 mg/mL	25 mg/mL	50. mg/mL	6.3 mg/mL	13 mg/mL	25 mg/mL	50. mg/mL	6.3 mg/mL	13 mg/mL	25 mg/mL	50. mg/mL
$conc$ [vol. %]	0.50(3)	1.32(3)	2.53(5)	4.52(8)	0.40(3)	0.88(4)	1.70(4)	3.92(7)	0.47(2)	1.15(3)	2.24(6)	4.35(6)
R_{core} [Å]	13.1(5)	13.1(5)	13.1(4)	13.8(4)	12.8(5)	13.14(4)	13.1(4)	13.1(3)	13.2(4)	13.0(4)	13.0(3)	13.8(3)
dR [Å] *	9.4(3)	9.4(3)	9.4(2)	9.4(2)	9.4(3)	9.4(2)	9.4(3)	9.4(3)	9.4(3)	9.4(3)	9.4(2)	9.4(2)
N_{ave} *	80	104	81	106	73	93	101	106	89	120	156	188
$L_{c,mean}$ [Å]	52(6)	68(7)	52(6)	63(5)	50(5)	61(6)	66(5)	69(5)	58(6)	79(8)	103(10)	110(12)
b (Kuhn) [Å] *	350	350	350	350	350	350	350	350	400	400	400	400
d_{surf} [g/cm^3]	1.136(4)	1.130(4)	1.136(3)	1.142(3)	1.139(3)	1.139(3)	1.138(2)	1.139(3)	1.139(4)	1.134(4)	1.130(5)	1.137(3)
B	N/A	N/A	N/A	7.6E-05(7)	N/A	N/A	N/A	5.0E-05(8)	N/A	N/A	N/A	3.3E-05(9)
σ_{PD} *	0.15	0.15	0.15	0.15	0.15	0.15	0.15	0.15	0.15	0.15	0.15	0.15
	0.650 M				0.750 M				0.850 M			
	6.3 mg/mL	13 mg/mL	25 mg/mL	50. mg/mL	6.3 mg/mL	13 mg/mL	25 mg/mL	50. mg/mL	6.3 mg/mL	13 mg/mL	25 mg/mL	50. mg/mL
$conc$ [$vol.$%]	0.57(2)	1.18(3)	2.12(8)	4.60(7)	0.51(4)	1.20(4)	2.07(5)	4.79(6)	0.53(2)	1.08(3)	2.23(3)	4.25(9)
R_{core} [Å]	13.0(4)	12.8(5)	12.8(4)	12.8(2)	12.8(4)	12.8(6)	12.8(4)	12.8(5)	12.8(5)	12.8(4)	12.8(5)	12.8(3)
dR [Å] *	9.4(4)	9.4(2)	9.4(2)	9.4(2)	9.4(4)	9.4(4)	9.4(2)	9.4(2)	9.4(4)	9.4(2)	9.4(2)	9.4(2)
N_{ave} *	148	202	217	264	286	404	324	769	734	769	622	805
$L_{c,mean}$ [Å]	98(8)	138(12)	148(13)	181(16)	195(20)	276(25)	221(26)	526(42)	502(51)	526(40)	426(34)	551(42)
b (Kuhn) [Å] *	700	700	700	700	850	850	850	850	850	850	850	850
d_{surf} [g/cm^3]	1.132(3)	1.131(3)	1.130(2)	1.130(2)	1.127(3)	1.127(2)	1.127(3)	1.127(2)	1.123(3)	1.123(2)	1.120(4)	1.123(4)
B	N/A	N/A	N/A	1.1E-05(8)	N/A	N/A	N/A	3.0E-06	N/A	N/A	N/A	2E-06(1)
σ_{PD} *	0.15	0.15	0.15	0.15	0.15	0.15	0.15	0.15	0.15	0.15	0.15	0.15
	1.00 M											
	6.3 mg/mL	13 mg/mL	25 mg/mL	50. mg/mL								
$conc$ [$vol.$%]	0.47(4)	0.98(5)	2.05(7)	4.55(8)								
R_{core} [Å]	12.8(5)	12.8(4)	12.7(4)	12.7(4)								
dR [Å] *	9.4(4)	9.4(3)	9.4(4)	9.4(4)								
N_{ave} *	920	918	941	977								
$L_{c,mean}$ [Å]	629(58)	628(42)	653(59)	678(55)								
b (Kuhn) [Å] *	850	850	850	850								
d_{surf} [g/cm^3]	1.124(3)	1.121(3)	1.119(4)	1.119(4)								
B	N/A	N/A	N/A	N/A								
σ_{PD} *	0.15	0.15	0.15	0.15								

Table 17: Fit parameters obtained from fitting the model of prolate ellipsoids to scattering curves from SDS in aqueous solutions with $MgCl_2$. The errors are evaluated as described in the Appendix Section 6.2. * denotes parameters that are not fitted.

Parameter	0.0835 M			
	6.3 mg/mL	13 mg/mL	25 mg/mL	50. mg/mL
$conc$ [vol. %]	0.52(3)	1.22(3)	2.45(4)	4.23(6)
ϵ	1.34(8)	1.34(5)	1.30(6)	1.25(7)
R [Å]	15.2(4)	15.5(5)	15.8(3)	15.8(3)
dR [Å] *	9.4(3)	9.4(4)	9.4(2)	9.4(2)
N_{ave} *	56	59	61	59
d_{surf} [g/cm^3]	1.184(4)	1.183(4)	1.173(4)	1.164(3)
R_{HS} [Å]	N/A	N/A	N/A	39.8(4)
Z	N/A	N/A	N/A	0
η	N/A	N/A	N/A	0.038(4)
σ_{PD} *	0.1	0.1	0.1	0.1

Table 18: Fit parameters obtained from fitting the model of short and long cylindrical micelles to scattering curves from SDS in aqueous solutions with $MgCl_2$. The errors are evaluated as described in the Appendix Section 6.2. * denotes parameters that are not fitted.

Parameter	0.167 M				0.250 M				0.333 M			
	6.3 mg/mL	13 mg/mL	25 mg/mL	50. mg/mL	6.3 mg/mL	13 mg/mL	25 mg/mL	50. mg/mL	6.3 mg/mL	13 mg/mL	25 mg/mL	50. mg/mL
$conc$ [$vol.\%$]	0.35(3)	0.95(4)	2.00(4)	4.06(8)	0.42(4)	1.10(3)	1.50(5)	4.70(6)	0.50(3)	0.95(4)	1.74(6)	4.25(7)
R_{core} [Å]	13.5(4)	13.3(4)	13.3(2)	13.3(2)	12.8(3)	12.8(3)	12.9(2)	13.0(2)	12.8(3)	12.8(3)	12.8(3)	12.8(2)
dR [Å] *	9.4(3)	9.4(4)	9.4(3)	9.4(3)	9.4(4)	9.4(3)	9.4(3)	9.4(2)	9.4(4)	9.4(4)	9.4(2)	9.4(2)
N_{ave} *	71	69	78	83	52	52	93	94	54	108	147	147
$L_{c,mean}$ [Å]	44(4)	44(5)	50(4)	52(5)	36(5)	36(5)	63(4)	63(5)	37(5)	75(7)	102(7)	102(9)
b (Kuhn) [Å] *	N/A	N/A	N/A	N/A	N/A	N/A	N/A	N/A	N/A	N/A	500	500
d_{surf} [g/cm^3]	1.147(3)	1.147(4)	1.145(3)	1.145(2)	1.145(4)	1.140(4)	1.141(3)	1.144(3)	1.140(4)	1.134(4)	1.132(2)	1.133(2)
B	N/A	N/A	N/A	5.0E-05(8)	N/A	N/A	N/A	N/A	N/A	N/A	N/A	N/A
σ_{PD}	0.15	0.15	0.15	0.15	0.15	0.15	0.15	0.15	0.15	0.15	0.15	0.15

	0.500 M			
	6.3 mg/mL	13 mg/mL	25 mg/mL	50. mg/mL
$conc$ [$vol.\%$]	0.60(4)	1.40(4)	1.97(5)	4.15(7)
R_{core} [Å]	12.8(4)	12.8(3)	12.8(2)	12.7(2)
dR [Å] *	9.4(4)	9.4(4)	9.4(3)	9.4(2)
N_{ave}*	N/A	N/A	N/A	N/A
$L_{c,mean}$ [Å]	1000	1000	1000	1000
b (Kuhn) [Å]	270(53)	270(45)	270	550
d_{surf} [g/cm^3]	1.124(4)	1.118(5)	1.122(3)	1.125(3)
B	N/A	N/A	N/A	N/A
σ_{PD} *	0.15	0.15	0.15	0.15

Table 19: Fit parameters obtained from fitting the model of prolate ellipsoids to scattering curves from SDS in aqueous solutions with KCl and $CaCl_2$. The errors are evaluated as described in the Appendix Section 6.2. * denotes parameters that are not fitted.

Parameter	5 mM KCl		5 mM $CaCl_2$	
	6.3 mg/mL	13 mg/mL	6.3 mg/mL	13 mg/mL
$conc$ [vol. %]	0.6(1)	1.2(3)	0.5(1)	1.2(3)
ϵ	1.50(6)	1.45(5)	1.45(5)	1.35(5)
R [Å]	13.6(4)	13.5(4)	14.0(4)	14.2(4)
dR [Å]	8.0(3)	8.3(3)	8.2(3)	8.43()
N_{ave} *	45	43	47	46
d_{surf} [g/cm^3]	1.156(4)	1.156(4)	1.156(3)	1.155(4)
R_{HS} [Å]	52.7(4)	52.0(5)	66.5	56.5
Z*	3.2	3.2	3.2	3.2
η	0.047(7)	0.13(2)	0.129	0.132
σ_{PD} *	0.1	0.1	0.1	0.1

Table 20: Parameters used to produce the simulated curves shown in Figure 49 in Section 4.2.3 together with the scattering curves from PBLG I, II and III. Error estimations are not included as the vesicle model was unable to fit the data.

Parameter	PBLG-PLL I	PBLG-PLL II	PBLG-PLL III
Concentration	5.0 mg/mL	5.0 mg/mL	5.0 mg/mL
W_{core} [Å]	500	500	500
W_1 [Å]	150	150	150
W_2 [Å]	150	150	150
W_3 [Å]	150	150	150
W_4 [Å]	30	30	30
σ_{core} [Å]	30	30	30
σ_1 [Å]	30	30	30
σ_2 [Å]	30	30	30
σ_3 [Å]	500	500	500
R_{tot} [Å]	1190	1190	1190
f	0.4	0.4	0.4
f_{wi}	0.53	0.63	0.84
f_{wo}	0.29	0.34	0.46
$R_{G,\ blob}$	50	65	70
σ_{PD} (Polydispersity)	0.2	0.2	0.2

7 Bibliography

1. Tanford, C., *The hydrophobic effect: formation of micelles and biological membranes*. 1973, New York: Wiley.
2. Mittal, K.L. and E.J. Fendler, *Solution Behavior of Surfactants: Theoretical and Applied Aspects Volume 1*. 1982, Boston, MA: Springer US.
3. Singh, A., J.D. Van Hamme, and O.P. Ward, *Surfactants in microbiology and biotechnology: Part 2. Application aspects.* Biotechnology Advances, 2007. **25**(1): p. 99-121.
4. Shi, J., et al., *Nanotechnology in drug delivery and tissue engineering: from discovery to applications.* Nano letters, 2010. **9**(10): p. 3223-3230.
5. Sakamoto, K., *Cosmetic science and technology: theoretical principles and applications*. 2017, Amsterdam, Netherlands; Oxford, England; Cambridge, Massachusetts: Elsevier.
6. Widom, B., P. Bhimalapuram, and K. Koga, *The hydrophobic effect.* Physical Chemistry Chemical Physics, 2003. **5**(15): p. 3085-3093.
7. Hamley, I.W., *Block copolymers in solution: fundamentals and applications*. 2005, Chichester: Wiley.
8. Israelachvili, J.N., *Intermolecular and Surface Forces*. 3 ed. 2010, Amsterdam, Netherlands: Elsevier Science.
9. Bergström, M. and J. Skov Pedersen, *Structure of pure SDS and DTAB micelles in brine determined by small-angle neutron scattering (SANS).* Physical Chemistry Chemical Physics, 1999. **1**(18): p. 4437-4446.
10. Magid, L., Z. Li, and P.D. Butler, *Flexibility of elongated sodium dodecyl sulfate micelles in aqueous sodium chloride: A small-angle neutron scattering study.* Langmuir, 2000. **16**(26): p. 10028-10036.
11. Arleth, L., M. Bergström, and J.S. Pedersen, *Small-angle neutron scattering study of the growth behavior, flexibility, and intermicellar interactions of wormlike SDS micelles in NaBr aqueous solutions.* Langmuir, 2002. **18**(14): p. 5343-5353.
12. Jensen, G.V., et al., *Monitoring the Transition from Spherical to Polymer ‐ like Surfactant Micelles Using Small ‐ Angle X ‐ Ray Scattering.* Angewandte Chemie International Edition, 2014. **53**(43): p. 11524-11528.
13. Patist, A., et al., *Kinetics of micellization: its significance to technological processes.* Colloids and Surfaces A: Physicochemical and Engineering Aspects, 2001. **176**(1): p. 3-16.
14. Villarreal, M.R. 2007; Available from: https://commons.wikimedia.org/wiki/File:Phospholipids_aqueous_solution_structures.svg.
15. Attwood, D. and A.T. Florence, *Surfactant systems: their chemistry, pharmacy and biology*. 1983, London: Chapman and Hall.
16. Jönsson, B., *Surfactants and polymers in aqueous solution*. 1998, Chichester: Wiley.
17. Aswal, V.K. and P.S. Goyal, *Counterions in the growth of ionic micelles in aqueous electrolyte solutions: A small-angle neutron scattering study.* Physical Review E, 2000. **61**(3): p. 2947-2953.
18. Magid, L.J., et al., *Tuning the Contour Lengths and Persistence Lengths of Cationic Micelles: The Role of Electrostatics and Specific Ion Binding.* The Journal of Physical Chemistry B, 2000. **104**(29): p. 6717-6727.
19. Dutkiewicz, E. and A. Jakubowska, *Effect of electrolytes on the physicochemical behaviour of sodium dodecyl sulphate micelles.* Colloid and Polymer Science, 2002. **280**(11): p. 1009-1014.
20. Kumar, S., et al., *A SANS study on growth of anionic micelles with quaternary ammonium bromide.* Current Science, 2003. **84**(10): p. 1346-1349.
21. Angelescu, D., H. Caldararu, and A. Khan, *Some observations on the effect of the trivalent counterion Al3+ to the self-assembly of sodium dodecyl sulphate in water.* Colloids and Surfaces A: Physicochemical and Engineering Aspects, 2004. **245**(1): p. 49-60.
22. Iyota, H., T. Tomimitsu, and M. Aratono, *Miscibility of calcium chloride and sodium dodecyl sulfate in the adsorbed film and aggregates.* Kolloid-Zeitschrift und Zeitschrift für Polymere, 2010. **288**(12): p. 1313-1320.
23. Sangwai, A.V., R. Sureshkumar, and A.V. Sangwai, *Coarse-grained molecular dynamics simulations of the sphere to rod transition in surfactant micelles.* Langmuir : the ACS journal of surfaces and colloids, 2011. **27**(11): p. 6628-6638.
24. Volkov, N.A., N.V. Tuzov, and A.K. Shchekin, *Molecular dynamics study of salt influence on transport and structural properties of SDS micellar solutions.* Fluid Phase Equilibria, 2016. **424**: p. 114-121.

25. Schäfer, K., et al., *Beyond the molecular packing model: understanding morphological transitions of charged surfactant micelles.* Unpublished manuscript, 2019.
26. Lazzari, M., G. Liu, and S. Lecommandoux, *Block Copolymers in Nanoscience*. 2008, Weinheim, Germany: Wiley.
27. Lee, J.S. and J. Feijen, *Polymersomes for drug delivery: Design, formation and characterization.* Journal of Controlled Release, 2012. **161**(2): p. 473-483.
28. Tian, B., et al., *Polypeptide-based vesicles: formation, properties and application for drug delivery.* Journal of Materials Chemistry, 2012. **22**(34): p. 17404.
29. Aliferis, T., H. Iatrou, and N. Hadjichristidis, *Living polypeptides.* Biomacromolecules, 2004. **5**(5): p. 1653-1656.
30. Hadjichristidis, N., et al., *Synthesis of well-defined polypeptide-based materials via the ring-opening polymerization of alpha-amino acid N-carboxyanhydrides.* Chemical Reviews, 2009. **109**: p. 5528-5578.
31. Holowka, E.P., D.J. Pochan, and T.J. Deming, *Charged Polypeptide Vesicles with Controllable Diameter.* Journal of the American Chemical Society, 2005. **127**(35): p. 12423-12428.
32. Rodríguez-Hernández, J. and S. Lecommandoux, *Reversible Inside−Out Micellization of pH-responsive and Water-Soluble Vesicles Based on Polypeptide Diblock Copolymers.* Journal of the American Chemical Society, 2005. **127**(7): p. 2026-2027.
33. Chiou, J.-S., et al., *The α-helix to β-sheet transition in poly(l-lysine): Effects of anesthetics and high pressure.* Biochimica et Biophysica Acta (BBA) - Protein Structure and Molecular Enzymology, 1992. **1119**(2): p. 211-217.
34. Díez-Pascual, A.M., P.S. Shuttleworth, and A.M. Díez-Pascual, *Layer-by-Layer Assembly of Biopolyelectrolytes onto Thermo/pH-Responsive Micro/Nano-Gels.* Materials, 2014. **7**(11): p. 7472-7512.
35. Gerweck, L.E. and K. Seetharaman, *Cellular pH gradient in tumor versus normal tissue: potential exploitation for the treatment of cancer.* Cancer Res, 1996. **56**(6): p. 1194-8.
36. Hamley, I.W., *Introduction to soft matter: synthetic and biological self-assembling materials*. Rev. ed. ed. 2007, Chichester: Wiley.
37. Dill, K.A., S. Bromberg, and D. Stigter, *Molecular driving forces: statistical thermodynamics in biology, chemistry, physics, and nanoscience*. 2nd ed. ed. 2011, London: Garland Science.
38. Israelachvili, J.N., D.J. Mitchell, and B.W. Ninham, *Theory of self-assembly of hydrocarbon amphiphiles into micelles and bilayers.* Journal of the Chemical Society, Faraday Transactions 2, 1976. **72**: p. 1525.
39. Pedersen, J.S., *Small-Angle Scattering from Surfactants and Block Copolymer Micelles*, ed. R. Borsali and R. Pecora. 2008, Dordrecht, Netherlands: Springer. 191-233.
40. Bruce, C.D., et al., *Molecular Dynamics Simulation of Sodium Dodecyl Sulfate Micelle in Water: Micellar Structural Characteristics and Counterion Distribution.* The Journal of Physical Chemistry B, 2002. **106**(15): p. 3788-3793.
41. Rakitin, A.R. and G.R. Pack, *Molecular dynamics simulations of ionic interactions with dodecyl sulfate micelles.* Journal of Physical Chemistry B, 2004. **108**(8): p. 2712.
42. Sammalkorpi, M., M. Karttunen, and M. Haataja, *Ionic surfactant aggregates in saline solutions: sodium dodecyl sulfate (SDS) in the presence of excess sodium chloride (NaCl) or calcium chloride (Ca[Cl.sub.2]).* Journal of Physical Chemistry B, 2009. **113**(17): p. 5863-5870.
43. Yan, H., et al., *Effect of Ca2+ and Mg2+ Ions on Surfactant Solutions Investigated by Molecular Dynamics Simulation.* Langmuir, 2010. **26**(13): p. 10448-10459.
44. Wennerstrom, H., A. Khan, and B. Lindman, *Ionic surfactants with divalent counterions.* Advances in Colloid and Interface Science, 1991. **34**: p. 433-449.
45. Als-Nielsen, J. and D. McMorrow, *Elements of modern X-ray physics*. 2nd ed. ed. 2011, Chichester: Wiley.
46. Willis, B.T.M. and C.J. Carlile, *Experimental neutron scattering*. 2009, Oxford: Oxford University Press.
47. Lindner, P. and T. Zemb, *Neutrons, x-rays and light: scattering methods applied to soft condensed matter*. 2002, Amsterdam: Elsevier.
48. Bruce, D.W., D. O'Hare, and R.I. Walton, *Structure from diffraction methods*. 2014, John Wiley & Sons, Ltd.: West Sussex, England.
49. Brumberger, H., *Modern aspects of small-angle scattering*. Vol. 451. 1995, Dordrecht: Kluwer.
50. Guinier, A. and G. Fournet, *Small-angle scattering of x-rays*. Structure of matter series. 1955, New York: Wiley.
51. Moore, P.B., *Small‐angle scattering. Information content and error analysis.* Journal of Applied Crystallography, 1980. **13**(2): p. 168-175.
52. Schmitz, K.S., *An introduction to dynamic light scattering by macromolecules*. 1990, Boston: Academic Press.

53. Goldburg, W.I., *Dynamic light scattering.* American Journal of Physics, 1999. **67**(12): p. 1152-1160.
54. Instruments, M., *Dynamic light scattering: an introduction in 30 minutes. Technical Note Malvern*. 2012. 1-8.
55. Urban, C. and P. Schurtenberger, *Characterization of Turbid Colloidal Suspensions Using Light Scattering Techniques Combined with Cross-Correlation Methods.* Journal of Colloid And Interface Science, 1998. **207**(1): p. 150-158.
56. Witt, W., H. Geers, and L. Aberle, *Measurement of Particle Size and Stability of Nanoparticles in Opaque Suspensions and Emulsions with Photon Cross Correlation Spectroscopy (PCCS)*. 2004, Germany: Partec.
57. Einstein, A., *Zur Theorie der Brownschen Bewegung.* Annalen der Physik, 2005. **14**(1): p. 248-258.
58. Siegert, A.J.F. and M.I.o.T.R. Laboratory, *On the Fluctuations in Signals Returned by Many Independently Moving Scatterers*. 1943: Radiation Laboratory, Massachusetts Institute of Technology.
59. Morrison, I.D., E.F. Grabowski, and C.A. Herb, *Improved techniques for particle size determination by quasi-elastic light scattering.* Langmuir, 1985. **1**(4): p. 496-501.
60. Stetefeld, J., S. McKenna, and T. Patel, *Dynamic light scattering: a practical guide and applications in biomedical sciences.* Biophysical Reviews, 2016. **8**(4): p. 409-427.
61. Glatter, O., *A new method for the evaluation of small‐angle scattering data.* Journal of Applied Crystallography, 1977. **10**(5): p. 415-421.
62. Glatter, O., *The interpretation of real-space information from small-angle scattering experiments.* Journal of Applied Crystallography, 1979. **12**(2): p. 166-175.
63. Almgren, M., et al., *SDS Micelles at High Ionic Strength. A Light Scattering, Neutron Scattering, Fluorescence Quenching, and CryoTEM Investigation.* Journal of Colloid And Interface Science, 1998. **202**(2): p. 222-231.
64. Pedersen, Laso, and Schurtenberger, *Monte Carlo study of excluded volume effects in wormlike micelles and semiflexible polymers.* Physical review, 1996. **54**(6): p. R5917.
65. Pedersen, J.S. and P. Schurtenberger, *Scattering Functions of Semiflexible Polymers with and without Excluded Volume Effects.* Macromolecules, 1996. **29**(23): p. 7602-7612.
66. Schmid, A.J., et al., *Multi-Shell Hollow Nanogels with Responsive Shell Permeability.* Scientific Reports, 2016. **6**: p. 22736.
67. Debye, P., *Molecular-weight determination by light scattering.* The Journal of physical and colloid chemistry, 1947. **51**(1): p. 18.
68. Hayter, J.B. and J. Penfold, *An analytic structure factor for macroion solutions.* Molecular Physics, 1981. **42**(1): p. 109-118.
69. Zimm, B.H., *The Scattering of Light and the Radial Distribution Function of High Polymer Solutions.* The Journal of Chemical Physics, 1948. **16**(12): p. 1093-1099.
70. Schweizer, K.S. and J.G. Curro, *PRISM theory of the structure, thermodynamics, and phase transitions of polymer liquids and alloys*, in *Atomistic Modeling of Physical Properties*, L. Monnerie and U.W. Suter, Editors. 1994, Springer: Berlin, Heidelberg. p. 319-377.
71. Unknown, 372px-Scheme_TEM_en.svg, Editor. 2009, Wikipedia: Wikimedia Commons.
72. Leng, Y., *Materials Characterization: Introduction to Microscopic and Spectroscopic Methods*. 2nd ed. ed. Materials Characterization. 2013, Hoboken: Wiley.
73. Franken, L.E., E.J. Boekema, and M.C.A. Stuart, *Transmission Electron Microscopy as a Tool for the Characterization of Soft Materials: Application and Interpretation.* Advanced science, 2017. **4**(5): p. 1600476.
74. Guerreiro, E.M., et al., *Efficient extracellular vesicle isolation by combining cell media modifications, ultrafiltration, and size-exclusion chromatography.* PLoS One, 2018. **13**(9): p. e0204276.
75. Nakagaki, M. and S. Yokoyama, *Acid-Catalyzed Hydrolysis of Sodium Dodecyl Sulfate.* Journal of Pharmaceutical Sciences, 1985. **74**(10): p. 1047-1052.
76. Borkowski, M., *Buffer Maker*. 2013, Chembuddy, Marki, Poland.
77. Pernot, P., et al., *New beamline dedicated to solution scattering from biological macromolecules at the ESRF.* Journal of Physics: Conference Series, 2010. **247**: p. 012009.
78. Narayanan, T., et al., *A multipurpose instrument for time-resolved ultra-small-angle and coherent X-ray scattering.* Journal of Applied Crystallography, 2018. **51**(6): p. 1511-1524.
79. *The European Synchrotron and Radiation Facility*. [Web Page] [cited 2019 22.02]; Available from: https://www.esrf.eu/home/UsersAndScience/Experiments/MX/About_our_beamlines/bm29.html.
80. Fan, L., et al., *The Absolute Calibration of a Small-Angle Scattering Instrument with a Laboratory X-ray Source.* Journal of Physics: Conference Series, 2010. **247**: p. 012005.
81. Pipich, V., *QtiKWS.* 2019, Jülich Centre for Neutron Science, Germany.

82. Konarev, P.V., et al., *PRIMUS: a Windows PC-based system for small-angle scattering data analysis.* Journal of Applied Crystallography, 2003. **36**(5): p. 1277-1282.
83. D.I. Svergun, A.S., *GNOM*. 2009, ATSAS.
84. Huber, M.L., et al., *New International Formulation for the Viscosity of H2O.* Journal of Physical and Chemical Reference Data, 2009. **38**(2): p. 101-125.
85. OriginLab, *Origin 2017*. 2017, OriginLab, United States.
86. GmbH, S., *Windox 5*. 2016, Sympatec GmbH, Germany.
87. Glatter, O. and O. Kratky, *Small angle X-ray scattering*. 1982, London: Academic Press.
88. Mahapatra, P., *Structure of Micelles Calcium Didodecyl Sulfate: A SAXS Study.* Journal of Nanomedicine & Nanotechnology, 2015. **06**(04).
89. Berret, J.-F., *Evidence of overcharging in the complexation between oppositely charged polymers and surfactants.* The Journal of Chemical Physics, 2005. **123**(16).
90. Vass, S., et al., *Sodium alkyl sulfate apparent molar volumes in normal and heavy water: Connection with micellar structure.* Journal of Physical Chemistry, 1989. **93**(17): p. 6553-6559.
91. Vass, S., et al., *Ambiguity in Determining the Shape of Alkali Alkyl Sulfate Micelles from Small-Angle Scattering Data.* Langmuir, 2008. **24**(2): p. 408-417.
92. Vold, M.J., *Role of shape in models of micellar equilibria.* Langmuir, 1985. **1**(4): p. 501-506.
93. Beaucage, G., *Small-angle scattering from polymeric mass fractals of arbitrary mass-fractal dimension.* J. Appl. Crystallogr., 1996. **29**: p. 134-146.
94. Magnus Bergström, L. and V.M. Garamus, *Structural behaviour of mixed cationic surfactant micelles: A small-angle neutron scattering study.* Journal of Colloid and Interface Science, 2012. **381**(1): p. 89-99.
95. Dušek, K., *Polymer networks*. Advances in polymer science. Vol. 44. 1982, Berlin: Springer.
96. Hall, D.G., *Polydispersity of sodium dodecyl sulfate (SDS) micelles.* Langmuir, 1999. **15**(10): p. 3483-3485.
97. Ainavarapu, S.R.K., et al., *Contour length and refolding rate of a small protein controlled by engineered disulfide bonds.* Biophysical journal, 2007. **92**(1): p. 225-233.
98. Holmes, R.W., M.B. Huglin, and M.K. Lai, *Helix — coil transition of poly(γ-bensyl L-glutamate) in dioxan — dichloracetic acid mixtures.* International Journal of Biological Macromolecules, 1979. **1**(1): p. 23-28.
99. Leson, A., et al., *Water permeation through block-copolymer vesicle membranes.* Chemical Physics Letters, 2007. **444**(4): p. 268-272.
100. Quan, L., et al., *Revealing membrane permeability of polymersomes through fluorescence enhancement.* Colloids and Surfaces B: Biointerfaces, 2018. **161**: p. 156-161.
101. Meier, W.P. and W. Knoll, *Polymer Membranes/Biomembranes*. Advances in Polymer Science. Vol. 224. 2010, Berlin: Springer.
102. Cass, A. and A. Finkelstein, *Water Permeability of Thin Lipid Membranes.* The Journal of General Physiology, 1967. **50**(6): p. 1765-1784.